Search for Long-lived Particles Decaying into Displaced Jets with the CMS Detector at the Large Hadron Collider

Jingyu Luo

A Dissertation

Presented to the Faculty

of Princeton University

in Candidacy for the Degree

of Doctor of Philosophy

Recommended for Acceptance

by the Department of

Physics

Advisor: Daniel Marlow

September, 2019

Abstract

The existence of long-lived particles is very generic in many beyond standard model scenarios. A search for long-lived particles decaying into jets is presented in this dissertation. Data were collected with the CMS detector at the LHC from proton-proton collisions at a center-of-mass energy of 13 TeV in 2016, corresponding to an integrated luminosity of $35.9\,\mathrm{fb}^{-1}$. The search examines the distinctive topology of displaced tracks and secondary vertices. The selected events are found to be consistent with standard model predictions. The search is sensitive to a wide range of models predicting long-lived particles decaying into displaced jets. For a simplified model in which long-lived neutral particles are pair produced and decay to two jets, pair production cross sections larger than 0.2 fb are excluded at 95% confidence level for a long-lived particle mass larger than 1000 GeV and proper decay lengths between 3 and 130 mm. Several supersymmetry models with gauge-mediated supersymmetry breaking or R-parity violation, where pair-produced long-lived gluinos or top squarks decay to several final-state topologies containing displaced jets, are also tested. For these models, in the mass ranges above 200 GeV, gluino masses up to 2300–2400 GeV and top squark masses up to 1350–1600 GeV are excluded for proper decay lengths approximately between 10 and 100 mm. These are the most restrictive limits to date on these models.

Acknowledgements

First and foremost, I'd like to express my deep gratitude to my advisor Professor Dan Marlow. Over the past five years, Dan has given me enormous support and unimaginable freedom, without which I could not have accomplished the research project presented in this thesis. It is his vision that had led me to this fantastic topic. I'm really grateful for the great opportunity to study and work under his guidance. He has also given me almost absolute freedom to pursue my interests and to explore different ideas in physics, which was an incredible experience for a Ph.D. student in experimental high energy physics.

I also would like to thank Professor Chris Tully, for taking the time to review my thesis as well as for many inspiring discussions on physics and other things. Thanks to Professor Mariangela Lisanti and Professor Peter Meyers for kindly agreeing to serve on my thesis committee. I would also like to thank my undergraduate advisors – Professor Zhengguo Zhao and Professor Bing Zhou – for introducing me to high energy physics, for trusting me when I doubted myself, and for unreserved help in my most difficult times. They have set up great examples for me both as a physicist and as a human being.

The work presented in this thesis could not have been accomplished and published

without the help of many colleagues in the CMS collaboration. I'd like to thank the wonderful coordination work of the Exotica conveners Slava Valouev, Oliver Buchmueller, and Ivan Mikulec, as well as the long-lived conveners Ted Kolberg, Albert De Roeck, Steven Lowette, and Juliette Alimena. I should also thank my Article Review Committees (ARC), especially Eva Halkiadakis, who served as the chair of my ARC. Eva provided many valuable comments on this work during the review process, her wonderful ARC leadership is really helpful for polishing the physics results as well as making the review/publication process smooth. Thanks also go to the EXO/B2G board of CMS publications committee – Dave Cutts and Bob Brown, whose magnificent suggestions on the editings greatly helped improve the quality of the paper. It is also a great pleasure to know John Paul Chou, I'm very grateful for many discussions with him on long-lived particles, his encouragement meant a lot to me when I was working on this analysis.

My sincere thanks also go to Chris Palmer, for his help and guidance in the work on the luminosity measurement. I remember the days Chris and I worked together day and night to pull out the luminosity results for CMS, those days were intensive but also extremely fruitful, I benefited a lot from the collaboration and the friendship with him. Thanks to Professor Jim Olsen and Professor Isobel Ojalvo for advices throughout the years. I would also like to thank other graduate students of Princeton working in the CMS experiment – Stephane Cooperstein, Gage Dezoort, Nick Haubrick, Josh Hardenbrook, Sam Higginbotham, Gillian Kopp, Stephanie Kwan, and Kelvin Mei – for making such a wonderful group. I sincerely believe that we are the best in CMS. I'm also really thankful to Kim Dawidowski for her amazing and constant administrative support.

I also feel very fortunate to have many great friends at CERN and Geneva – Jing Chen, Jue Chen, Chong Geng, Wen Guo, Yicheng Guo, Weifeng Ji, Xiangyang Ju, Yanlin Liu, Haonan Lu, Nan Lu, Xinmei Niu, Rongkun Wang, Zirui Wang, Hua Wei, Meng Wu, Yusheng Wu, Zhaoxu Xi, Lailin Xu, Hongtao Yang, Liqing Zhang, Chen Zhou. Their friendship and precious advices have brought lots of joyful memories for the year I stayed at CERN, which I will treasure for the rest of my life.

I'm also indebted to many friends at Princeton. The years at Princeton have not only taught me a lot about physics, but also have greatly influenced the way I view life. I have had the amazing 10-year long friendship with Huan He, Jie Wang, and Yunqin Zheng, which started when we were still undergraduate students in USTC. I would also like to thank my roommate Zhenbin Yang for all the time we spend together. The gratitude also goes to many other friends, who really make a difference for my life at Princeton – Xiaowen Chen, Yiming Chen, Zijia Cheng, Yale Fan, Tong Gao, Po-Shen Hsin, Yuwen Hu, Ziming Ji, Jiaqi Jiang, JaeUk Kim, Zhaoqi Leng, Sihang Liang, Ho-Tat Lam, Xinran Li, Biao Lian, Jingjing Lin, Zheng Ma, Justin Ripley, Yu Shen, Xiaojie Shi, Xue Song, Suerfu, Jiepeng Wang, Siwei Wang, Wudi Wang, Yi Wang, Xuelan Wu, Yantao Wu, Fang Xie, Jun Xiong, Bin Xu, Xinwei Yu, Junyi Zhang, Sonia Zhang, Bo Zhao, Fang Zhao, Wenli Zhao, Hao Zheng, Zheyi Zhu, and many many others. I hope all my friends will have a bright future and a happy life.

Last but not the least, I should express my deep gratitude to my parents for their unconditional love and support throughout my life.

To my beloved grandma.

Contents

List of Figures

List of Tables

Chapter 1

The Standard Model

1.1 Gauge field theory

> *... Soon after my seminar began, when I had written on the blackboard,*
>
> $$\left(\partial_\mu - i\epsilon \mathbf{B}_\mu\right)\psi$$
>
> *Pauli asked, "What is the mass of this field* $\mathbf{B}$ *?" I said we did not know. Then I resumed my presentation but soon Pauli asked the same question again. I said something to the effect that it was a very complicated problem, we had worked on it and had come to no definite conclusions. I still remember his repartee: "That is not sufficient excuse". I was so taken aback that I decided, after a few moments' hesitation, to sit down. There was general embarrassment. Finally Oppenheimer, who was chairman of the seminar, said "We should let Frank proceed". I then resumed and Pauli did not ask any more questions during the seminar.*
>
> — Chen-Ning Yang, on a seminar he gave at Princeton in 1954 [1]

The gauge invariance of a theory requires that the Lagrangian of that theory is invariant under the infinitesimal transformation on the matter field:

$$\delta\psi(x) = i\epsilon^\alpha(x) t_\alpha \psi(x), \tag{1.1}$$

where ϵ^α are infinitesimal parameters depending on the position in the spacetime; t_α are generators of a Lie group and satisfy commutation relations:

$$\left[t_\alpha, t_\beta\right] = iC^\gamma_{\alpha\beta} t_\gamma. \tag{1.2}$$

Any function of ψ that is invariant under the transformation 1.1 with ϵ constant would also be invariant under the transformation with ϵ as arbitrary functions of spacetime. However, if we want to construct a Lagrangian with the derivative term of ψ also involved, the transformation of the derivative would be:

$$\delta\left(\partial_\mu \psi(x)\right) = i\epsilon^\alpha(x) t_\alpha \left(\partial_\mu \psi(x)\right) + i\left(\partial_\mu \epsilon^\alpha(x)\right) t_\alpha \psi(x), \tag{1.3}$$

where the term involves $\partial_\mu \epsilon$ would generally break the invariance of the Lagrangian. To cancel the $\partial_\mu \epsilon$ term, we can add a new "gauge" field A_μ such that:

$$\delta A^\beta_\mu = \partial_\mu \epsilon^\beta + C^\beta_{\gamma\alpha} \epsilon^\alpha A^\gamma_\mu. \tag{1.4}$$

We can then construct a "covariant derivative":

$$D_\mu \psi = \partial_\mu \psi - iA^\beta_\mu t_\beta \psi, \tag{1.5}$$

whose transformation would be:

$$\delta\left(D_\mu \psi\right) = i\epsilon^\alpha t_\alpha \left(D_\mu \psi\right). \tag{1.6}$$

Furthermore, similar to the electromagnetic tensor in electrodynamics, we can define a field strength tensor $F^\lambda_{\mu\nu}$:

$$F^\lambda_{\mu\nu} = \partial_\mu A^\lambda_\nu - \partial_\nu A^\lambda_\mu + C^\lambda_{\alpha\beta} A^\alpha_\mu A^\beta_\nu, \tag{1.7}$$

whose infinitesimal transformation would be:

$$\delta F^\lambda_{\mu\nu} = \epsilon^\alpha C^\lambda_{\beta\alpha} F^\beta_{\mu\nu}. \tag{1.8}$$

Given the infinitesimal transformation rules in equations 1.1, 1.4, 1.6, and 1.8, for a finite transformation induced by $S \equiv \exp(i\epsilon^\alpha t_\alpha)$, the transformations of fields are:

$$\psi \to S\psi, \tag{1.9}$$

$$\mathbf{A}_\mu \to S\mathbf{A}_\mu S^{-1} - i(\partial_\mu S)S^{-1}, \tag{1.10}$$

$$\mathbf{F}_{\mu\nu} \to S\mathbf{F}_{\mu\nu}S^{-1}, \tag{1.11}$$

where $\mathbf{A}_\mu \equiv t_\alpha A^\alpha_\mu, \mathbf{F}_{\mu\nu} \equiv t_\alpha F^\alpha_{\mu\nu}$. In analogy to electrodynamics, we can write down a Lagrangian that is invariant under the gauge transformations:

$$\mathcal{L} \equiv -\frac{1}{4}F_{\alpha\mu\nu}F^{\mu\nu}_\alpha + \mathcal{L}_M(\psi, D_\mu\psi), \tag{1.12}$$

where $\mathcal{L}_M$ are terms involving matter fields ψ. For example, if ψ are Dirac fields, $\mathcal{L}_M$ could be:

$$\mathcal{L}_M = -\overline{\psi}(\not{D}_\mu + m)\psi. \tag{1.13}$$

From 1.12, the Euler-Lagrangian equation yields:

$$\partial_\mu F^{\mu\nu}_\alpha = F^{\nu\mu}_\lambda C_{\lambda\alpha\beta}A_{\beta\mu} + i\frac{\partial\mathcal{L}_M}{\partial D_\nu\psi}t_\alpha\psi. \tag{1.14}$$

If we define current $j^\nu_\alpha \equiv F^{\nu\mu}_\lambda C_{\lambda\alpha\beta}A_{\beta\mu} + i\frac{\partial\mathcal{L}_M}{\partial D_\nu\psi}t_\alpha\psi$, we can have the current conservation:

$$\partial_\nu j^\nu_\alpha = 0, \tag{1.15}$$

which means the gauge charge $Q_\alpha = \int d^3x\ j^0_\alpha$ is conserved. This immediately has two important consequences in non-Abelian gauge theories: i) the gauge charge is gauge-dependent (i.e. it is not invariant under gauge transformations); and ii) the gauge field itself carries gauge charges (for example, in Quantum chromodynamics, gluons carry color charges).

The idea of non-Abelian gauge field theory was first published by Chen-Ning Yang and Robert Mills in 1954 [2]. But even before the paper was published, Pauli had raised the question on the mass of the gauge boson (as mentioned at the beginning of this section) which Yang and Mills could not answer at that time, they admitted in the paper that they "*have not been able to conclude anything about the mass*". Though it seemed that the gauge symmetry requires the gauge boson to be massless at the classical level, Yang and Mills didn't know how to renormalize the non-Abelian gauge theory and thus didn't know if the gauge boson is still massless at the quantum level. On the other hand, if the gauge boson is truly massless, it should have been discovered experimentally at that time, so the gauge theory seemed to be inconsistent with experimental observations.

Pauli's question proved to be at the core of the development of particle physics. Eighteen years later, the renormalizability of non-Abelian gauge theory was proved by t'Hooft and Veltman [3]. That is, if we start with a gauge field theory, the divergences in the loop diagrams can be systematically absorbed by counter terms in the "bare" Lagrangian in a way such that the gauge symmetry is **preserved**. At the same time, the mystery as to why no massless non-Abelian gauge boson is observed experimentally was (at least partially) solved by two other important concepts developed in the 1950s to the 1970s, one is **symmetry breaking**, the other one is **asymptotic freedom** (and confinement). Together with numerous experimental breakthroughs, these concepts led to a triumphant theory that describes strong, weak, and electromagnetic interactions — the standard model, the core structure of which will be illustrated in the rest of this chapter.

1.2 Spontaneously broken global symmetries

1.2.1 Nambu-Goldstone bosons and and Goldstone-Salam-Weinberg theorem

Suppose the effective action of a theory $\Gamma[\phi]$ is invariant under the infinitesimal transformation corresponding to a continuous global symmetry:

$$\delta\phi_l = i\epsilon t_{lm}\phi_m, \tag{1.16}$$

where ϵ is a constant infinitesimal parameter, and t is a generator of the symmetry group. We should then have:

$$\int \frac{\delta\Gamma[\phi]}{\delta\phi_l} t_{lm}\phi_m \, d^4x = 0. \tag{1.17}$$

When $\phi(x)$ is constant, i.e. $\partial_i\phi = 0$, $\Gamma[\phi]$ can be written as:

$$\Gamma[\phi] = -\mathcal{V}V(\phi), \tag{1.18}$$

where $\mathcal{V}$ is the spacetime volume, and $V(\phi)$ is called the effective potential of ϕ. Equation 1.17 then becomes:

$$\frac{\partial V(\phi)}{\partial\phi_l} t_{lm}\phi_m = 0. \tag{1.19}$$

Differentiating this equation with respect to ϕ_n yields:

$$\frac{\partial V}{\partial\phi_l} t_{ln} + \frac{\partial^2 V}{\partial\phi_l\partial\phi_n} t_{lm}\phi_m = 0. \tag{1.20}$$

Now evaluating this equation at a vacuum state $\phi = \langle\phi\rangle_0$, since the vacuum state should be at a minimum of the effective potential $V(\phi)$, we have:

$$\frac{\partial V}{\partial\phi}|_{\phi=\langle\phi\rangle_0} = 0. \tag{1.21}$$

Therefore, equation 1.20 becomes:

$$\frac{\partial^2 V}{\partial\phi_l\partial\phi_n}\bigg|_{\phi=\langle\phi\rangle} t_{lm}\langle\phi_m\rangle_0 = 0 \tag{1.22}$$

Now that the symmetry is broken by the vacuum state, i.e. $t_{lm}\langle\phi_m\rangle_0 \neq 0$, this means the matrix $\frac{\partial^2 V}{\partial\phi_l\partial\phi_n}\Big|_{\phi=\langle\phi\rangle_0}$ has an eigenvalue of zero. On the other hand, (roughly speaking) $\frac{\partial^2 V}{\partial\phi_l\partial\phi_n}\Big|_{\phi=\langle\phi\rangle_0}$ corresponds to the mass matrix of the theory. So we can conclude that there exist massless particles — so-called *Nambu-Goldstone bosons*, which are at the directions defined by the linear combinations of $t_{lm}\langle\phi_m\rangle_0$.

A more rigorous proof was provided by Goldstone, Salam and Weinberg [4], where they stated:

> *If there is continuous symmetry transformation under which the Lagrangian is invariant, then either the vacuum state is also invariant under the transformation, or there must exist spinless particles of zero mass.*

1.2.2 Pseudo-Goldstone bosons, $SU(3) \times SU(3)$ flavor symmetry

The first successful application of spontaneous symmetry breaking in particle physics was the description of pions and their interactions. In 1961, Nambu and Jona-Lasinio [5, 6] suggested that pions can be viewed as (pseudo-)Goldstone bosons resulting from the spontaneous breaking of a $SU(2) \times SU(2)$ symmetry, where the $SU(2) \times SU(2)$ symmetry is **approximate** in the sense that it is also *explicitly* broken by small mass terms of underlying fundamental fermion fields (i.e. quarks). Since the symmetry we start with is not exact but approximate, the (pseudo-)Goldstone bosons are no longer massless, and their masses can be determined from the structure of the symmetry and the small mass terms of the underlying quarks.

The $SU(2) \times SU(2)$ symmetry Nambu and Jona-Lasinio considered can be extended to a larger $SU(3) \times SU(3)$ symmetry, which can be used to describe other light-flavor mesons like K and η. To show that, consider the color-gauge interactions of the three light-flavor quarks — u, d, and s:

$$\mathcal{L} = -\bar{\mathrm{u}}\not{D}_\mu \mathrm{u} - \bar{\mathrm{d}}\not{D}_\mu \mathrm{d} - \bar{\mathrm{s}}\not{D}_\mu \mathrm{s} + \cdots . \tag{1.23}$$

The details of the gauge symmetry are not important here. In the limit where u, d, and s are massless, the Lagrangian has a global $SU(3)_V \times SU(3)_A$ symmetry if we build a triplet from u, d, and s:

$$q \equiv \begin{pmatrix} \mathrm{u} \\ \mathrm{d} \\ \mathrm{s} \end{pmatrix}, \tag{1.24}$$

$$SU(3)_V : \quad q \to \exp\left(i\theta_V^i \lambda_i\right) q, \tag{1.25}$$

$$SU(3)_A : \quad q \to \exp\left(i\theta_A^i \lambda_i \gamma_5\right) q, \tag{1.26}$$

where λ_i are the eight Gell-Mann matrices for $SU(3)$ group. In reality we know that quarks indeed have mass, therefore this symmetry is explicitly broken by the quark mass terms:

$$\mathcal{L}_m = -m_{\mathrm{u}}\bar{\mathrm{u}}\mathrm{u} - m_{\mathrm{d}}\bar{\mathrm{d}}\mathrm{d} - m_{\mathrm{s}}\bar{\mathrm{s}}\mathrm{s}. \tag{1.27}$$

However, given that m_{u}, m_{d}, and m_{s} are small compared to the QCD scale $\Lambda_{\mathrm{QCD}} \sim$ 218 MeV, the $SU(3) \times SU(3)$ symmetry still *approximately* holds.

On the other hand, the axial $SU(3)_A$ transformation changes the parity of a given state, if it is unbroken, then each hadron state should have a partner with opposite parity, which is in conflict with experimental observations. Therefore it is natural

to assume that $SU(3)_A$ symmetry is spontaneously broken, leaving us the $SU(3)_V$ symmetry (which is exactly the same symmetry Gell-Mann and Ne'eman proposed for baryons and mesons).

For the quark field $q(x)$, we can define a new field $\tilde{q}(x)$ such that it is Goldstone-free (i.e. it is invariant under the $SU(3)_A$ transformation):

$$\tilde{q}(x) = \exp\left(i\epsilon^i(x)\lambda_i\gamma_5\right) q(x). \tag{1.28}$$

Then $\epsilon^i(x)$ parameterize the directions where the symmetries are broken, therefore they can be identified as our Goldstone boson fields. If we define a matrix $U(x) = \exp(2i\epsilon^i\lambda_i)$, it can be shown that [7] $U(x)$ transforms under $SU(3)_V \times SU(3)_A$ like:

$$U(x) \to \exp\left(i(\theta_V^i - \theta_A^i)\lambda_i\right) U(x) \exp\left(-i(\theta_V^i + \theta_A^i)\lambda_i\right). \tag{1.29}$$

We can then write down a general "effective Lagrangian" that is invariant under the $SU(3)_V \times SU(3)_A$ symmetry and only involves Goldstone boson fields:

$$\begin{aligned}\mathcal{L}_{\text{eff}} = &-\frac{1}{16}f_\pi^2 \text{Tr}\left[\partial_\mu U \partial^\mu U^\dagger\right] + L_1 \text{Tr}\left[(\partial_\mu U \partial^\mu U^\dagger)^2\right] \\ &+ L_2 \text{Tr}\left[\partial_\mu U \partial_\nu U^\dagger\right] \text{Tr}\left[\partial^\mu U \partial^\nu U^\dagger\right] + \cdots .\end{aligned} \tag{1.30}$$

The Goldstone fields can be mapped into the meson fields we know as:

$$\sum_i \epsilon^i \lambda_i = \frac{\sqrt{2}}{f_\pi} \begin{pmatrix} \frac{1}{\sqrt{2}}\pi^0 + \frac{1}{\sqrt{6}}\eta^0 & \pi^+ & K^+ \\ \pi^- & -\frac{1}{\sqrt{2}}\pi^0 + \frac{1}{\sqrt{6}}\eta^0 & K^0 \\ K^- & \overline{K}^0 & -\sqrt{\frac{2}{3}}\eta^0 \end{pmatrix} \tag{1.31}$$

The effective Lagrangian 1.30 doesn't contain mass terms for Goldstone boson fields, which is in agreement with the Goldstone-Salam-Weinberg theorem. However, the $SU(3) \times SU(3)$ is also explicitly broken by the (small) quark mass terms $\mathcal{L}_m$ 1.27, which can be written as:

$$\mathcal{L}_m = -\overline{q}Mq = -\overline{\tilde{q}} \exp\left(-i\epsilon^i\lambda_i\gamma_5\right) M \exp\left(-i\epsilon^i\lambda_i\gamma_5\right) \tilde{q}, \tag{1.32}$$

where M is the mass matrix for quarks:

$$M = \begin{pmatrix} m_{\mathrm{u}} & 0 & 0 \\ 0 & m_{\mathrm{d}} & 0 \\ 0 & 0 & m_{\mathrm{s}} \end{pmatrix}. \tag{1.33}$$

At the same time, by requiring that the $SU(3)_V$ is unbroken and the vacuum alignment condition [8] (i.e. the vacuum state should be at a minimum of the effective potential) holds, the vacuum state of QCD should satisfy:

$$\langle \bar{\tilde{q}}_m \gamma_5 \tilde{q}_n \rangle_0 = 0, \quad \langle \bar{\tilde{q}}_m \tilde{q}_n \rangle_0 = -v_{\mathrm{QCD}} \delta_{mn}. \tag{1.34}$$

Take the vacuum expectation of $\mathcal{L}_m$ and expand to the second order in meson fields, we can find out that the mass terms of the mesons are:

$$\begin{aligned} -2v_{\mathrm{QCD}} \mathrm{Tr}\left[\sum_{ij} \epsilon^i \lambda_i M \epsilon^j \lambda_j\right] = &-\frac{4v_{\mathrm{QCD}}}{f_\pi^2}\left[m_{\mathrm{u}}\left(\frac{1}{\sqrt{2}}\pi^0 + \frac{1}{\sqrt{6}}\eta^0\right)^2 + (m_{\mathrm{u}} + m_{\mathrm{d}})\pi^+\pi^- \right. \\ &+ (m_{\mathrm{u}} + m_{\mathrm{s}})K^+K^- + m_{\mathrm{d}}\left(-\frac{1}{\sqrt{2}}\pi^0 + \frac{1}{\sqrt{6}}\eta^0\right)^2 \\ &\left. + (m_{\mathrm{d}} + m_{\mathrm{s}})K^0\overline{K}^0 + \frac{2}{3}m_{\mathrm{s}}(\eta^0)^2\right], \end{aligned} \tag{1.35}$$

from which we can read out the masses of different mesons:

$$m_\pi^2 = \frac{4v_{\mathrm{QCD}}}{f_\pi^2}(m_{\mathrm{u}} + m_{\mathrm{d}}), \tag{1.36}$$

$$m_{K^+}^2 = \frac{4v_{\mathrm{QCD}}}{f_\pi^2}(m_{\mathrm{u}} + m_{\mathrm{s}}), \tag{1.37}$$

$$m_{K^0}^2 = \frac{4v_{\mathrm{QCD}}}{f_\pi^2}(m_{\mathrm{d}} + m_{\mathrm{s}}), \tag{1.38}$$

$$m_{\eta^0}^2 = \frac{4v_{\mathrm{QCD}}}{f_\pi^2}\left(\frac{m_{\mathrm{u}} + m_{\mathrm{d}} + 4m_{\mathrm{s}}}{3}\right). \tag{1.39}$$

Taking account of the correction due to the electromagnetic interactions, the masses of $\pi^{\pm}$ and $K^{\pm}$ become:

$$m^2_{\pi^{\pm}} = \frac{4v_{\rm QCD}}{f_\pi^2}(m_{\rm u} + m_{\rm d}) + \Delta_{em}, \tag{1.40}$$

$$m^2_{K^{\pm}} = \frac{4v_{\rm QCD}}{f_\pi^2}(m_{\rm u} + m_{\rm s}) + \Delta_{em}. \tag{1.41}$$

We can then derive predictions on quark mass ratios from the pion and kaon masses:

$$\frac{m_{\rm d}}{m_{\rm s}} = \frac{m^2_{K^0} + m^2_{\pi^+} - m^2_{K^+}}{m^2_{K^0} - m^2_{\pi^+} + m^2_{K^+}}, \quad \frac{m_{\rm u}}{m_{\rm s}} = \frac{2m^2_{\pi^0} - m^2_{K^0} - m^2_{\pi^+} + m^2_{K^+}}{m^2_{K^0} - m^2_{\pi^+} + m^2_{K^+}} \tag{1.42}$$

1.3 Spontaneously broken gauge symmetries

Though pseudo-Goldstone bosons accompanied with spontaneously broken *approximate* symmetries played important roles in describing mesons/baryons and their interactions, the true massless Goldstone bosons associated with broken *exact* symmetries were never discovered experimentally. In 1964, Brout and Englert [9], Higgs [10], Guralnik, Hagen and Kibble [11] realized that the Goldstone-Salam-Weinberg theorem can be bypassed if the fundamental exact symmetries are not global but gauge (i.e. local) symmetries, where the degree-of-freedoms corresponding to the Goldstone bosons become the helicity-0 components of the gauge fields, making the gauge fields become massive vector fields. Thus the massless Goldstone bosons are exorcised, and the gauge fields acquire masses in the end. This is called the Higgs mechanism, which is crucial for the electroweak unification.

In a theory with gauge symmetry, the Higgs mechanism proposes the existence of **elementary scalar** fields ϕ_n, whose vacuum states $\langle\phi\rangle_0$ broke the gauge symmetry:

$$t^{\alpha}_{mn}\langle\phi_n\rangle_0 \neq 0, \tag{1.43}$$

then there always exists a gauge transformation $\phi \to \tilde{\phi}$:

$$\tilde{\phi}_m(x) = \gamma_{mn}(x)\phi_n(x), \tag{1.44}$$

such that the Goldstone modes are removed:

$$\tilde{\phi}_m(x)[it^\alpha]_{mn}\langle\phi_n\rangle_0 = 0. \tag{1.45}$$

This condition is called the *unitarity gauge* [12]. Note we are taking real representation here. Even if ϕ_m are complex fields, real representation can still be achieved by treating the real and imaginary parts of ϕ as separate components — $\phi = (\mathrm{Re}\phi, \mathrm{Im}\phi)$. The existence of the unitarity gauge can be proved as following:

Considering the quantity $K \equiv (g(\theta)\phi)^T v$, where $v = \langle\phi\rangle_0$, and $g(\theta)$ is an arbitrary gauge transformation belongs to the gauge group, parameterized as:

$$g(\theta) \equiv \exp\left(i\theta_\alpha t^\alpha\right). \tag{1.46}$$

When the gauge group is compact, K must have a minimum, which means there exists a θ^*, such that:

$$0 = \left.\frac{\partial K(\theta)}{\partial\theta_\alpha}\right|_{\theta=\theta^*} = \left(\left.\frac{\partial g}{\partial\theta_\alpha}\right|_{\theta=\theta^*}\phi\right)^T v. \tag{1.47}$$

On the other hand, we have $\frac{\partial g}{\partial\theta_\alpha} = i\sum_\beta N_{\alpha\beta}t^\beta g$, where $N_{\alpha\beta}$ is a non-singular matrix, therefore we have:

$$\left(\sum_\beta N_{\alpha\beta}it^\beta g(\theta^*)\phi\right)^T v = 0. \tag{1.48}$$

Since this equation holds for arbitrary α, and $N_{\alpha\beta}$ is non-singular, we must have:

$$\left(it^\alpha g(\theta^*)\phi\right)^T v = 0 \tag{1.49}$$

Comparing with equations 1.44 and 1.45, we can see that $\gamma = g(\theta^*)$. Therefore, *the unitarity gauge condition can always be satisfied by choosing an appropriate gauge transformation.*

The benefit of the unitarity gauge is that the unphysical Goldstone bosons are removed, and the physical consequences of the spontaneous gauge symmetry breaking are more obvious. Assuming we have chosen the unitarity gauge, the gauge interaction terms for ϕ can be written as:

$$\mathcal{L} = -\frac{1}{2}\sum_m \left(\partial_\mu \phi_m - [it^\alpha]_{mn} A_\alpha \phi_n\right)^2 . \tag{1.50}$$

Now expand ϕ around its vacuum expectation value v:

$$\phi \equiv v + \phi', \tag{1.51}$$

the terms in the Lagrangian 1.50 to the second order in ϕ' and A can be written as:

$$\mathcal{L}_{\text{QUAD}} = -\frac{1}{2}\sum_m \left(\partial_\mu \phi'_m - [it^\alpha]_{mn} A_\alpha v_n\right)^2 . \tag{1.52}$$

According to the unitarity gauge condition, the terms proportional to $\phi_m [it]^\alpha_{mn} v_n$ vanish (therefore $(\partial_\mu \phi'_m)[it]^\alpha_{mn} v_n$ also vanishes), leaving us:

$$\mathcal{L}_{\text{QUAD}} = -\frac{1}{2}\sum_m \left(\partial_\mu \phi'_m\right)^2 - \frac{1}{2} M_{\alpha\beta} A_{\alpha\mu} A^\mu_\beta, \tag{1.53}$$

where

$$M_{\alpha\beta} \equiv \sum_{mnl} [it^\alpha]_{mn} [it^\beta]_{ml} v_n v_l. \tag{1.54}$$

$M_{\alpha\beta}$ is then identified as the mass matrix of gauge fields A^μ_α. Now for an arbitrary linear combination of gauge fields $B^\mu \equiv \sum_\alpha c_\alpha A^\mu_\alpha$ (with the normalization condition $\sum_\alpha c_\alpha^2 = 1$), the mass term for B^μ is proportional to:

$$\sum_{\alpha\beta} c_\alpha M_{\alpha\beta} c_\beta = \left(\sum_\alpha c_\alpha \cdot it^\alpha v\right)^2 \geq 0, \tag{1.55}$$

which vanishes if and only if the symmetry generated by $\sum_\alpha c_\alpha \cdot it^\alpha$ is unbroken, i.e. $\sum_\alpha c_\alpha \cdot it^\alpha v = 0$. Therefore, we can conclude that *in the spontaneous gauge symmetry breaking, the gauge fields corresponding to the broken symmetries become massive, while the gauge fields corresponding to the unbroken symmetries remain massless.*

1.4 The electroweak theory

In 1967, combining the ideas of gauge symmetry and spontaneous symmetry breaking, Weinberg established the theory that unifies electromagnetic and weak interactions [13], predicting the existence of neutral current, W boson, Z boson, and what now is called the "Higgs boson." All these predictions were later confirmed experimentally, by Gargamelle [14], UA1 [15, 16, 17, 18], ATLAS [19], and CMS [20]. Similar models of electroweak unification were also established independently by Glashow [21] and Salam [22].

Starting from the simplest case where we only consider electron e and its neutrino ν_e, we can build a doublet:

$$\ell = \begin{pmatrix} \nu_e \\ e \end{pmatrix}. \tag{1.56}$$

The gauge group proposed for the electroweak interaction is $SU(2)_L \times U(1)_Y$, where the generators of $SU(2)_L$ and $U(1)_Y$ are:

$$SU(2)_L: \quad \vec{t}_L = \frac{g}{2} P_L \vec{\sigma}, \tag{1.57}$$

$$U(1)_Y: \quad t_Y = g' \left[-\frac{1}{2} P_L - P_R \begin{pmatrix} 0 & 0 \\ 0 & 1 \end{pmatrix} \right], \tag{1.58}$$

where g and g' are coupling constants, $\vec{\sigma}$ are Pauli matrices, P_L and P_R are the projection operators to the left-handed/right-handed components of a fermion:

$$P_L = \frac{1}{2}(1+\gamma_5), \quad P_R = \frac{1}{2}(1-\gamma_5). \tag{1.59}$$

It is worthwhile to point out that the generator corresponding to the electromagnetic symmetry $U(1)_{em}$ can be built based on a linear combination of t_{3L} and t_Y:

$$q = \mathbf{e}\begin{pmatrix} 0 & 0 \\ 0 & -1 \end{pmatrix} = \mathbf{e}\left(\frac{t_{3L}}{g} + \frac{t_Y}{g'}\right). \tag{1.60}$$

The gauge interaction terms for the leptons can be written as:

$$\mathcal{L}_\ell = -\bar{\ell}(\not{\partial} - i\vec{\not{A}} \cdot \vec{t}_L - i\not{B} t_Y)\ell. \tag{1.61}$$

Since photons, which are the gauge fields of electromagnetic interaction, are massless, we would like the $SU(2)_L \times U(1)_Y$ symmetry to be spontaneously broken to the electromagnetic symmetry $U(1)_{em}$. It is helpful to recombine the gauge fields $\vec{A}^\mu$ and B^μ:

$$W^{+\mu} = \frac{1}{\sqrt{2}}(A_1^\mu + iA_2^\mu), \tag{1.62}$$

$$W^{-\mu} = \frac{1}{\sqrt{2}}(A_1^\mu - iA_2^\mu), \tag{1.63}$$

$$Z^\mu = \cos\theta A_3^\mu - \sin\theta B^\mu, \tag{1.64}$$

$$A^\mu = \sin\theta A_3^\mu + \cos\theta B^\mu. \tag{1.65}$$

Now we would like to identify A^μ in equation 1.65 as the photon in electromagnetic theory, the generator it's coupled with is:

$$q = \sin\theta t_{3L} + \cos\theta t_Y. \tag{1.66}$$

Compared with equation 1.60, we can get:

$$g = \mathbf{e}/\sin\theta, \quad g' = \mathbf{e}/\cos\theta. \tag{1.67}$$

The gauge interaction terms 1.61 can then be written as:

$$\begin{aligned}\mathcal{L}_\ell =& \frac{g}{\sqrt{2}}(\overline{e}\not{W}^+ P_L \nu_e) + \frac{g}{\sqrt{2}}(\overline{\nu}_e \not{W}^- P_L e) \\ & - \frac{1}{2}\sqrt{g^2+g'^2}\overline{\nu}_e \not{Z} P_L \nu_e + \frac{g^2-g'^2}{2\sqrt{g^2+g'^2}}\overline{e}\not{Z} P_L e + g'\overline{e}\not{Z} P_R e \\ & - \mathbf{e}(\overline{e}\not{A} e) \end{aligned} \tag{1.68}$$

We know that electron has mass, but the (Dirac) mass term of electron can not be added to the Lagrangian directly, otherwise it would *explicitly* break the chiral $SU(2)_L$ symmetry. Instead we introduce a scalar doublet:

$$\phi \equiv \begin{pmatrix} \phi^+ \\ \phi^0 \end{pmatrix}, \tag{1.69}$$

as well as a "Yukawa" coupling:

$$\mathcal{L}_Y = -Y_e \overline{\begin{pmatrix} \nu_e \\ e \end{pmatrix}_L} \begin{pmatrix} \phi^+ \\ \phi^0 \end{pmatrix} e_R + \text{H.c.}. \tag{1.70}$$

Given that $\mathcal{L}_Y$ should be invariant under the $SU(2)_L \times U(1)_Y$ group, the transformation rule for ϕ can be determined as:

$$SU(2)_L: \quad \vec{t}_L^{\phi} = \frac{g}{2}\vec{\sigma}, \tag{1.71}$$

$$U(1)_Y: \quad t_Y^{\phi} = \frac{g'}{2}\begin{pmatrix} 1 & 0 \\ 0 & 1 \end{pmatrix} \tag{1.72}$$

The electric charge matrix for ϕ is then:

$$q^{\phi} = \mathbf{e}\left(\frac{t_{3L}^{\phi}}{g} + \frac{t_Y^{\phi}}{g'}\right) = \mathbf{e}\begin{pmatrix} 1 & 0 \\ 0 & 0 \end{pmatrix}. \tag{1.73}$$

Therefore ϕ^+ carries an electric charge of $+\mathbf{e}$, while ϕ^0 is neutral. The most general renormalizable Lagrangian for ϕ with $SU(2)_L \times U(1)_Y$ gauge symmetry is:

$$\mathcal{L}_\phi = -\frac{1}{2}|D_\mu \phi|^2 - \frac{\mu^2}{2}\phi^\dagger\phi - \frac{\lambda}{4}(\phi^\dagger\phi)^2, \quad D_\mu = \partial_\mu - i\vec{A}_\mu \cdot \vec{t}_L^{\phi} - iB_\mu t_Y^{\phi}. \tag{1.74}$$

When $\mu^2 < 0$, the vacuum expectation value of ϕ is non-zero:

$$|\langle\phi\rangle_0|^2 \equiv v^2 = |\mu^2|/\lambda. \tag{1.75}$$

At the same time, we hope $U(1)_{em}$ is unbroken, which means $q^\phi\langle\phi\rangle_0 = 0$, so we must have:

$$\langle\phi^+\rangle_0 = 0, \quad |\langle\phi^0\rangle_0| = v. \tag{1.76}$$

Furthermore, with the $SU(2)_L \times U(1)_Y$ symmetry, we have the freedom to choose $\langle\phi^0\rangle_0$ to be real, so the vacuum expectation value of ϕ can be written as:

$$\langle\phi\rangle_0 = \begin{pmatrix} 0 \\ v \end{pmatrix}. \tag{1.77}$$

Now writing ϕ and it^ϕ in the real representation:

$$\phi = \begin{pmatrix} \mathrm{Re}\phi^+ \\ \mathrm{Im}\phi^+ \\ \mathrm{Re}\phi^0 \\ \mathrm{Im}\phi^0 \end{pmatrix}, \quad \langle\phi\rangle_0 = \begin{pmatrix} 0 \\ 0 \\ v \\ 0 \end{pmatrix}, \quad it^\phi_{1L} = \frac{g}{2}\begin{pmatrix} 0 & 0 & 0 & -1 \\ 0 & 0 & 1 & 0 \\ 0 & -1 & 0 & 0 \\ 1 & 0 & 0 & 0 \end{pmatrix}, \quad \cdots \tag{1.78}$$

Applying the unitarity gauge condition $\phi^T[it^\phi]\langle\phi\rangle_0 = 0$, we can find out that the only physical field is $\mathrm{Re}\phi^0$, which is our **Higgs boson**.

Accompanied with the spontaneous symmetry breaking caused by $\langle\phi\rangle_0$, the mass terms for W and Z bosons can be obtained from the Lagrangian 1.74, which are:

$$-\frac{1}{2}\left|\left(\vec{A}_\mu \cdot \vec{t}^\phi_L + B_\mu t^\phi_Y\right)\langle\phi\rangle_0\right|^2 = -\frac{v^2 g^2}{4}W^+_\mu W^{-\mu} - \frac{v^2}{8}(g^2 + g'^2)Z_\mu Z^\mu. \tag{1.79}$$

Therefore the masses of W and Z bosons are:

$$m_W = \frac{vg}{2}, \quad m_Z = \frac{v\sqrt{g^2 + g'^2}}{2}. \tag{1.80}$$

The mass of the electron can be obtained from the Yukawa coupling 1.70, which is:

$$m_e = Y_e v \tag{1.81}$$

Since the lepton numbers are conserved separately for each flavor (except in the case of neutrino oscillation), the electroweak theory of electron and its neutrino can be straightforwardly extended to other lepton flavors. For the quark sector, at the time when the electroweak theory was established, the only quark flavors people knew were u, d, and s. However, with only three quark flavors, the electroweak theory predicted the Z boson mediation would lead to flavor-changing neutral current (FCNC) processes, resulting in much larger rates than what were observed experimentally in processes like $K^0 - \overline{K}^0$ oscillations and $K^0 \to \mu^+\mu^-$ decays. To avoid FCNCs, in 1970, Glashow, Iliopoulos and Maiani proposed the existence of the fourth quark – charm quark [23]. The meson formed by charm quark-antiquark pair was soon discovered by groups led by Samuel Ting [24] and Burton Ritcher [25], which was the first triumph of the electroweak theory and the standard model.

For the electroweak interactions of quarks, we can build a doublet with up and down types of quarks:

$$Q = \begin{pmatrix} U \\ D \end{pmatrix}. \tag{1.82}$$

The $SU(2)_L \times U(1)_Y$ transformations for Q are:

$$SU(2)_L: \quad \vec{t}_L^{\,Q} = \frac{g}{2} P_L \vec{\sigma}, \tag{1.83}$$

$$U(1)_Y: \quad t_Y^Q = g' \left[\frac{1}{6} P_L + \frac{1}{3} P_R \begin{pmatrix} 2 & 0 \\ 0 & -1 \end{pmatrix} \right] \tag{1.84}$$

The electric charge matrix for quarks are then:

$$q^Q = \mathbf{e}\left(\frac{t^Q_{3L}}{g} + \frac{t^Q_Y}{g'}\right) = \mathbf{e}\begin{pmatrix} \frac{2}{3} & 0 \\ 0 & -\frac{1}{3} \end{pmatrix}. \tag{1.85}$$

That is, the up type quarks carry electric charges of $+2/3\mathbf{e}$, while the down type quarks carry electric charges of $-1/3\mathbf{e}$. In order to give masses to both up and down types of quarks, we can construct a new scalar doublet:

$$\widetilde{\phi} \equiv i\sigma_2\phi^* = \begin{pmatrix} \phi^{0*} \\ -\phi^{+*} \end{pmatrix}. \tag{1.86}$$

Utilizing $\sigma_2\sigma_j^* + \sigma_j\sigma_2 = 0$, we can find out the $SU(2)_L \times U(1)_Y$ transformations for $\widetilde{\phi}$ are:

$$SU(2)_L: \quad \vec{t}_L^{\widetilde{\phi}} = \frac{g}{2}\vec{\sigma} \tag{1.87}$$

$$U(1)_Y: \quad t_Y^{\widetilde{\phi}} = -\frac{g'}{2}\begin{pmatrix} 1 & 0 \\ 0 & 1 \end{pmatrix}. \tag{1.88}$$

Then the following "Yukawa" couplings for quarks are $SU(2)_L \times U(1)_Y$ invariant:

$$\mathcal{L}_{Y_Q} = -Y_D\overline{Q}_L\phi D_R - Y_U\overline{Q}_L\widetilde{\phi}U_R + \text{H.c.}. \tag{1.89}$$

Taking the vacuum expectation of $\mathcal{L}_{Y_Q}$, we can get the mass terms for quarks:

$$\mathcal{L}_{m_Q} = -M_D\overline{D}_L D_R - M_U\overline{U}_L U_R + \text{H.c.}, \tag{1.90}$$

where $M_D = vY_D$, $M_U = vY_U$. When there is more than one generations of quarks, M_D and M_U are matrices, whose indices represents the generation.

Now considering (global) unitary transformations for quark fields:

$$D_L \to S_{DL}D_L, \quad D_R \to S_{DR}D_R, \quad U_L \to S_{UL}U_L, \quad U_R \to S_{UR}U_R, \tag{1.91}$$

then the mass matrices M_D and M_U transforms like:

$$M_D \to S_{DL} M_D S_{DR}^\dagger, \quad M_U \to S_{UL} M_U S_{UR}^\dagger. \tag{1.92}$$

It can be proved that for any matrix M, there always exist unitary matrices S_L and S_R such that $S_L M S_R^\dagger$ is real and diagonal. Therefore we can always find appropriate S_{DL}, S_{DR}, S_{UL}, S_{UR} such that M_U and M_D are real and diagonal, which means U and D are at their mass eigenstates. However, with these transformations, the hadronic charged current that couples with W boson $J_{CC}^\mu = \overline{U}\gamma^\mu P_L D$ becomes:

$$J_{CC}^\mu = \overline{U}\gamma^\mu S_{UL} S_{DL}^\dagger P_L D, \tag{1.93}$$

while the hadronic neutral current J_{NC}^μ and electromagnetic current J_{EM}^μ are invariant. If we define $V \equiv S_{UL} S_{DL}^\dagger$, then we can have:

$$J_{CC}^\mu = \overline{U}\gamma^\mu V P_L D. \tag{1.94}$$

The matrix V is known as the **Cabibbo-Kobayashi-Maskawa (CKM) matrix**, which parameterizes the flavor mixing between different mass eigenstates of quarks. If V is real, then the CP-symmetry is conserved. When there are only two generations of quarks (i.e. V is a 2×2 matrix), it is always possible to let V become real (by adjusting the phases of the quark fields such that the mass matrices M_D and M_U are invariant). However, when there are three or more generations of quarks, it is no longer always possible to make V become real by adjusting the phases of the quark fields, therefore the CP-symmetry could be violated in the electroweak interactions. Indeed, CP-violation in weak interactions was discovered by Cronin and Fitch [26] in 1964, Kobayashi and Maskawa [27] realized that it requires the existence of the third generation of quarks if the electroweak theory holds. The existence of the third generation of quarks — top and bottom quarks — was later confirmed experimentally [28, 29, 30].

With three generations of quarks including u, d, c, s, t, and b quarks, the CKM matrix can be parameterized as:

$$
\begin{aligned}
V &\equiv \begin{pmatrix} V_{\mathrm{ud}} & V_{\mathrm{us}} & V_{\mathrm{ub}} \\ V_{\mathrm{cd}} & V_{\mathrm{cs}} & V_{\mathrm{cb}} \\ V_{\mathrm{td}} & V_{\mathrm{ts}} & V_{\mathrm{tb}} \end{pmatrix} \\
&= \begin{pmatrix} c_{12}c_{13} & s_{12}c_{13} & s_{13}e^{-i\delta} \\ -s_{12}c_{13} - c_{12}s_{23}s_{13}e^{i\delta} & c_{12}c_{23} - s_{12}s_{23}s_{13}e^{i\delta} & s_{23}c_{13} \\ s_{12}s_{23} - c_{12}c_{23}s_{13}e^{i\delta} & -c_{12}s_{23} - s_{12}c_{23}s_{13}e^{i\delta} & c_{23}c_{13} \end{pmatrix},
\end{aligned} \tag{1.95}
$$

where $c_{ij} = \cos\theta_{ij}$, $s_{ij} = \sin\theta_{ij}$, and θ_{ij} are the mixing angles between different generations; δ is the CP-phase, which indicates the magnitude of the weak CP-violation.

1.5 Quantum chromodynamics

Quantum chromodynamics (QCD) is the gauge field theory that describes the strong interactions, based on a $SU(3)$ gauge group. In QCD, in addition to the flavors, quarks can carry three "color" charges – red, green, and blue – which form a fundamental representation of $SU(3)$ group. One of the first evidences for the existence of the three "color" charges came from the studies on $\pi^0 \to \gamma\gamma$ decay. As discussed in Section 1.2.2, π^0 is one of the pseudo-Goldstone bosons corresponding to the flavor $SU(3)_A$ symmetry. More specifically, it corresponds to the chiral symmetry $\delta q = i\theta_A\gamma_5\lambda_3 q$, which can also be written as:

$$\delta \mathrm{u} = i\theta_A\gamma_5 \mathrm{u}, \quad \delta \mathrm{d} = -i\theta_A\gamma_5 \mathrm{d}. \tag{1.96}$$

Such symmetry could also be broken by the so-called **chiral anomaly** [31, 32, 33], which was first discovered by Bell, Jackiw, and Adler. That is, in the Feynman path

integral for fermion fields:

$$S[\psi] = \int \mathcal{D}\overline{\psi}\mathcal{D}\psi \ \exp\left\{ i \int d^4x \ \mathcal{L}(\psi, D_\mu\psi) \right\}, \tag{1.97}$$

the measure $\mathcal{D}\overline{\psi}\mathcal{D}\psi$ is generally not invariant under chiral transformations. Therefore, even if the classical action $I[\psi] = \int d^4x \ \mathcal{L}(\psi, D_\mu\psi)$ is invariant under a given chiral transformation, the chiral symmetry could still be broken at the quantum level. In the case of the neutral pion π^0, the chiral anomaly means the axial (i.e. chiral) current corresponding to the pion production is no longer conserved, and it leads to a significant rate of $\pi^0 \to \gamma\gamma$ decay when coupled with photons. The theoretical calculations based on chiral anomaly at one-loop level (the results are actually one-loop exact) yield a decay rate for π^0 as:

$$\Gamma(\pi^0 \to \gamma\gamma) = \left(\frac{N_c}{3}\right)^2 \times 1.11 \times 10^{16} s^{-1}, \tag{1.98}$$

where N_c is the number of additional degree-of-freedoms for quarks. The experimental value of $\Gamma(\pi^0 \to \gamma\gamma)$ is $(1.16 \pm 0.02) \times 10^{16} s^{-1}$, therefore we must have $N_c = 3$ in order to let the theoretical calculation and the experimental measurement be consistent. Indeed, the numerical values for $\pi^0 \to \gamma\gamma$ decay motivated Gross and Wilczek [34], Fritzsch, Gell-Mann and Leutwyler [35] to propose the $SU(3)$ gauge symmetry with three "color" charges for strong interactions.

With the $SU(3)_c$ gauge symmetry, the Lagrangian for QCD can be written as:

$$\mathcal{L}_{\text{QCD}} = -\frac{1}{4} F_\alpha^{\mu\nu} F_{\alpha\mu\nu} - \overline{q}\left[\partial\!\!\!/ - i\frac{g_c}{2} A\!\!\!/_\alpha \lambda_\alpha + M\right] q, \tag{1.99}$$

where A_α^μ is the gauge field for the $SU(3)$ color gauge symmetry — "gluon," g_c is the coupling constant of QCD. A more commonly used number is the so-called "strong coupling constant" α_s, defined as:

$$\alpha_s \equiv \frac{g_c^2}{4\pi}. \tag{1.100}$$

The strong coupling constant α_s is in analogy with the "fine structure constant" $\alpha = \frac{e^2}{4\pi}$ in QED, and characterizes the scattering amplitudes of $2 \to 2$ scattering processes mediated by gluons.

For the renormalization of a given field theory, generally we start with a Lagrangian with bare fields, masses, and couplings, the bare Lagrangian can be written as the sum of a Lagrangian with renormalized quantities and counter terms:

$$\mathcal{L}(\phi_B, m_B, g_B) = \mathcal{L}_R(\phi_R, m_R, g_R) + \delta\mathcal{L}. \tag{1.101}$$

The renormalization procedure is then taken such that the ultraviolet divergences arising from the loop diagrams based on $\mathcal{L}_R$ are canceled by the counter terms $\delta\mathcal{L}$, therefore the observable physical quantities become finite and calculable. The renormalized constants (e.g. g_R, m_R) are generally fixed to satisfy some "renormalization conditions." However, the physical observables should be independent on the choices of the renormalization condition. Therefore in stead of the renormalized coupling constants g_R, it is usually more useful to define some "effective coupling constants" g_μ as the amplitudes of the relevant physics processes (more strictly speaking, the renormalized Green's functions) measured at momenta characterized by some energy scale μ. The effective coupling constants g_μ obey the so-called *Renormalization Group Equation* [36, 37, 38, 39, 40, 41]:

$$\mu \frac{d}{d\mu} g_\mu = \beta(g_\mu). \tag{1.102}$$

$\beta(g_\mu)$ can be computed perturbatively and are deeply connected to the renormalization procedure. For example, in the "dimensional regularization" method [3] for renormalization, where the calculations are done at the $4 - \epsilon$ dimension, the diver-

gences in the loop diagrams can then be described by a power series of $1/\epsilon$:

$$g_B = g_R + \sum_{n=1}^{\infty} b_n(g_R) \left(\frac{1}{\epsilon}\right)^n . \tag{1.103}$$

It was shown that the β-function of g_μ can be determined by the coefficient of $1/\epsilon$ [42]. More importantly, for gauge couplings (e.g. e in QED, g_c in QCD), there exists a simple relation:

$$\beta(g) = \frac{1}{2}\left[b_1(g) - g\frac{\partial}{\partial g} b_1(g)\right] . \tag{1.104}$$

In 1973, Gross and Wilczek [34, 43], Politzer [44] calculated the β-function for non-Abelian gauge field theory with fermion fields:

$$\mathcal{L} = -\frac{1}{4} F_\alpha^{\mu\nu} F_{\alpha\mu\nu} - \overline{\psi}\left[\partial\!\!\!/ - ig A\!\!\!/_\alpha t_\alpha + M\right]\psi, \tag{1.105}$$

and found that for an $SU(N)$ theory, the β-function to the one-loop order is:

$$\beta(g) = -\frac{g^3}{4\pi^2}\left(\frac{11}{12}N - \frac{n_f}{6}\right), \tag{1.106}$$

where n_f is the number of flavors for the fermion fields. In QCD, we have $N = 3$, $n_f = 6$ (above the top quark mass threshold), and thus $\beta(g_c) = -\frac{7g_c^3}{16\pi^2} < 0$. According to the renormalization group equation, this means when $\mu \to \infty$, we will have $g_c(\mu) \to 0$. Such theories are said to be **asymptotically free**, and are consistent with the experimental observations for deep-inelastic e–p scattering [45, 46] that the strong interactions seemed to become weaker at higher energy scale. Furthermore, it was also proved that any renormalizable quantum field theory other than non-Abelian gauge field theories **can not** be asymptotically free [47]. So when QCD was shown to be asymptotically free, it was quickly accepted as the correct theory to describe strong interactions.

The QCD Lagrangian $\mathcal{L}_{\rm QCD}$ is CP-invariant if the mass matrix M is real. As discussed

in Section 1.4, we indeed have the freedom to choose M to be real in the electroweak symmetry breaking, therefore $\mathcal{L}_{\text{QCD}}$ automatically conserves CP-symmetry. However, we can also add another term $\mathcal{L}_\theta$ that satisfies $SU(3)_c$ gauge symmetry:

$$\mathcal{L}_\theta = -\frac{\theta}{64\pi^2}\epsilon^{\mu\nu\rho\sigma}F_{\alpha\mu\nu}F_{\alpha\rho\sigma}. \tag{1.107}$$

$\mathcal{L}_\theta$ doesn't have any dynamical effect since it is a total derivative (and thus doesn't change the field equation):

$$\begin{aligned}\mathcal{L}_\theta &= -\frac{\theta}{32\pi^2}\partial_\mu G^\mu,\\ G^\mu &= \epsilon^{\mu\nu\rho\sigma}\left(A_{\gamma\nu}F_{\gamma\rho\sigma} - \frac{1}{3}C_{\alpha\beta\gamma}A_{\alpha\nu}A_{\beta\rho}A_{\gamma\sigma}\right),\end{aligned} \tag{1.108}$$

where G^μ is the famous *Chern-Simons* class. At the same time, the integral of $\mathcal{L}_\theta$ over the entire spacetime volume is **topologically invariant** and satisfies:

$$\int d^4x\ \mathcal{L}_\theta = n\theta \quad (n = 0, \pm1, \pm2, \pm3, \cdots), \tag{1.109}$$

where n is called the winding number of the gluon field. The gluon field configurations with non-zero winding numbers are called *instantons* (discovered by Belavin, Polyakov, Schwarz, and Tyupkin [48]), the existence of which is crucial for solving another puzzle in particle physics – the $U(1)$ *problem* [49, 50, 51]. When computing the Feynman path integral:

$$\langle F[q,A]\rangle = \frac{\int \mathcal{D}\overline{q}\mathcal{D}q\mathcal{D}A\ F[q,A]\exp\left\{i\int d^4x\left(\mathcal{L}_{\text{QCD}} + \mathcal{L}_\theta\right)\right\}}{\int \mathcal{D}\overline{q}\mathcal{D}q\mathcal{D}A\ \exp\left\{i\int d^4x\left(\mathcal{L}_{\text{QCD}} + \mathcal{L}_\theta\right)\right\}}, \tag{1.110}$$

we need to integrate over all the gluon field configurations with different winding numbers n, therefore $\mathcal{L}_\theta$ would have non-trivial impact on the Feynman path integral if $\theta \neq 0$. In fact, it can be shown that [52], a shift in θ: $\theta \to \theta + \Delta\theta$ is equivalent to a transformation of the mass matrix M:

$$M \to \exp(-i\Delta\theta)M, \tag{1.111}$$

therefore a non-zero θ value is equivalent to a mass matrix M with complex phases. In other words, if we shift θ to be 0, we would no longer have the freedom to chose M to be real, thus the CP-symmetry would be violated in the strong interactions. However, the CP-violation has not been observed in strong interactions. More importantly, Crewther, Vecchia, Veneziano, and Witten [53] calculated the contribution of $\mathcal{L}_\theta$ to the neutron electric dipole moment (nEDM) d_n, and found that $d_n \sim 10^{-16}|\theta|e$ cm. The current best limit on d_n is $3.6 \times 10^{-26} e$ cm (95% C.L.) [54], which means $|\theta|$ needs to be smaller than $\sim 10^{-10}$. The reason why θ is so small is one of the main mysteries in particle physics, which is known as the **strong CP problem**. One popular solution to the strong CP problem is the suggestion that there exists a global chiral $U(1)$ symmetry which is spontaneously broken at some high energy scale [55, 56]. As discussed in Section 1.2.2, the spontaneous breaking of such symmetry will result in a (pseudo-)Goldstone boson – "axion" a [57, 58]. At the same time, this new chiral $U(1)$ symmetry will also be broken by the chiral anomaly when coupled with gluon fields, which can be described by an effective interaction between axion fields and gluon fields (similar to the case in $\pi^0 \to \gamma\gamma$):

$$\mathcal{L}_{\text{anomaly}} = -\frac{1}{64\pi^2}\frac{a}{f_a}\epsilon^{\mu\nu\rho\sigma}F_{\alpha\mu\nu}F_{\alpha\rho\sigma}, \tag{1.112}$$

where f_a corresponds to some unknown scale. Adding the $\mathcal{L}_\theta$ term, the total Lagrangian contains a term as:

$$\mathcal{L}_\theta + \mathcal{L}_{\text{anomaly}} = -\frac{1}{64\pi^2}\left(\theta + \frac{a}{f_a}\right)\epsilon^{\mu\nu\rho\sigma}F_{\alpha\mu\nu}F_{\alpha\rho\sigma}. \tag{1.113}$$

Now that the winding number of gluon field configuration can be any integer from $-\infty$ to $+\infty$, the effective potential of the axion a must be an even function of $\theta + a/f_a$. Since the vacuum state is at a stationary point of the effective potential, the vacuum

expectation value of the axion field can satisfy:

$$\theta + \frac{\langle a \rangle_0}{f_a} = 0, \tag{1.114}$$

at which the CP-violating term is shifted to zero, therefore the existence of the axion provides a dynamical solution to the strong CP problem. The search for axion remains one of the important topics in particle physics experiments.

Chapter 2

Beyond Standard Model Physics and Long-lived Particles

Many searches for new physics beyond the standard model (BSM) focus on short lifetimes or missing energy signatures, which leave a large phase space with long-lived particles that having macroscopic decay lengths uncovered. The lifetime of a given particle is determined by its decay rate Γ:

$$\tau_0^{-1} = \Gamma \sim \frac{1}{m} \int d\Pi_f \left| \mathcal{M}_{\text{decay}} \right|^2 , \tag{2.1}$$

where m is the mass of the particle, Π_f is the allowed final state phase space satisfying four-momentum conservation, and $\mathcal{M}_{\text{decay}}$ is the matrix element of the decay process. The particle tends to be long-lived when:

- the relevant couplings are small, such that $\mathcal{M}_{\text{decay}}$ is small;
- $\mathcal{M}_{\text{decay}}$ is suppressed by some large scale;
- the allowed final state phase space is small, e.g. with a nearly-degenerate mass spectrum.

The BSM physics cases for long-lived particles (LLPs) are extremely rich, in the following sections of this chapter, I will mainly discuss some supersymmetric (SUSY) models with long-lived particles. However, the strong theoretical motivation for the existence of LLPs is not limited to SUSY scenarios, and can also be relevant to other important topics such as dark matter candidates [59, 60, 61, 62, 63, 64], neutral naturalness [65, 66, 67, 68, 69], and right-handed neutrinos [70, 71, 72, 73], etc.

2.1 Long-lived supersymmetric models

2.1.1 Foundations of supersymmetric field theories

Until now, all the symmetry generators we encountered are bosonic and can not change the particle statistics, i.e. they can not turn bosons to fermions, or vice versa. However, theoretically it is possible to construct fermionic symmetry generators that satisfy both the quantum principles and the Lorentz invariance. To see this, consider the following Lorentz symmetry generators:

$$\mathbf{A} \equiv \frac{1}{2}(\mathbf{J} + i\mathbf{K}), \quad \mathbf{B} \equiv \frac{1}{2}(\mathbf{J} - i\mathbf{K}), \tag{2.2}$$

where $\mathbf{J}$ and $\mathbf{K}$ are the generators for rotations and boosts. $\mathbf{A}$ and $\mathbf{B}$ satisfy following commutation relations:

$$[A_i, A_j] = \epsilon_{ijk} A_k, \quad [B_i, B_j] = \epsilon_{ijk} B_k, \quad [A_i, B_j] = 0. \tag{2.3}$$

Therefore $\mathbf{A}$ and $\mathbf{B}$ can be viewed as two independent three-dimensional rotation groups, and any representation of the homogeneous Lorentz group can be classified by the spins of $\mathbf{A}$ and $\mathbf{B}$, which is called the (A, B) representation. For example, a $(0, 0)$ representation is a scalar, a $(0, \frac{1}{2})$ or $(\frac{1}{2}, 0)$ representation is a left-handed or right handed Weyl fermion, a $(0, \frac{1}{2}) \oplus (\frac{1}{2}, 0)$ representation is a Dirac fermion, and a $(\frac{1}{2}, \frac{1}{2})$ is

a vector, etc. The Haag-Lopuszanski-Sohnius theorem [74] states that any fermionic symmetry generator must belong to a $(0, \frac{1}{2})$ or $(\frac{1}{2}, 0)$ representation. Now given a set of fermionic symmetry generators $Q_{\alpha r}$ that belong to $(0, \frac{1}{2})$ representations (where a is the spinor index), their Hermitian adjoints $Q^\dagger_{\dot{\beta} s}$ must belong to $(\frac{1}{2}, 0)$ representations since $\mathbf{A}^\dagger = \mathbf{B}$, and they satisfy the following "supersymmetry algebra":

$$\{Q_{\alpha r}, Q^\dagger_{\dot{\beta} s}\} = -2\delta_{rs}\sigma^\mu_{\alpha\dot{\beta}} P_\mu, \quad \{Q_{\alpha r}, Q_{\beta s}\} = \epsilon_{\alpha\beta} Z_{rs}, \tag{2.4}$$

$$\sigma^1 = \begin{pmatrix} 0 & 1 \\ 1 & 0 \end{pmatrix}, \quad \sigma^2 = \begin{pmatrix} 0 & -i \\ i & 0 \end{pmatrix}, \quad \sigma^3 = \begin{pmatrix} 1 & 0 \\ 0 & -1 \end{pmatrix},$$

$$\sigma^0 = \begin{pmatrix} 1 & 0 \\ 0 & 1 \end{pmatrix}, \quad \epsilon = \begin{pmatrix} 0 & 1 \\ -1 & 0 \end{pmatrix}.$$

When Z_{rs} vanishes, the supersymmetry algebra reduces to the *simple supersymmetry algebra*:

$$\{Q_\alpha, Q^\dagger_{\dot{\beta}}\} = -2\sigma^\mu_{\alpha\dot{\beta}} P_\mu, \quad \{Q_\alpha, Q_\beta\} = 0. \tag{2.5}$$

To build supersymmetric theories, it is usually useful to introduce anticommuting c-numbers (which is also known as *Grassmann variables*) θ_a, in the sense that:

$$\{\theta_1, \theta_2\} = \{\theta_1, \theta_2^\dagger\} = \{\theta_1^\dagger, \theta_2^\dagger\} = 0. \tag{2.6}$$

Then the anticommutation rules for supersymmetry algebra can be written as commutation rules:

$$[\theta_1 Q, Q^\dagger \theta_2^\dagger] = -2\theta_1 \sigma^\mu \theta_2^\dagger P_\mu, \quad [\theta_1 Q, Q\theta_2] = 0, \tag{2.7}$$

therefore the SUSY algebra can be viewed as the Lie-algebra acting on the "superfields" S defined in the "superspace" with the usual four-dimensional coordinates (t, x, y, z) and the supercoordinates $(\theta, \theta^\dagger)$ [75, 76]:

$$S(x^\mu, \theta, \theta^\dagger). \tag{2.8}$$

Consider the following translation operator acting on S:

$$G(x^\mu, \theta, \theta^\dagger) \equiv \exp(-ix^\mu P_\mu + i\theta Q + i\theta^\dagger Q^\dagger) \tag{2.9}$$

$$= \exp(-ix^\mu P_\mu + i\theta^\alpha Q_\alpha + i\theta^\dagger_{\dot\alpha} Q^{\dagger\dot\alpha}). \tag{2.10}$$

Using $e^A e^B = e^{A+B+\frac{1}{2}[A,B]+\cdots}$, we can have:

$$G(0, \eta, \eta^\dagger) G(x^\mu, \theta, \theta^\dagger) = G(x^\mu - i\theta\sigma^\mu\eta^\dagger + i\eta\sigma^\mu\theta^\dagger, \theta + \eta, \theta^\dagger + \eta^\dagger), \tag{2.11}$$

for which $G(0, \eta, \eta^\dagger)$ induces a translation in the superspace:

$$(x^\mu, \theta, \theta^\dagger) \to (x^\mu - i\theta\sigma^\mu\eta^\dagger + i\eta\sigma^\mu\theta^\dagger, \theta + \eta, \theta^\dagger + \eta^\dagger), \tag{2.12}$$

so $Q(Q^\dagger)$ can be expressed as differential operators:

$$Q_\alpha = i\partial_{\theta^\alpha} - \sigma^\mu_{\alpha\dot\beta}\theta^{\dagger\dot\beta}\partial_\mu, \quad Q^\dagger_{\dot\alpha} = -i\partial_{\theta^{\dagger\dot\alpha}} + \theta^\beta\sigma^\mu_{\beta\dot\alpha}\partial_\mu. \tag{2.13}$$

Direct calculation yields:

$$\{Q_\alpha, Q^\dagger_{\dot\beta}\} = 2i\sigma^\mu_{\alpha\dot\beta}\partial_\mu, \quad \{Q_\alpha, Q_\beta\} = 0, \tag{2.14}$$

which is the same as the simple SUSY algebra given that $P_\mu = -i\partial_\mu$. An infinitesimal supersymmetric transformation can be written as:

$$\delta_\theta S = -i\left((\delta\theta)Q + (\delta\theta^\dagger)Q^\dagger\right) S. \tag{2.15}$$

We can also construct chiral covariant derivatives with respect to θ and $\theta^\dagger$ such that they commutate with supersymmetric transformations:

$$D_\alpha = \partial_{\theta^\alpha} - i(\sigma^\mu\theta^\dagger)_\alpha\partial_\mu, \quad \overline{D}_{\dot\alpha} = -\partial_{\theta^{\dagger\dot\alpha}} + i(\theta\sigma^\mu)_{\dot\alpha}\partial_\mu. \tag{2.16}$$

$$\delta_\theta\left(D_\alpha S\right) = D_\alpha\left(\delta_\theta S\right), \quad \delta_\theta\left(\overline{D}_{\dot\alpha} S\right) = \overline{D}_{\dot\alpha}\left(\delta_\theta S\right). \tag{2.17}$$

D_α and $\overline{D}_{\dot\alpha}$ satisfy the following anticommutation relations:

$$\{D_\alpha, \overline{D}_{\dot\beta}\} = -2i\sigma^\mu_{\alpha\dot\beta}\partial_\mu, \quad \{D_\alpha, D_\beta\} = \{\overline{D}_{\dot\alpha}, \overline{D}_{\dot\beta}\} = 0. \tag{2.18}$$

Now we can define (left-)chiral superfields Φ whose chiral covariant derivatives with respect to $\theta^\dagger$ vanish:

$$\overline{D}_{\dot{\alpha}}\Phi = 0. \tag{2.19}$$

If we define $y^\mu \equiv x^\mu - i\theta\sigma^\mu\theta^\dagger$, we can write D_α and $\overline{D}_{\dot{\alpha}}$ in terms of the new coordinates $(y^\mu, \theta, \theta^\dagger)$:

$$D_\alpha = \frac{\partial}{\partial\theta^\alpha} - 2i(\sigma^\mu\theta^\dagger)_\alpha\frac{\partial}{\partial y^\mu}, \quad \overline{D}_{\dot{\alpha}} = -\frac{\partial}{\partial\theta^{\dagger\dot{\alpha}}}. \tag{2.20}$$

Then the general solution to $\overline{D}_{\dot{\alpha}}\Phi = 0$ can be written as:

$$\Phi = \phi(y) + \sqrt{2}\theta\psi(y) + \theta\theta F(y). \tag{2.21}$$

The supersymmetric transformations of Φ can be determined by evaluating $\delta_\theta\Phi$ based on equation 2.15. Or more simply, we evaluate the transformation induced by the translation 2.12, when written in the $(y, \theta, \theta^\dagger)$ coordinates, it is equivalent to:

$$(y^\mu, \theta, \theta^\dagger) \to (y^\mu - 2i\theta\sigma^\mu(\delta\theta^\dagger), \theta + \delta\theta, \theta^\dagger + \delta\theta^\dagger), \tag{2.22}$$

the supersymmetric transformations of Φ are thus straightforwardly determined as:

$$\delta_\theta\phi = \sqrt{2}(\delta\theta)\psi, \tag{2.23}$$

$$\delta_\theta\psi = -\sqrt{2}i\sigma^\mu(\delta\theta^\dagger)\partial_\mu\phi + \sqrt{2}(\delta\theta)F, \tag{2.24}$$

$$\delta_\theta F = -\sqrt{2}i\sigma^\mu(\delta\theta^\dagger)\partial_\mu\psi = -\sqrt{2}i(\delta\theta^\dagger)\overline{\sigma}^\mu\partial_\mu\psi, \tag{2.25}$$

where $\overline{\sigma}^\mu$ are defined as:

$$\begin{aligned}(\overline{\sigma}^0)^{\dot{\alpha}\beta} &= (\sigma^0)_{\alpha\dot{\beta}}, \quad (\overline{\sigma}^1)^{\dot{\alpha}\beta} = -(\sigma^1)_{\alpha\dot{\beta}}, \\ (\overline{\sigma}^2)^{\dot{\alpha}\beta} &= -(\sigma^2)_{\alpha\dot{\beta}}, \quad (\overline{\sigma}^3)^{\dot{\alpha}\beta} = -(\sigma^3)_{\alpha\dot{\beta}}.\end{aligned} \tag{2.26}$$

Therefore the supersymmetric transformation of F is a total derivative according to equation 2.25, this means if we treat F (which is called the ***F*-term**) as a Lagrangian,

the action $\int d^4x\ F$ will be invariant under supersymmetric transformations. Furthermore, it is easy to verify that any products $\Phi_i\Phi_j\dots$ of chiral superfields Φ_i are also chiral superfields, i.e. $\overline{D}_{\dot\alpha}(\Phi_i\Phi_j\dots) = 0$, so we can build a general form of chiral superfields:

$$W(\Phi_i) = L_i\Phi_i + \frac{1}{2}m_{ij}\Phi_i\Phi_j + \frac{1}{3}Y_{ijk}\Phi_i\Phi_j\Phi_k\ . \tag{2.27}$$

$W(\Phi_i)$ is called the **superpotential**, its F-term produces a supersymmetrically invariant Lagrangian (up to a total derivative) containing mass terms and Yukawa couplings:

$$\begin{aligned}\mathcal{L}_{\text{int}} &\equiv W(\Phi_i)|_F + \text{h.c.} = \int d\theta^\dagger d\theta^\dagger\ W(\Phi_i) + \text{h.c.}\\ &= L_iF_i + m_{ij}\left(\phi_iF_j - \frac{1}{2}\psi_i\psi_j\right) + Y_{ijk}\left(\phi_i\phi_jF_k - \psi_i\psi_j\phi_k\right) + \text{h.c.}\ .\end{aligned} \tag{2.28}$$

At the same time, for any superfield S, the integral of its $\theta\theta\theta^\dagger\theta^\dagger$ component (known as the ***D*-term**) over the space-time is always SUSY-invariant:

$$\delta_\theta\left(\int dx^4\ \ (S|_D)\right) = \delta_\theta\left(\int dx^4 d\theta d\theta d\theta^\dagger d\theta^\dagger\ S\right) = \int dx^4 d\theta d\theta d\theta^\dagger d\theta^\dagger\ \delta_\theta S = 0, \tag{2.29}$$

which is due to the fact that the SUSY generators Q_α and $Q^\dagger_{\dot\alpha}$ are composed of differential operators ∂_{θ^α}, $\partial_{\theta^{\dagger\dot\alpha}}$, and ∂_μ. Therefore we can build another SUSY-invariant Lagrangian as the D-term of $\Phi_i^*\Phi_i$, which contains the kinematic terms of the scalar fields ϕ_i and their superpartners — fermion fields ψ_i:

$$\begin{aligned}\mathcal{L}_{\text{kine}} &\equiv [\Phi_i^*\Phi_i]|_D = \int d\theta d\theta d\theta^\dagger d\theta^\dagger \Phi_i^*\Phi_i\\ &= -\partial^\mu\phi_i^*\partial_\mu\phi_i + i\psi_i^\dagger\overline{\sigma}^\mu\partial_\mu\psi_i + F_i^*F_i.\end{aligned} \tag{2.30}$$

Then the total SUSY Lagrangian built from chiral superfields are:

$$\begin{aligned}\mathcal{L} =& \mathcal{L}_{\text{kine}} + \mathcal{L}_{\text{int}}\\ =& -\partial^\mu\phi_i^*\partial_\mu\phi_i + i\psi_i^\dagger\overline{\sigma}^\mu\partial_\mu\psi_i + F_i^*F_i\\ &+ L_iF_i + m_{ij}\left(\phi_iF_j - \frac{1}{2}\psi_i\psi_j\right) + Y_{ijk}\left(\phi_i\phi_jF_k - \psi_i\psi_j\phi_k\right) + \text{h.c.}\ .\end{aligned} \tag{2.31}$$

Notice that there is no kinematic term for fields F_i, in which case F_i are called *auxiliary fields* and do not correspond to physical particles. Solving the Euler-Lagrangian equations for F_i yields:

$$F_i + L_i^* + m_{ij}^* \phi_j^* + Y_{jki}^* \phi_j^* \phi_k^* = 0. \tag{2.32}$$

Inserting equation 2.32 back to $\mathcal{L}$, we have:

$$\begin{aligned}\mathcal{L} = &- \partial^\mu \phi_i^* \partial_\mu \phi_i + i\psi_i^\dagger \overline{\sigma}^\mu \partial_\mu \psi_i \\ &- \frac{1}{2} m_{ij} \psi_i \psi_j - \frac{1}{2} m_{ij}^* \psi_i^\dagger \psi_j^\dagger - Y_{ijk} \psi_i \psi_j \phi_k - Y_{ijk}^* \psi_i^\dagger \psi_j^\dagger \phi_k^* \\ &- \left| L_i + m_{ij} \phi_j + Y_{jki} \phi_j \phi_k \right|^2 .\end{aligned} \tag{2.33}$$

Now we have a Lagrangian for ϕ_i and ψ_i, including their kinetic terms, mass terms, and Yukawa couplings, as well as a potential for ϕ_i: $F_i^* F_i = \left| L_i + m_{ij} \phi_j + Y_{jki} \phi_j \phi_k \right|^2$, which will be crucial for the spontaneous breaking of supersymmetry.

As the next step, in order to introduce gauge interactions to SUSY theories, we can introduce a real superfield V, in the sense that $V^* = V$:

$$\begin{aligned}V(x, \theta, \theta^\dagger) = &C + \theta\omega + \theta^\dagger \omega^\dagger + \theta\theta b + \theta^\dagger \theta^\dagger b^* + \theta^\dagger \overline{\sigma}^\mu \theta A_\mu + \theta^\dagger \theta^\dagger \theta \left(\lambda - \frac{i}{2} \sigma^\mu \partial_\mu \omega^\dagger \right) \\ &+ \theta\theta\theta^\dagger \left(\lambda^\dagger - \frac{i}{2} \overline{\sigma}^\mu \partial_\mu \omega \right) + \theta\theta\theta^\dagger\theta^\dagger \left(\frac{1}{2} D + \frac{1}{4} \partial_\mu \partial^\mu C \right) .\end{aligned} \tag{2.34}$$

Consider the following (Abelian) "supergauge transformation" induced by a chiral superfield $\Lambda = \phi_\Lambda(x) + \sqrt{2}\theta\psi_\Lambda(x) + \theta\theta F_\Lambda(x) + \ldots$:

$$V \to V + i(\Lambda^* - \Lambda). \tag{2.35}$$

The different components of V transforms like:

$$C \to C + i(\phi_\Lambda^*), \tag{2.36}$$

$$\omega_\alpha \to \omega_\alpha - i\sqrt{2}\psi_{\Lambda\alpha}, \tag{2.37}$$

$$b \to b - iF_\Lambda, \tag{2.38}$$

$$A_\mu \to A_\mu + \partial_\mu(\phi_\Lambda + \phi_\Lambda^*), \tag{2.39}$$

$$\lambda \to \lambda, \tag{2.40}$$

$$D \to D, \tag{2.41}$$

where the transformation of A_μ is the same as the ordinary Abelian gauge transformation. With the supergauge transformation, we have the freedom to fix C, ω, and b to be zero while the transformation of A_μ is unaltered. This condition is called the **Wess-Zumino gauge**, under which the vector superfield V can be written as:

$$V = \theta^\dagger\overline{\sigma}^\mu\theta A_\mu + \theta^\dagger\theta^\dagger\theta\lambda + \theta\theta\theta^\dagger\lambda^\dagger + \frac{1}{2}\theta\theta\theta^\dagger\theta^\dagger D. \tag{2.42}$$

From V we can build a chiral superfield:

$$\mathcal{W}_\alpha = -\frac{1}{4}\overline{D}_{\dot\beta}\overline{D}^{\dot\beta}D_\alpha V, \tag{2.43}$$

where $\mathcal{W}_\alpha$ is supergauge-invariant:

$$\begin{aligned}\mathcal{W}_\alpha \to -\frac{1}{4}\overline{D}_{\dot\beta}\overline{D}^{\dot\beta}D_\alpha\left[V + i(\Lambda^* - \Lambda)\right] &= \mathcal{W}_\alpha + \frac{i}{4}\overline{D}_{\dot\beta}\overline{D}^{\dot\beta}D_\alpha\Lambda \\ &= \mathcal{W}_\alpha - \frac{i}{4}\overline{D}^{\dot\beta}\{\overline{D}_{\dot\beta}, D_\alpha\}\Lambda \\ &= \mathcal{W}_\alpha + \frac{1}{2}\sigma^\mu_{\alpha\dot\beta}\overline{D}^{\dot\beta}\partial_\mu\Lambda \\ &= \mathcal{W}_\alpha. \end{aligned} \tag{2.44}$$

Therefore the F-term of $\mathcal{W}^\alpha\mathcal{W}_\alpha$ is both SUSY-invariant and supergauge-invariant. Taking the Wess-Zumino gauge, it is:

$$[\mathcal{W}^\alpha\mathcal{W}_\alpha]|_F = D^2 + 2i\lambda\sigma^\mu\partial_\mu\lambda^\dagger - \frac{1}{2}F^{\mu\nu}F_{\mu\nu} + \frac{i}{4}\epsilon^{\mu\nu\rho\sigma}F_{\mu\nu}F_{\rho\sigma}, \tag{2.45}$$

where $F_{\mu\nu}$ is the field strength tensor: $F_{\mu\nu} = \partial_\mu A_\nu - \partial_\nu A_\mu$. We can then write down a pure gauge action:

$$\begin{aligned}\int d^4x\ \mathcal{L}_{\text{gauge}} &= \int d^4x\ \left(\frac{1}{4}[\mathcal{W}^\alpha \mathcal{W}_\alpha]|_F + \frac{1}{4}[\mathcal{W}^\dagger_{\dot\alpha}\mathcal{W}^{\dagger\dot\alpha}]|_F\right) \\ &= \int d^4x\ \left(\frac{1}{2}D^2 + i\lambda^\dagger\overline{\sigma}^\mu\partial_\mu\lambda - \frac{1}{4}F^{\mu\nu}F_{\mu\nu}\right). \end{aligned} \tag{2.46}$$

The fermion field λ can be viewed as the superpartner of the gauge field A_μ — *gaugino*. To consider the gauge transformations for matter fields, consider the following supergauge transformations on Φ_i:

$$\Phi_i \to e^{2ig\Lambda}\Phi_i, \tag{2.47}$$

where g is the gauge coupling constant. The superfields product $\Phi_i^*\Phi_i$ (which determines the kinetic terms of matter fields) transforms like:

$$\Phi_i^*\Phi_i \to \Phi_i^* e^{2ig(\Lambda-\Lambda^*)}\Phi_i. \tag{2.48}$$

Now in order to make our theory supergauge invariant, we need to cancel $e^{2ig(\Lambda-\Lambda^*)}$ in equation 2.54, for which we can replace $\Phi_i^*\Phi_i$ with $\Phi_i^* e^{2gV}\Phi_i$. So the kinetic terms of matter fields in equation 2.30 become:

$$\mathcal{L}_{\text{kine}} \equiv [\Phi_i^* e^{2gV}\Phi_i]|_D. \tag{2.49}$$

taking the Wess-Zumino gauge and using the identity $\theta^\dagger\overline{\sigma}^\mu\theta\theta^\dagger\overline{\sigma}^\nu\theta = -\frac{1}{2}\theta^\dagger\theta^\dagger\theta\theta\eta^{\mu\nu}$, we have:

$$\begin{aligned}[\Phi_i^* e^{2gV}\Phi_i]|_D = &- |D_\mu\phi_i|^2 + i\psi_i^\dagger\overline{\sigma}^\mu D_\mu\psi_i + F_i^* F_i \\ &- \sqrt{2}g(\phi_i^*\psi_i\lambda + \lambda^\dagger\psi_i^\dagger\phi_i) + g\phi_i^*\phi_i D, \end{aligned} \tag{2.50}$$

where $D_\mu = \partial_\mu - igA_\mu$. Therefore we get the gauge interactions for ϕ and ψ, as well as a new three-point interaction between ϕ, ψ, and the gaugino λ. Add the terms in

equations 2.46 and 2.50, we have a SUSY theory with Abelian gauge symmetry:

$$\begin{aligned}\mathcal{L} = &-\frac{1}{4}F^{\mu\nu}F_{\mu\nu} + i\lambda^\dagger\overline{\sigma}^\mu\partial_\mu\lambda - |D_\mu\phi_i|^2 + i\psi_i^\dagger\overline{\sigma}^\mu D_\mu\psi_i + F_i^*F_i \\ &- \sqrt{2}g(\phi_i^*\psi_i\lambda + \lambda^\dagger\psi_i^\dagger\phi_i) + g\phi_i^*\phi_i D + \frac{1}{2}D^2,\end{aligned} \tag{2.51}$$

which doesn't contain kinetic terms for the field D, thus D is also an auxiliary field. Solving the field equation for D and inserting it back to the Lagrangian will yield another potential for ϕ: $\frac{1}{2}D^2 = \frac{1}{2}g^2(\phi_i^*\phi_i)^2$.

To extend the supergauge field theory to the non-Abelian case, with a set of gauge group generators t_a we can introduce a set of vector superfields V_a as well as a set of chiral superfields Λ_a, and define:

$$\mathbf{V} = \sum_a V_a t_a, \quad \mathbf{\Lambda} = \sum_a \Lambda_a t_a. \tag{2.52}$$

Then the supergauge transformations in equations 2.35 and 2.47 can be generalized to:

$$e^{\mathbf{V}} \to e^{i\mathbf{\Lambda}^\dagger}e^{\mathbf{V}}e^{-i\mathbf{\Lambda}}, \quad \Phi \to e^{2ig\mathbf{\Lambda}}\Phi, \tag{2.53}$$

so the term $\Phi^\dagger e^{2ig\mathbf{V}}\Phi$ is supergauge-invariant, its D-term yields:

$$\begin{aligned}[\Phi^\dagger e^{2ig\mathbf{V}}\Phi]|_D = &-|D_\mu\phi|^2 + i\psi^\dagger\overline{\sigma}^\mu D_\mu\psi + F^\dagger F \\ &+ g\sum_a\left(\sqrt{2}\phi^\dagger t_a\psi\lambda^a + \sqrt{2}\lambda^{a\dagger}\psi^\dagger t_a\phi + \phi^\dagger t_a\phi D^a\right)\end{aligned} \tag{2.54}$$

with $D_\mu = \partial_\mu - ig\sum_a A_\mu^a t_a$. Therefore we get the non-Abelian gauge interactions for the matter fields. In order to find out the pure gauge Lagrangian, we can generalize the $\mathcal{W}_\alpha$ defined in equation 2.43 to:

$$\mathbf{W}_\alpha = \frac{1}{4}\overline{D}_{\dot\beta}\overline{D}^{\dot\beta}e^{-\mathbf{V}}D_\alpha e^{\mathbf{V}}. \tag{2.55}$$

Since $\mathbf{\Lambda}$ is a chiral superfield: $\overline{D}_{\dot{\alpha}}\mathbf{\Lambda} = D_\alpha \mathbf{\Lambda}^\dagger = 0$, the supergauge transformation of $\mathbf{W}_\alpha$ can be determined as:

$$\mathbf{W}_\alpha \to e^{i\mathbf{\Lambda}}\mathbf{W}_\alpha e^{-i\mathbf{\Lambda}}, \tag{2.56}$$

thus $\mathrm{Tr}[\mathbf{W}^\alpha \mathbf{W}_\alpha]$ is supergauge-invariant. Under Wess-Zumino gauge, its F-term is:

$$\mathrm{Tr}[\mathbf{W}^\alpha \mathbf{W}_\alpha]|_F = 4C_2 g^2 \sum_a \left(D^a D^a + 2i\lambda^a \sigma^\mu D_\mu \lambda^{\dagger a} - \frac{1}{2} F^{a\mu\nu} F^a_{\mu\nu} + \frac{i}{4}\epsilon^{\mu\nu\rho\sigma} F^a_{\mu\nu} F^a_{\rho\sigma} \right), \tag{2.57}$$

where C_2 is determined by $\mathrm{Tr}[t_a t_b] = C_2 \delta_{ab}$, and is usually normalized to be $\frac{1}{2}$. Gauginos λ^a furnish an adjoint representation of the gauge group, thus the covariant derivative for λ^a is $D_\mu \lambda^a = \partial_\mu \lambda^a + gC^{abc} A^b_\mu \lambda^c$. We can then write down a pure gauge Lagrangian that is both SUSY-invariant and supergauge-invariant:

$$\mathcal{L}_{\text{gauge}} = \frac{1}{4C_2 g^2} \left(\frac{1}{4} - i\frac{\Theta}{32\pi^2} \right) \mathrm{Tr}[\mathbf{W}^\alpha \mathbf{W}_\alpha]|_F + \text{h.c.}, \tag{2.58}$$

where Θ corresponds to the θ-term $\mathcal{L}_\theta$ we encountered in section 1.5, which violates CP-symmetry.

In summary, we can now write down the most general renormalizable Lagrangian for supergauge field theories, which is the sum of terms in equations 2.58, 2.54, and 2.28:

$$\begin{aligned} \mathcal{L}_{\text{SUSY}} =& \frac{1}{4C_2 g^2} \left(\frac{1}{4} - i\frac{\Theta}{32\pi^2} \right) \mathrm{Tr}[\mathbf{W}^\alpha \mathbf{W}_\alpha]|_F + \text{h.c.} + [\Phi^\dagger e^{2ig\mathbf{V}} \Phi]|_D \\ &+ W(\Phi_i)|_F + \text{h.c.} \ . \end{aligned} \tag{2.59}$$

2.1.2 *R*-parity violating supersymmetry

In order to consider the simplest supersymmetric extension of the $SU(3)_c \times SU(2)_L \times U(1)_Y$ theory of the standard model, we can promote the standard model matter fields to (left-)chiral superfields (as defined in equation 2.21) which consist of the SM particles and their superpartners, and use the following conventions:

- Q_i: the chiral superfields corresponding to the left-handed $SU(2)_L$ quark doublets $\begin{pmatrix} u_{Li} \\ d_{Li} \end{pmatrix}$;
- $\overline{U}_i$: the chiral superfields corresponding to the Hermitian conjugates of the right-handed up-type quarks $u^\dagger_{Ri}$;
- $\overline{D}_i$: the chiral superfields corresponding to the Hermitian conjugates of the right-handed down-type quarks $d^\dagger_{Ri}$;
- L_i: the chiral superfields corresponding to the left-handed $SU(2)_L$ lepton doublets $\begin{pmatrix} \nu_i \\ e_{Li} \end{pmatrix}$;
- $\overline{E}_i$: the chiral superfields corresponding to the Hermitian conjugates of the right-handed charged leptons $e^\dagger_{Ri}$.

We can also introduce two Higgs chiral superfields H_u and H_d to generate masses for quarks and leptons through spontaneous symmetry breaking. Then we can write down the superpotential for the so-called **Minimal Supersymmetric Standard Model (MSSM)**:

$$W_{\text{MSSM}} = \mathbf{Y_U}\overline{U}QH_u + \mathbf{Y_D}\overline{D}QH_d + \mathbf{Y_E}\overline{E}LH_d + \mu H_u H_d, \tag{2.60}$$

where the product of two $SU(2)_L$ doublets like $H_u H_d$ should be viewed as a contraction with the antisymmetric Levi-Civita symbol ϵ, i.e. $H_u H_d = \epsilon^{ab}(H_u)_a(H_d)_b$ with a and b as $SU(2)_L$ indices, such that the product is a $SU(2)_L$ singlet. The superpotential W_{MSSM} conserves baryon number and lepton number, however we can also build another superpotential that is $SU(3)_c \times SU(2)_L \times U(1)_Y$ invariant [77]:

$$W_{\text{RPV}} = \mu'_i L_i H_u + \frac{1}{2}\lambda_{ijk} L_i L_j \overline{E}_k + \lambda'_{ijk} L_i Q_j \overline{D}_k + \frac{1}{2}\lambda''_{ijk}\overline{U}_i\overline{D}_j\overline{D}_k. \tag{2.61}$$

Notice that the product $L_i L_j$ contain contractions with ϵ^{ab} due to the requirement on the $SU(2)_L$ gauge symmetry, thus we must have $\lambda_{ijk} = -\lambda_{jik}$. Similarly, $\overline{U}_i \overline{D}_j \overline{D}_k$ contains a contraction with $\epsilon^{\alpha\beta\gamma}$ (where α, β, and γ run over the color indices) due to the the requirement on the $SU(3)_c$ gauge symmetry, thus we also must have $\lambda''_{ijk} = -\lambda''_{ikj}$. The couplings λ_{ijk}, λ'_{ijk}, and μ'_i violate lepton number conservation, while the coupling λ''_{ijk} violates baryon number conservation. Lepton number violating or baryon number violating processes usually face stringent bounds from experimental measurements. For example, non-zero λ' and λ'' can induce a non-zero proton decay rate:

$$\Gamma(p \to e^+ \pi^0) \sim m_p^5 \sum_{i=2,3} \frac{|\lambda'_{11i} \lambda''_{11i}|^2}{m_{\tilde{d}_i}{}^4}, \tag{2.62}$$

while the current best limits on the $\Gamma(p \to e^+ \pi^0)$ is around $10^{-40} s^{-1}$. Therefore a specific symmetry — R-parity was usually imposed to prohibit the terms in W_{RPV}.

To introduce the concept of R-parity, first of all, it can be noticed that the SUSY algebra 2.5 has a global $U(1)$ symmetry — R-symmetry [78]:

$$Q \to e^{-i\alpha} Q, \quad Q^\dagger \to e^{i\alpha} Q^\dagger. \tag{2.63}$$

Or equivalently:

$$\theta \to e^{i\alpha} \theta, \quad \theta^\dagger \to e^{-i\alpha} \theta^\dagger. \tag{2.64}$$

However, if R-symmetry is unbroken, the mass terms of gauginos are generally prohibited, in which case gauginos should have already been discovered. Therefore, it is commonly assumed that the continuous $U(1)$ R-symmetry is broken to a discrete Z_2 subgroup — ***R*-parity** [79], defined as:

$$\theta \to -\theta, \quad \theta^\dagger \to -\theta^\dagger, \quad M \to -M, \quad V \to V, \quad H \to H, \tag{2.65}$$

where M represents matter chiral superfields — Q_i, $\overline{U}_i$, $\overline{D}_i$, L_i, and $\overline{E}_i$; V represents the gauge real superfields; H represents the Higgs chiral superfields — H_u and H_d. Since the matter superfields transform like $M \to -M$ and the terms in superpotential W_{RPV} contain odd number of matter superfields, W_{RPV} is forbidden if R-parity conservation is imposed.

When writing these superfields in their components, it follows immediately that all the SM particles carry R-parity of $+1$ while all their superpartners carry R-parity of -1. Furthermore, R-parity can be written equivalently in terms of baryon number B, lepton number L, and spin S:

$$P_R = (-1)^{3(\mathrm{B}-\mathrm{L})+2\mathrm{S}}. \tag{2.66}$$

R-parity conservation, if holds, has important consequences for collider signatures. It means that the lightest supersymmetric particle (LSP) can not decay to SM particles and thus is stable. The stable LSP will escape the detector and produce missing transverse energy (MET) signatures. Therefore, many SUSY searches at the Large Hadron Collider assume R-parity conservation and usually rely on the existence of MET signatures.

However, R-parity conservation is not guaranteed, the experimental constraints on proton decay and other B-violating/L-violating processes can be evaded by assuming the R-parity violating (RPV) couplings are small. When the RPV terms in W_{RPV} are allowed, squarks/sleptons can decay back to SM particles through λ, λ', or λ'' without producing (intrinsic) MET signatures, as illustrated in Figure 2.1. At the same time, since the RPV couplings are required to be small, the LSP is usually long-lived, and if it decays hadronically via λ' or λ'' couplings, **displaced jets** signatures will emerge.

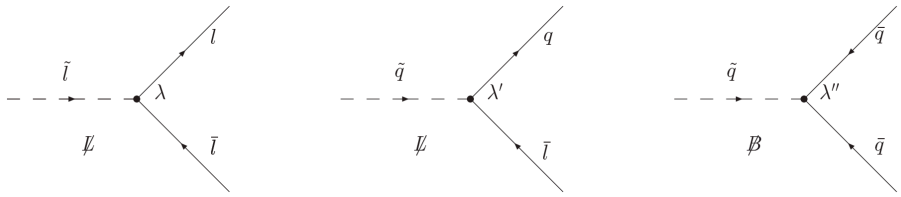

Figure 2.1: The allowed sleptons/squarks decays via non-zero RPV couplings λ, λ', and λ'', which violate lepton number conservation or baryon number conservation.

Besides the renormalizable, holomorphic superpotential W_{RPV}, RPV interactions can also be produced in the so-called "dynamical R-parity violation" (dRPV) framework [80], where the following nonrenormalizable, nonholomorphic Kähler potential are considered:

$$K_{\mathrm{dRPV}} = \frac{1}{M}\left(\eta_{ijk}\overline{U}_i\overline{E}_j\overline{D}_k^* + \eta'_{ijk}Q_i\overline{U}_iL_k^* + \eta''_{ijk}Q_iQ_j\overline{D}_k^*\right), \tag{2.67}$$

which is suppressed by the large scale M and naturally leads to small RPV couplings. The dRPV interactions can also result in a long-lived LSP with displaced decays [81]. For example, when a top squark LSP mainly decays to two bottom quarks ($\widetilde{\mathrm{t}} \to \overline{\mathrm{bb}}$) through η''_{333} coupling, its lifetime is:

$$c\tau_0 \sim 1\ \mathrm{mm}\left(\frac{300\ \mathrm{GeV}}{m_{\widetilde{\mathrm{t}}}}\right)\left(\frac{M}{10^8\ \mathrm{GeV}}\right)^2\left|\frac{1}{\eta''_{333}}\right|^2. \tag{2.68}$$

Therefore if the long lived top squarks are pair-produced, their decays will give rise to four displaced b jets, and each pair of them originates from a displaced vertex.

2.1.3 Gauge mediated supersymmetry breaking

If supersymmetry is unbroken, particles belonging to the same supermultiplet should have the same mass, and the superpartners of the SM particles should have already been discovered. Therefore supersymmetry must be spontaneously broken, and it

can be shown that the spontaneous breaking of supersymmetry is equivalent to the positive energy of the vacuum state. As discussed in Section 2.1.1, in SUSY theories, we indeed have a scalar potential for ϕ_i:

$$V(\phi_i) = F_i F_i + \frac{1}{2} D^a D^a = \left| L_i + m_{ij}\phi_j + Y_{jki}\phi_j\phi_k \right|^2 + \frac{1}{2} g_a^2 (\phi_i^* t_a \phi_i)^2, \tag{2.69}$$

so the SUSY-breaking corresponds to non-zero vacuum expectation values (VEV) of F_i or D^a, which are called F-term breaking [82] and D-term breaking [83]. When the SUSY-breaking happens, the mass matrix of the fermion particles (ψ_i, λ^a) in a given SUSY theory can be written as:

$$\begin{pmatrix} m_{ij} + 2Y_{ijk}\langle\phi_k\rangle_0 & \sqrt{2} g_a \left[\langle\phi^*\rangle_0 t^a\right]_i \\ \sqrt{2} g_b \left[\langle\phi^*\rangle_0 t^b\right]_j & 0 \end{pmatrix}, \tag{2.70}$$

which has an eigenvector with zero eigenvalue when the VEVs of F_i or D^a are non-zero :

$$\tilde{\Pi} = \frac{1}{\langle F\rangle_0} \begin{pmatrix} \langle F_i\rangle_0 \\ \frac{1}{\sqrt{2}}\langle D^a\rangle_0 \end{pmatrix}, \tag{2.71}$$

where $\langle F\rangle_0$ is a normalization factor, defined as:

$$\langle F\rangle_0 = \sqrt{\sum_i \langle F_i\rangle_0^2 + 1/2 \sum_a \langle D^a\rangle_0^2}. \tag{2.72}$$

This massless fermion field $\tilde{\Pi}$ is known as the *goldstino* [83], which can be viewed as the SUSY version of a Goldstone boson. The goldstino field can be described by the following effective Lagrangian [83] based on the requirement on the supercurrent conservation:

$$\begin{aligned} \mathcal{L}_{\text{goldstino}} &= i\tilde{\Pi}^\dagger \overline{\sigma}^\mu \partial_\mu \tilde{\Pi} - \frac{1}{\langle F\rangle_0}\left(\tilde{\Pi}\partial_\mu j^\mu + \text{h.c.}\right), \\ j^\mu &= \left(\sigma^\nu \overline{\sigma}^\mu \psi_i\right)\partial_\nu \phi_i^* - \frac{1}{2\sqrt{2}} \sigma^\nu \overline{\sigma}^\rho \sigma^\mu \lambda^{\dagger a} F^a_{\nu\rho} + \cdots, \end{aligned} \tag{2.73}$$

which induces goldstino-fermion-scalar and goldstino-gaugino-gauge boson interactions. Note that these interactions are suppressed by $\langle F \rangle_0$, which characterizes the SUSY-breaking scale.

At very large scale (i.e. Plank scale $\Lambda_P \sim 10^{19}$ GeV), gravitational interaction needs to be taken account of, where the graviton has a superpartner — *gravitino* $\widetilde{\mathrm{G}}$. Similar to the case in the Higgs mechanism, the degrees-of-freedom corresponding to the goldstino are "eaten" by the gravitino through the "super-Higgs" mechanism [84, 85], making the gravitino become a massive spin-$\frac{3}{2}$ fermion field. The mass of the gravitino can be estimated as:

$$m_{3/2} \sim \frac{\langle F \rangle_0}{\Lambda_P}. \tag{2.74}$$

At low energy, the only relevant parts of the gravitino are those degrees-of-freedom provided by the eaten goldstino (since the gravitational interaction is very weak), thus the low-energy interactions of the gravitino can also be described by $\mathcal{L}_{\text{goldstino}}$ in equation 2.73, leads to gravitino-fermion-scalar and gravitino-gaugino-gauge boson interaction vertices suppressed by $\langle F \rangle_0$, as illustrated in Figure 2.2.

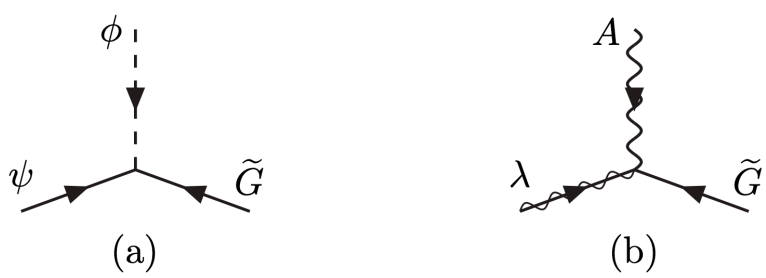

Figure 2.2: The interactions of gravitino with scalar-fermion or gaugino-gauge boson through derivative couplings suppressed by the SUSY-breaking scale.

Now let's consider the so-called "gauge mediated supersymmetry breaking" (GMSB) framework [86]. GMSB has a great advantage that it can avoid dangerous FCNC

processes which contradict stringent experimental limits in flavor physics. It assumes the existence of a hidden sector consisting of some new chiral superfields — *messager superfields*, as well as some other superfields with non-vanishing VEVs such that they are responsible for the SUSY-breaking in the hidden sector. The messager superfields also carry $SU(3)_c \times SU(2)_L \times U(1)_Y$ gauge charges, so the SUSY-breaking in the hidden sector can be communicated by the messager superfields to the observed sector (i.e. MSSM superfields) through gauge interactions. One important aspect of the GMSB is that the SUSY-breaking scale of the hidden sector ($\sim \sqrt{\langle F \rangle_0}$) is usually much smaller than the Planck scale Λ_P, thus the mass of the gravitino is very small and can be treated as the LSP. In such case, the next-to-lightest supersymmetric particle (NLSP) can decay to its SM superpartner and a gravitino through the interactions shown in Figure 2.2. As discussed above, this decay is suppressed by $\langle F \rangle_0$, therefore the NLSP is usually long-lived and can produce displaced signatures in collider detectors.

In the traditional forms of GMSB, the NLSP is usually a bino-like neutralino or a tau slepton, which can lead to displaced photon or displaced tau signatures at the LHC. However, in a more general framework of GMSB — "general gauge mediation" [87], the NLSP could be any superparticles, leading to rich LHC phenomenologies with long-lived signatures. When the mass of its SM superpartner is small, the lifetime of the NLSP can be estimated as:

$$c\tau_0 \sim 0.3 \text{ mm} \left(\frac{100 \text{ GeV}}{m_{\text{NLSP}}}\right)^5 \left(\frac{\sqrt{\langle F \rangle_0}}{100 \text{ TeV}}\right)^4 . \tag{2.75}$$

If the NLSP is gluino or a squark, its decay will also give rise to a displaced jet signature, which falls in the class of targets of this thesis.

2.1.4 Split supersymmetry

Though one of the main attractive charateristics of supersymmetry is that it solves the "hierarchy problem" resulting from the naturalness argument, there are always many debates on whether the concept of naturalness is a good guiding principle for seeking new physics. For example, K. G. Wilson, one of the first physicists who proposed the naturalness argument [88, 89], called it his "blunder" in his later years [90]:

> *The final blunder was a claim that scalar elementary particles were unlikely to occur in elementary particle physics at currently measurable energies unless they were associated with some kind of broken symmetry. The claim was that, otherwise, their masses were likely to be far higher than could be detected. The claim was that it would be unnatural for such particles to have masses small enough to be detectable soon. But this claim makes no sense when one becomes familiar with the history of physics. $\cdots$ This blunder was potentially more serious, if it caused any subsequent researchers to dismiss possibilities for very large or very small values for parameters that now must be taken seriously.*

In supersymmetry, if one wants to solve the hierarchy problem, the squark masses need to be comparable to the electroweak scale in order to cancel the quadratic divergence in the Higgs mass term. However, up to now there is no evidence for the existence of squark at $\sim$ TeV scale. Nima Arkani-Hamed and Savas Dimopoulos [91] proposed that if the naturalness argument is abandoned, all the scalars (i.e. squarks) except for the Higgs can be ultra-heavy, while the fermions (including gauginos and Higgsinos) could still be light through the protection from the R-symmetry (which is a chiral symmetry). This scenario is called the "split supersymmetry" [92, 93], since it has a split mass spectrum for scalars and fermions. With the sacrifice of the naturalness requirement, split supersymmetry could still maintain other attractive charateristics of ordinary low-energy supersymmetry models — e.g. the unification of strong-electroweak couplings, the candidate for the dark matter particles. Furthermore, it can avoid dangerous FCNC and CP-violation processes which are present in

many SUSY models, since these processes are usually mediated by squarks in SUSY.

A striking phenomenological consequence of the split supersymmetry is the existence of long-lived gluinos [94, 95]. Generally speaking, if R-parity conservation is imposed, the gluino usually decays through squark mediation, and since the squarks are ultra-heavy, the decay rate is suppressed, thus the gluino is long-lived (another possibility is that the gluino can decay to the gravitino and a gluon ($\widetilde{\mathrm{g}} \to \mathrm{g}\widetilde{\mathrm{G}}$) as discussed in the last section, but it is also suppressed, by the SUSY-breaking scale $\sqrt{\langle F \rangle_0}$). The possible decay modes of gluino include $\widetilde{\mathrm{g}} \to \mathrm{qq}\widetilde{\chi}^0$, $\widetilde{\mathrm{g}} \to \mathrm{qq}'\widetilde{\chi}^{\pm}$, and $\widetilde{\mathrm{g}} \to \mathrm{g}\widetilde{\chi}^0$. As an example, the lifetime for the $\widetilde{\mathrm{g}} \to \mathrm{qq}\widetilde{\chi}^0$ decay [96] is

$$c\tau_0 \sim 10^{-5}\ \mathrm{m} \left(\frac{m_{\widetilde{\mathrm{q}}}}{\mathrm{PeV}}\right)^4 \left(\frac{\mathrm{TeV}}{m_{\widetilde{\mathrm{g}}}}\right)^5 . \tag{2.76}$$

If the long-lived gluino decays within the collider detector, displaced jet signatures can also be produced and observed.

Chapter 3

The LHC and the CMS Detector

3.1 The Large Hadron Collider

The Large Hadron Collider (LHC) [97] is a hadron accelerator and collider that is part of the European Organization for Nuclear Research's (CERN) accelerator complex (as shown in Figure 3.1). The LHC machine is located in the 26.7 km tunnel under the French-Swiss border. For proton-proton collisions, the proton beams are supplied by the injection chain: LINAC 2 — BOOSTER — Proton Synchrotron (PS) — Super Proton Synchrotron (SPS). The designed center-of-mass energy for proton-proton collisions is 14 TeV, with each proton beam carrying an energy of 7 TeV per proton. As a two-ring accelerator, the two beams of the LHC are crossed at four interaction points, which houses four large detectors, two of them are general purpose detectors located at high-luminosity cross points – the ATLAS detector at Point 1 and the CMS detector at Point 5. The other two more specific detectors – the ALICE and the LHCb detectors – are located at low-luminosity cross points. The schematic layout of the LHC is illustrated in Figure 3.2.

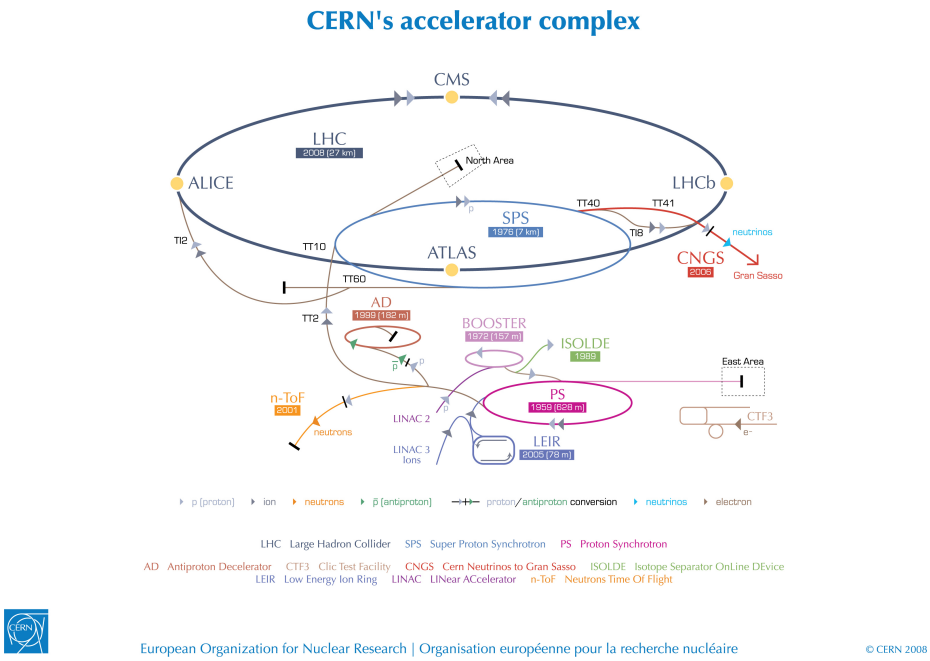

Figure 3.1: CERN's accelerator complex including the LHC machine and the injection chain for the LHC.

The LHC ring accommodates 1,232 main superconducting dipole magnets to steer the proton beams, the dipole magnets are cooled down to 1.9 K using superfluid helium. And there are 858 quadrupole magnets for focusing the proton beams to maximize the luminosity and keep the beams within the beam vacuum.

The instantaneous luminosity of the LHC machine is determined by the following formula:

$$L = \frac{\gamma f N_p^2 n_b}{4\pi\epsilon\beta^*}\left(1+\left(\frac{\theta\sigma_z}{2\sigma_{xy}}\right)^2\right)^{-\frac{1}{2}}, \tag{3.1}$$

where γ is the Lorentz factor, N_p is the number of protons per bunch, n_b is the number of filled bunches per beam, f is the LHC revolution frequency, ϵ is the transverse beam emittance, β^* is the beta function at the collision point, θ is the crossing angle at the collision point, σ_{xy} is the transverse beam size, and σ_z is the longitudinal beam size. The target of the peak luminosities at ATLAS and CMS is $\sim 10^{34}\,\mathrm{cm}^{-1}\mathrm{s}^{-1}$. As

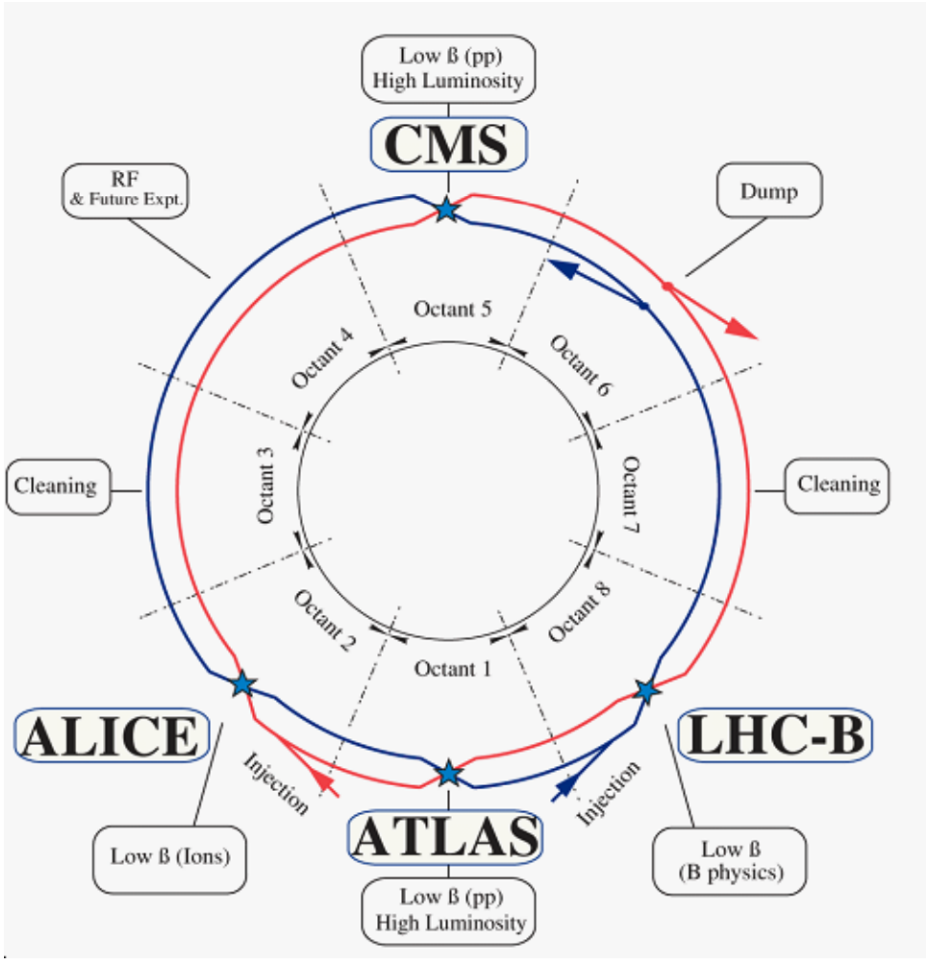

Figure 3.2: The layout of the LHC rings.

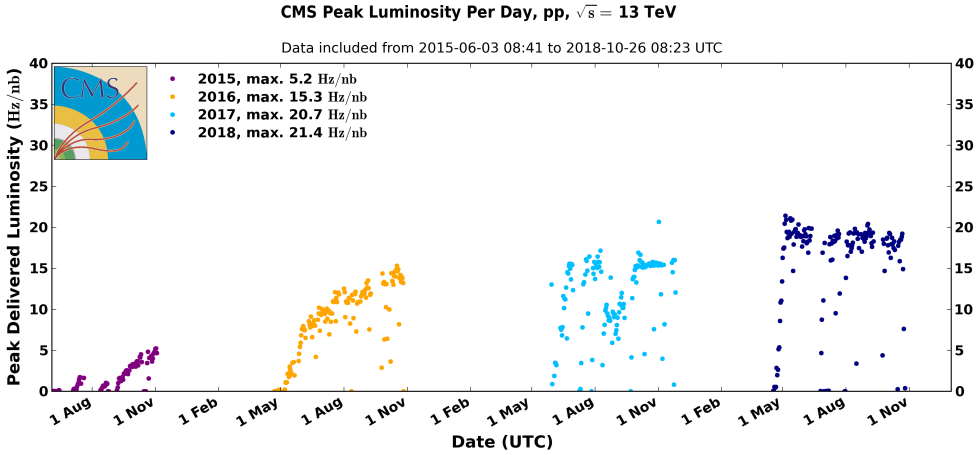

Figure 3.3: The peak proton-proton collision luminosity delivered by the LHC to the CMS detector from 2015 to 2018.

shown in Figure 3.3, the peak luminsosity delivered by the LHC to the CMS detector in 2015 to 2018 reached $\sim 2 \times 10^{34}\,\mathrm{cm}^{-1}\mathrm{s}^{-1}$ (20 Hz/nb), which surpassed the LHC's performance goal.

3.2 The CMS detector

The Compact Muon Solenoid (CMS) detector [98] is a general-purpose particle detector surrounding one of the high-luminosity interaction points of the LHC. It is designed to identify and measure the properties of different final-state particles produced in proton-proton collisions. The main structure of the CMS detector is illustrated in Figure 3.4, which includes a 13-m-long, 6-m-inner-diameter, 3.8-T superconducting solenoid to bend charged particle trajectories. The return field of the solenoid can saturate 1.5 m of iron, allowing the installation of gas-ionization muon stations to precisely measure muon momentum. Thus a 10,000-t iron yoke composed of 3 barrel layers and 6 endcap disks (with three disks at each side) was installed outside the magnetic coil to return the magnetic flux and serve as the absorber for the muon system. The diameter of the outermost barrel layer is 14 m, while the total thickness of the iron yoke layers (in the radial direction) is 1.56 m. Alternately placed with the iron yoke layers are 4 muon stations. Each muon station consists of several drift tubes (DTs) in the barrel region and cathode strip chambers (CSCs) in the endcap region, which are further complemented with resistive plate chambers (RPCs) to provide excellent timing measurements.

Inside the magnet coil sit an inner tracking system consisting of a large silicon strip tracker and a small silicon pixel tracker, an electromagnetic calorimeter (ECAL) made of lead tungstate ($PbWO_4$) crystals, and a brass and scintillator hadron calorimeter

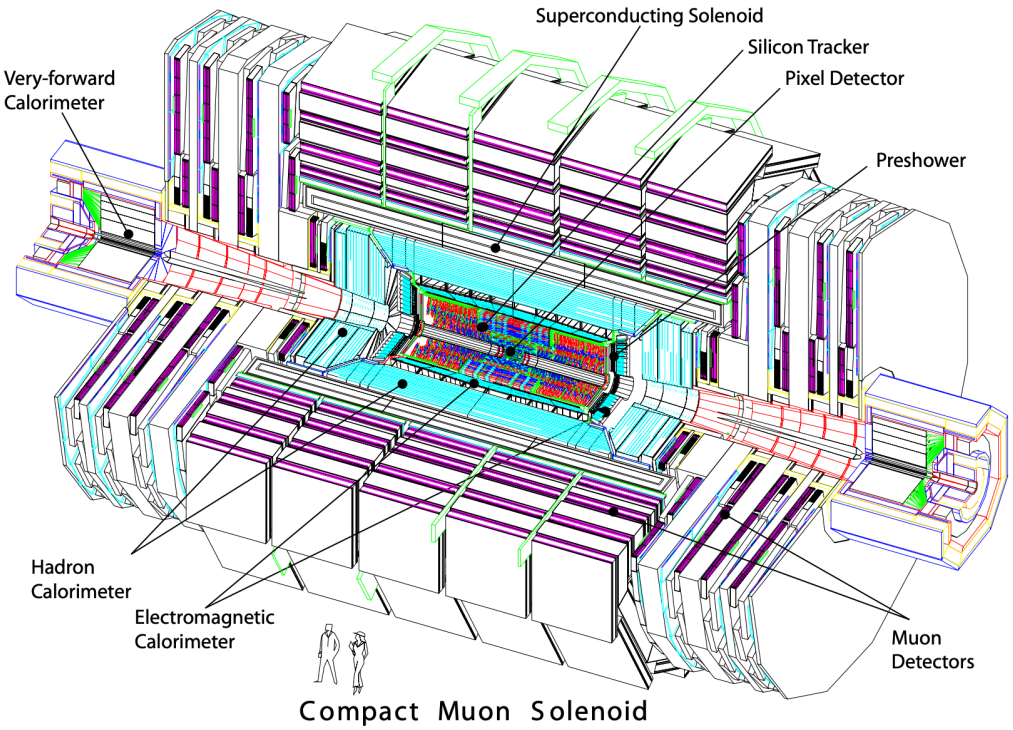

Figure 3.4: An illustration of the CMS detector.

(HCAL).

The convention of the coordinate system adopted by CMS is a right-handed coordinate system with an origin at the nominal collision point inside the detector, the x-axis pointing towards the center of the LHC ring, the y-axis pointing vertically upward, and the z-axis pointing along the beam direction. The azimuthal angle ϕ is the usual angular coordinate in the polar coordinate system defined at the x-y plane, i.e. $\phi = \tan^{-1}(y/x)$. The polar angle θ is measured with respect to the z-axis. The pseudorapidity η is defined as $\eta = -\ln[\tan(\theta/2)]$. The transverse momentum and energy are denoted as p_{T} and E_{T}, which are computed with x and y components. An r-z cross section of the CMS detector with the illustration of different subdetectors is shown in Figure 3.5.

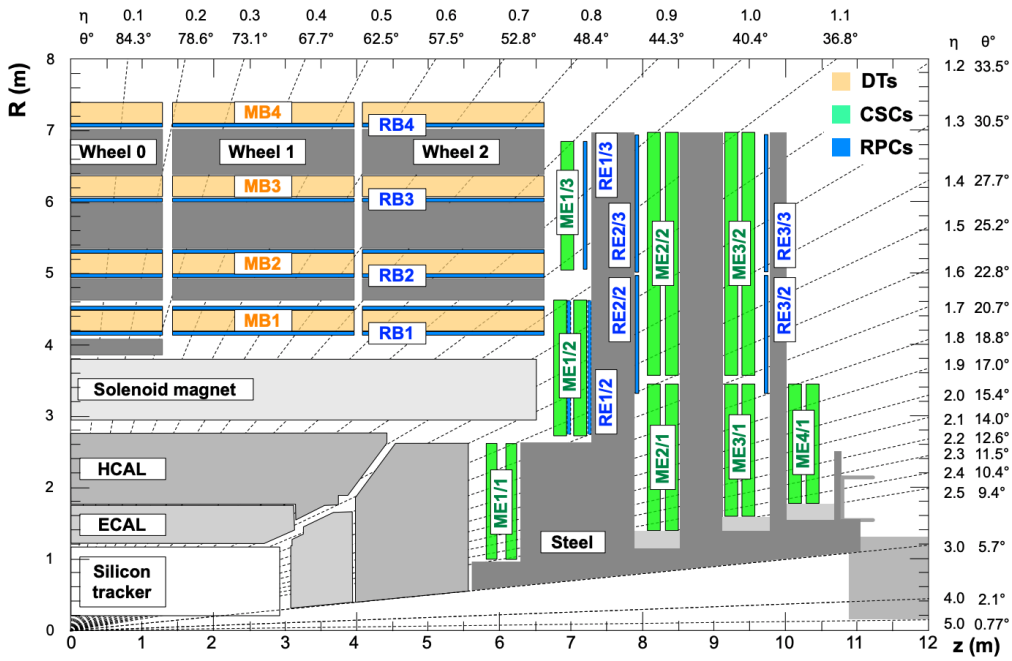

Figure 3.5: An r-z cross section of a quadrant of the CMS detector. The positions of the inner tracking system, ECAL, HCAL, solenoid, iron yoke, and muon stations are shown in the plot.

3.2.1 Inner tracking system

The inner tracking system of the CMS detector is designed to reconstruct and precisely measure charged particle trajectories, as well as reconstruct primary and secondary vertices, which are crucial for the displaced jets search presented in this thesis. The CMS tracker occupies a cylindrical volume with a length of 5.8 m and a diameter of 2.5 m. At the center of the inner tracking system sits a small silicon pixel detector consisting of three barrel layers at radii of 4.3, 7.3, and 10.4 cm, as well as two pairs of endcap disks at $z = \pm 34.5$ and ± 46.5 cm. The pixel detector has 1,440 modules with 66 million pixels, providing a hit position resolution of $\sim 10\mu$m in the transverse directions and $\sim 20 - 40\mu$m in the longitudinal direction. Outside the pixel detector sits a large silicon strip detector which consists of four subsystems – the Tracker Inner Barrel (TIB), the Tracker Inner Disks (TID), the Tracker Outer Barrel (TOB), and

Table 3.1: Summary of the main characteristics of the different tracker subsystems

Tracker subsystem	Layers	Location
Pixel tracker barrel	3 cylindrical	$4.4 < r < 10.2\,\mathrm{cm}$
Strip tracker inner barrel (TIB)	4 cylindrical	$20 < r < 55\,\mathrm{cm}$
Strip tracker outer barrel (TOB)	6 cylindrical	$55 < r < 116\,\mathrm{cm}$
Pixel tracker endcap	2 disks	$34.5 < \lvert z\rvert < 46.5\,\mathrm{cm}$
Strip tracker inner disks (TID)	3 disks	$58 < \lvert z\rvert < 124\,\mathrm{cm}$
Strip tracker endcap (TEC)	9 disks	$124 < \lvert z\rvert < 282\,\mathrm{cm}$

the Tracker Endcaps (TEC). The strip tracker has 15,148 silicon modules with 9.3 million strips. The structure of the CMS tracker is illustrated in Figure 3.6. The main characteristics of the different CMS tracker subsystems are summarized in Table 3.1.

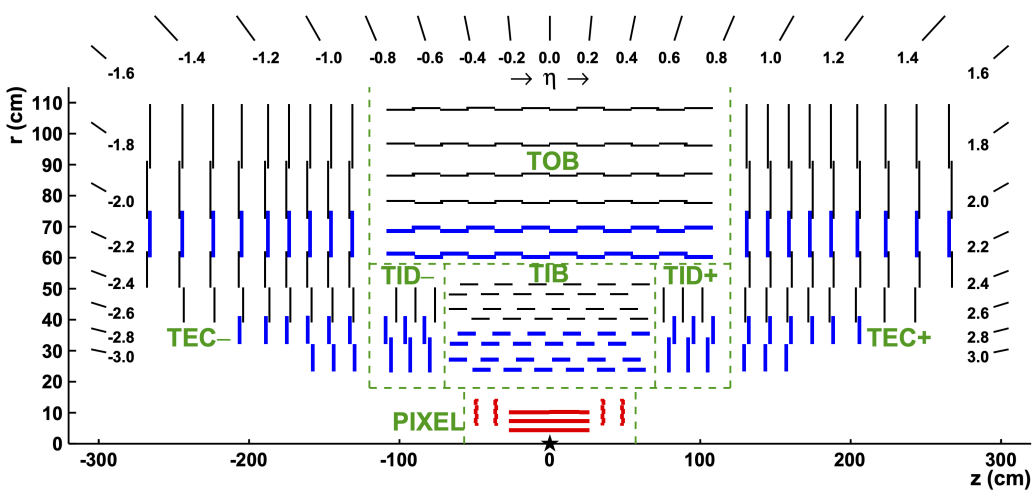

Figure 3.6: Schematic illustration for the structure of the CMS tracker in the r-z plane.

3.2.2 Electromagnetic calorimeter

The CMS electromagnetic calorimeter (ECAL) is a hermetic, homogeneous, fine grained calorimeter composed of lead tungstate ($PbWO_4$) crystals. The choice of $PbWO_4$ is due to its high density (8.28 g/ cm^3) and short radiation length (X_0 =

0.89 cm), and thus is suitable for building a calorimeter with good energy resolution and compact size. The central barrel region (EB) of ECAL covers a pseudorapidity region of $|\eta| < 1.48$ starting from a radius of 129 cm. The EB consists of 36 supermodules, with each supermodule having 1700 $PbWO_4$ crystals. The length of each crystal is 230 mm, which is equivalent to 25.8 X_0 in terms of the radiation length. The alignment of the crystals is quasi-projective, with a small tilt angle ($\sim 3^\circ$) with respect to the interaction point to avoid cracks aligned with particle trajectories. The endcap region (EE) covers a pseudorapidity region of $1.48 < |\eta| < 3.00$ and starts from $|z| = 315.4$ cm. The endcaps are composed of 14,648 crystals, with each crystal having a length of 220 mm (24.7 X_0). A preshower section consisting of two planes of silicon strip sensors as well as two disks of lead absorber is placed in front of the endcaps to improve the π^0-photon discrimination.

To detect the scintillation light produced in the $PbWO_4$ crystals, silicon avalanche photodiodes (APDs) are used as photodetectors in the EB, while vacuum phototriodes (VPTs) are used in the EE to overcome the large radiation doses in the forward region. To compensate for the small light yield of the $PbWO_4$ crystals, these photodetectors are set to have high internal gain (~ 50 for APDs, ~ 10 for VPTs). The dependences on temperature for the light yield of the $PbWO_4$ crystal and the gains of the photodetectors require temperature stability of $\pm 0.05^\circ$C in EB and $\pm 0.1^\circ$C in EE.

The energy and time resolutions of ECAL crystal arrays are measured at beam tests. For electron beams impacting centrally at a 3×3 crystal array, the energy resolution can be parameterized as:

$$\frac{\sigma_E}{E} = \frac{2.8\%}{\sqrt{E/\,\mathrm{GeV}}} \oplus \frac{12.8\%}{E/\,\mathrm{GeV}} \oplus 0.3\%. \tag{3.2}$$

3.2.3 Hadron calorimeter

The CMS hadron calorimeter (HCAL) is composed of four major sections: the HCAL barrel (HB) [99], HCAL endcaps (HE) [100], HCAL outer (HO), and HCAL forward (HF). A schematic view of the HCAL system is shown in Figure 3.7. The HB and HE, which sit inside the magnetic coil, are sampling calorimeters with brass as the absorber and plastic scintillator as the active material, having a sampling fraction of $\sim 7\%$. The HB part of HCAL consists of 32 wedges covering $|\eta| < 1.4$, which can be further divided into 2,304 cells with a segmentation of $\Delta\eta \times \Delta\phi = 0.087 \times 0.087$. The HE part of HCAL also consists of 2,304 cells, covering the pseudorapidity region of $1.3 < |\eta| < 3.0$, with a ϕ segmentation of $\Delta\phi = 5^\circ$ and an η segmentation varying from 0.087 to 0.35 at different η values. The HO part of HCAL is placed outside the cryostat and solenoid coil and utilizes them as additional absorbers for sampling the hadronic shower penetrating through ECAL and HB, thus helps mitigate the non-Gaussian tail of the energy resolution function and improve the $E_{\mathrm{T}}^{\mathrm{miss}}$ resolution of the CMS detector. The HO consists of 5 "rings", which contain scintillators with a thickness of 10 mm, covering the pseudorapidity region of $|\eta| < 1.26$. For HE, HB, and HO, the scintillation light is collected using embedded wave-length shifting (WLS) fibers. The WLS fibers carry the scintillation light to the photodetectors, which are based on multi-channel hybrid photodiodes (HPDs) (The photodectors were later upgraded to SiPMs in Run 2). The signals from the photodetectors are then translated into measurements of the energy deposits of the hadronic showers.

3.2.4 Track reconstruction

In collider physics, a "track" represents a trajectory left by a charged particle. The movement of a charged particle in the magnetic field can be characterized by five

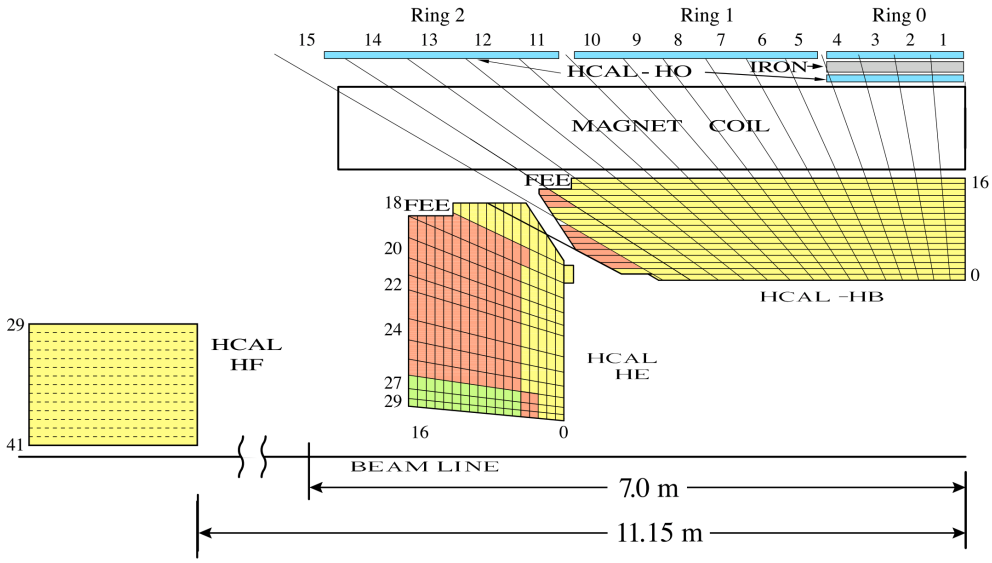

Figure 3.7: The schematic view of the CMS hadron calorimeter system in the r-z plane.

free parameters. For example, if we choose an arbitrary plane the charged particle intersects (which is called the "reference surface"), these five parameters could be two for the coordinates of the impact point at the reference surface, two describing the direction of the movement at the impact point, and one for the momentum of the charged particle. The task of track reconstruction then includes finding the track candidates (*track finding*) and finding the best estimation of the five track parameters (*track fitting*). Track finding and track fitting are extremely important for the identification and measurement of the relevant physical particles.

The theoretical foundation of the track finding and fitting in CMS is based on the **Kalman filter** [101]. In the Kalman filter, the state of the track at a given "surface" (i.e. pixel or strip tracker layer) can be described by a 5-component state vector $\vec{x}_k$, then the state vector at the next *surface* (layer) can be predicted as:

$$\vec{x}_{k+1} = \mathbf{F}_k \vec{x}_k + \vec{\omega}_k, \tag{3.3}$$

where $\mathbf{F}_k$ is a transfer matrix determined by the equation of motion of charged particles in the magnetic field, and $\vec{\omega}$ represents some Gaussian noise with zero expectation value. The covariance matrix of $\vec{\omega}$ is denoted by $\mathbf{Q}$. The measurement of the state vector is described by:

$$\vec{m}_k = \mathbf{H}_k \vec{x}_k + \vec{\epsilon}_k, \tag{3.4}$$

where $\vec{m}_k$ is the measurement made by the detector, $\vec{\epsilon}$ represents some Gaussian noise with zero expectation value and $\mathbf{V}$ as its covariance matrix. The Kalman filter seeks to find the best estimation of the state vectors based on the measurements $\vec{m}_k$, which consists of the following steps:

- **Prediction**: suppose we have an estimation of the state vector at the $(k-1)$-th surface, $\hat{\vec{x}}_{k-1}$, as well as its covariance matrix $\mathbf{C}_{k-1}$, the prediction for the state vector at the k-th surface is then:

$$\hat{\vec{x}}_k = \mathbf{F}_{k-1} \hat{\vec{x}}_{k-1}, \tag{3.5}$$

$$\mathbf{C}_k = \mathbf{F}_{k-1} \mathbf{C}_{k-1} \mathbf{F}_{k-1}^T + \mathbf{Q}_{k-1}. \tag{3.6}$$

- **Filtering**: now we can compare the prediction with the measurement at the k-th surface, and then update our predictions to be:

$$\hat{\vec{x}}_{k,\text{filtered}} = \hat{\vec{x}}_k + \mathbf{K}_k \left(\vec{m}_k - \mathbf{H}_k \hat{\vec{x}}_k \right), \tag{3.7}$$

$$\mathbf{C}_{k,\text{filtered}} = (\mathbf{I} - \mathbf{K}_k \mathbf{H}_k) \mathbf{C}_k, \tag{3.8}$$

  where $\mathbf{K}_k$ is the Kalman gain matrix $\mathbf{K}_k = \mathbf{C}_k \mathbf{H}_k^T \left(\mathbf{V}_k + \mathbf{H}_k \mathbf{C}_k \mathbf{H}_k^T \right)^{-1}$.

- **Smoothing**: after the prediction and filtering reach the state vector $\vec{x}_n$ at the last surface (layer), the final estimation of $\vec{x}_n$ after the filtering $\hat{\vec{x}}_{n,\text{filtered}}$ contains the information of all the measurements $(\vec{m}_1, \vec{m}_2, \ldots, \vec{m}_n)$, thus we relabel it as

$\hat{\vec{x}}_{n,\text{smoothed}}$. Then all the state vectors in the previous surfaces (layers) can be updated through a "back propagation" process starting from $\hat{\vec{x}}_{n,\text{smoothed}}$:

$$\hat{\vec{x}}_{k,\text{smoothed}} = \hat{\vec{x}}_{k,\text{filtered}} + \mathbf{A}_k \left(\hat{\vec{x}}_{k+1,\text{smoothed}} - \hat{\vec{x}}_{k+1} \right), \tag{3.9}$$

$$\mathbf{C}_{k,\text{smoothed}} = \mathbf{C}_{k,\text{filtered}} + \mathbf{A}_k \left(\mathbf{C}_{k+1,\text{smoothed}} - \mathbf{C}_{k+1} \right) \mathbf{A}_k^T, \tag{3.10}$$

where $\mathbf{A}_k = \mathbf{C}_{k,\text{filtered}} \mathbf{F}_k^T \mathbf{C}_{k+1}^{-1}$.

Due to the high energy and high luminosity for the proton-proton collisions at the LHC, the density of tracks is extremely large especially in the case of high pileup, therefore the hit-to-track assignment becomes very challenging. The wrong hit-to-track assignment would lead to degraded track reconstruction performance. To mitigate this problem, the CMS detector adopted an adaptive version of the Kalman filter during Run 2, called **Deterministic Annealing Filter** (DAF). In DAF, after the initial Kalman filter was applied, at a given layer k, we now consider N possible hits that can be assigned to the track $(\vec{m}_{k,1}, \vec{m}_{k,2}, \ldots, \vec{m}_{k,N})$, and assign a weight factor to each hit:

$$w_i(\vec{m}_{k,i}) = \frac{\exp\left(-\chi_i^2/2T\right)}{\sum_{j=1}^{N} \exp\left(-\chi_j^2/2T\right) + N \exp\left(-\chi_c^2/T\right)}, \tag{3.11}$$

where χ_i^2 is the χ^2 between the hit $\vec{m}_{k,i}$ and the expected measurement of the smoothed track state vector $(\mathbf{H}_k \hat{\vec{x}}_{k,\text{smoothed}})$, χ_c^2 is a preset threshold value, and T is the "temperature" for annealing. The different hits $(\vec{m}_{k,1}, \vec{m}_{k,2}, \ldots, \vec{m}_{k,N})$ are then combined to a single "`MultiRecHit`":

$$\vec{m}_k' = \left(\sum_i w_i \mathbf{V}_i^{-1} \right)^{-1} \sum_i w_i \mathbf{V}_i{}^{-1} \vec{m}_{k,i}, \tag{3.12}$$

with a covariance matrix $\mathbf{V}'$ associated with $\vec{m}_k'$:

$$\mathbf{V}' = \left(\sum_i w_i \mathbf{V}_i^{-1} \right)^{-1}. \tag{3.13}$$

Then several iterations of the Kalman filter were applied with $\vec{m}_k$ and $\mathbf{V}$ replaced by $\vec{m}'_k$ and $\mathbf{V}'$. In each iteration the temperature T is decreased till $T = 1$. As a result, the hits that are less compatible with the track are downweighted in each step. With DAF, the track reconstruction are more immune to wrong track-hit assignments and thus have better performance in the high pileup environment.

In the CMS detector, the track reconstruction starts from the **hit reconstruction**, where the signals above specific thresholds in pixel and strip channels are clustered into "hits." The initial estimation of the hit position (and the corresponding uncertainty) is determined by the charge and the position of the end pixels of the cluster and is corrected for the Lorentz drift in the magnetic field. This initial estimation of the hit position is utilized in the following steps of seed generation and track finding, as will be described below.

In the **seed generation**, the initial possible track candidates are formed, which serve as the starting points for the propagation using the Kalman filter. The CMS detector utilizes an iterative tracking process, with each iteration starting from a specific group of seeds. The seeds are formed using two or three hits in the different layers of pixel detector and strip detector, which are summarized in Table 3.2. The earlier iterations utilizes hits in the pixel detector to target prompt tracks, while later iterations focus on tracks with larger displacements. After each iteration, hits associated with reconstructed tracks are removed. In this way, the CMS tracking becomes efficient for reconstructing tracks with different displacements. Besides the iterations listed in Table 3.2, there are also some special iterations of tracking to recover the tracking efficiencies for high p_{T} jets and muons.

Table 3.2: The main iterations of seed generation in the CMS detector before the Phase 1 upgrade.

Iteration	Name	Seeding	Target tracks
0	Initial	pixel triplets	prompt, high p_{T}
1	DetachedTriplet	pixel triplets	from b hadron decays, $R \lesssim 5\,\mathrm{cm}$
2	LowPtTriplet	pixel triplets	prompt, low p_{T}
3	PixelPair	pixel pairs	prompt, recover high p_{T}
4	MixedTriplet	pixel+strip triplets	displaced, $R \lesssim 7\,\mathrm{cm}$
5	PixelLess	inner strip pairs	displaced, $R \lesssim 25\,\mathrm{cm}$
6	TobTec	outer strip pairs	displaced, $R \lesssim 60\,\mathrm{cm}$

After the seeds belonging to a given iteration are formed, a Combinatorial Track Finder based on the Deterministic Annealing Kalman Filter described above is performed, where the track candidates produced by the seeds are extrapolated to the next compatible layer using the Kalman Filter. After the extrapolation reaches the final layer, track fitting is achieved by updating the track parameters through the smoothing step of the Kalman filter as well as the following annealing schedule. The track candidates with too many missing hits or with p_{T} below some specific value are dropped. Since all the seeds are extrapolated at the same time, there could be some tracks with significant overlaps; When two tracks share more than 19% of the hits, the one with smaller number of hits or larger χ^2 is discarded.

To reduce the fraction of fake tracks, after the track reconstruction tracks are classified as *Loose*, *Tight*, or *High Purity* utilizing the information such as the χ^2 of the track fit, the impact parameters and the hits in different layers. The classification is optimized separately for each iteration and thus is efficient for selecting tracks with different displacement. The "High Purity" tracks have the best quality and thus are utilized in the analysis presented in this thesis.

3.2.5 Jet reconstruction and corrections

There are mainly two types of jets that are utilized in the physics analyses in the CMS experiment, one is the particle flow (PF) jets, the other one is the calorimeter (CALO) jets. Though PF jets usually have better performance compared to the CALO jets, they are optimized for jets produced promptly with respect to the interaction point, and thus can be biased for displaced jets. Therefore, in the search presented in this thesis, we mainly consider the CALO jets.

The CALO jets are reconstructed solely from the energy deposits in the calorimeter towers. A calorimeter tower consists of one HCAL cell and the geometrically corresponding (in the η-ϕ plane) ECAL crystals. For example, in the barrel region one HCAL cell can be mapped to an array of 5×5 ECAL crystals. The contribution from each calorimeter tower is assigned a momentum, the absolute value and the direction of which are given by the energy measured in the tower and the coordinates of the tower. The CALO jets are then reconstructed from the energy deposits in the calorimeter towers, clustered using the anti-k_{T} algorithm [102, 103] with a distance parameter of 0.4.

The anti-k_{T} algorithm is a sequential clustering algorithm, in which one introduces distances d_{ij} between entities (in the case of CALO jets, the entities are calorimeter towers) i and j based on their transverse momenta, as well as a "beam distance" d_{iB}:

$$d_{ij} = \min\left(k_{\mathrm{T}i}^{-2}, k_{\mathrm{T}j}^{-2}\right)\frac{\Delta_{ij}^2}{R^2}, \tag{3.14}$$

$$d_{iB} = k_{\mathrm{T}i}^{-2}, \tag{3.15}$$

where Δ_{ij} is the angular distance in the η-ϕ plane: $\Delta_{ij} = \sqrt{(\phi_i - \phi_j)^2 + (\eta_i - \eta_j)^2}$, and R is a preset constant called the "distance parameter". For a given entity i, if

there is no j satisfying $d_{ij} < d_{iB}$ then i is called a "jet" and is removed from the list of entities, otherwise j is absorbed into i and the distances are recalculated. This procedure is repeated until no entity is left, which results in a group of jets. The anti-k_{T} algorithm is collinear-safe and infrared safe, therefore it is widely taken as the standard jet reconstruction algorithm in collider physics.

After a CALO jet is reconstructed, the raw jet energy is obtained from the sum of the tower energies, and the raw jet momentum from the vector sum of the tower momenta, which results in a nonzero jet mass. The raw jet energies are then corrected to establish a relative uniform response of the calorimeter in η and a calibrated absolute response in transverse momentum p_{T} [104]. The first stage of the jet corrections is a correction for the contributions due to pileup effects, which is referred to as the L1Fast correction; The second stage of the jet corrections is a correction based on simulated QCD multijet samples by comparing the energies of reconstructed jets and the energies of particle-level jets in the MC simulation, which is referred to as the L2L3 correction. Finally, for data, the differences in the jet energy responses between data and MC simulation are studied and calibrated using dijet, Z+jet, γ+jet, and multijet events, these differences are then parameterized as functions of (η, p_{T}) and are corrected for, which is referred as the L2L3Residual correction.

Chapter 4

Triggers, Data Sets, and MC Simulations

4.1 Trigger implementation

Our goal in the search presented in this thesis is to probe long-lived particles with displaced jet signatures in a way that is as model-independent as possible. Therefore we'd like to have a minimum requirement on the additional objects. Specially designed BLT triggers are therefore necessary for capturing displaced jet signatures. During Run 2 of the LHC, the main displaced jet HLT paths are:

- `HLT_HT350_DisplacedDijet40_DisplacedTrack_v`
- `HLT_HT500_DisplacedDijet40_Inclusive_v`

Both triggers impose an H_{T} requirement, where H_{T} is defined as the scalar sum of the transverse momentum of all the CALO jets that satisfy $p_{\mathrm{T}} > 40\,\mathrm{GeV}$ and $|\eta| < 2.5$. The triggers also require the existence of at least two CALO jets, each of them satisfying:

- $p_{\mathrm{T}} > 40\,\mathrm{GeV}$, and $|\eta| < 2.0$;
- at most two associated prompt tracks, which are tracks having a transverse impact parameter ($\mathrm{IP}_{\mathrm{2D}}$) smaller than 1.0 mm . The track candidates are selected from the three iterations (`iter0`, `iter1`, `iter2`) of HLT regional iterative tracking (which is the standard CMS online tracking), and are associated with the jets using jet-track association at the primary vertex with $\Delta R = 0.4$.

For the displaced track path, an additional requirement is imposed on the CALO jets:

- having at least one track that satisfying $\mathrm{IP}_{\mathrm{2D}} > 500\,\mu\mathrm{m}$, $\mathrm{Sig}[\mathrm{IP}_{\mathrm{2D}}] > 5.0$, where $\mathrm{Sig}[\mathrm{IP}_{\mathrm{2D}}]$ is the ratio between $\mathrm{IP}_{\mathrm{2D}}$ and its error. The track candidates here are selected from four iterations (`iter0`, `iter1`, `iter2`, `iter4`) of HLT regional iterative tracking, and are associated with the jets using jet-track association at the primary vertex with $\Delta R = 0.4$.

Apart from the two paths listed above, there are two other control paths with the same jet and track requirements but lower HLT H_{T} cut:

- `HLT_HT250_DisplacedDijet40_DisplacedTrack_v`
- `HLT_HT400_DisplacedDijet40_Inclusive_v`

They were designed to monitor the trigger efficiency performance for the online CALO H_{T} requirement. However, these control paths use the same L1 HTT seeds as the signal paths, so they can not spot potential problems due to L1 HTT inefficiency. Thus we instead use an orthogonal data set to monitor the performance of CALO H_{T} filter, which will be explained in detail in section 7.1.1.

To avoid possible mismodeling for trigger efficiencies in the MC samples, we require the triggers are matched with the following offline CALO H_{T} requirements in data:

- `HLT_HT350_DisplacedDijet40_DisplacedTrack_v` AND the offline CALO H_{T} is larger than 400 GeV;
- `HLT_HT500_DisplacedDijet40_Inclusive_v` AND the offline CALO H_{T} is larger than 560 GeV.

In 2016, the inclusive path `HLT_HT500_DisplacedDijet40_Inclusive_v` was disabled due to the rate limit, thus the data taken in 2016 for this analysis came from:

- `HLT_HT350_DisplacedDijet40_DisplacedTrack_v` AND the offline CALO H_{T} is larger than 400 GeV.

The performance of the displaced jet trigger as well as the corresponding systematic uncertainties will be discussed in detail in section 7.1.

4.2 Data sets

The data collected by the displaced jet trigger are routine and saved as special primary data sets – "DisplacedJet" data sets, which this search mainly relies upon. The DisplacedJet data sets are further filtered by the 25ns "golden JSON file" in 2016 to ensure good data-taking quality, as shown in Table 4.2.
To measure the efficiency of the HLT CALO H_{T} filter, we also utilized the events in "SingleMuon" primary data sets: `/SingleMuon/*/AOD`, which are collected by single muon triggers.

4.3 Background MC simulation

The possible background sources for displaced jet searches include:

- the nuclear interactions between hadrons and detector material;

Table 4.1: The data sets and certification JSON file used in the analysis.

Data sets
/DisplacedJet/Run2016B-23Sep2016-v3/AOD
/DisplacedJet/Run2016C-23Sep2016-v1/AOD
/DisplacedJet/Run2016D-23Sep2016-v1/AOD
/DisplacedJet/Run2016E-23Sep2016-v1/AOD
/DisplacedJet/Run2016F-23Sep2016-v1/AOD
/DisplacedJet/Run2016G-23Sep2016-v1/AOD
/DisplacedJet/Run2016H-PromptReco-v2/AOD
/DisplacedJet/Run2016H-PromptReco-v3/AOD

Json file
Cert_271036-284044_13TeV_23Sep2016ReReco_Collisions16_JSON.txt

- heavy-flavor jets with strikingly displaced decays;
- fake displaced vertices formed by randomly crossing tracks.

These background sources are expected to mainly arise from QCD multijet events, the QCD multijet samples used in the analysis are listed in Table 4.2. The samples are simulated with MadGraph5_aMC@NLO 2.2.2 [105] at leading order, which is interfaced with PYTHIA 8.212 [106] for parton showering, hadronization, and fragmentation. Jets from the matrix element calculations are matched to parton shower jets using the MLM algorithm [107]. The CUETP8M1 tune [108] is used for modeling the underlying event. For parton distribution function (PDF) modeling, the NNPDF3.0 PDF set [109] is used. The production of these samples is binned based on different generator-level H_{T}, each sample is then reweighted according to its cross sections and the number of completed events respectively.

Table 4.2: The QCD multijet simulation samples and their cross sections used in the analysis

Reconstruction condition and data tier: `/RunIISummer16DR80Premix-PUMoriond17_80X_*/AODSIM`	cross section (pb)
QCD_HT300to500_TuneCUETP8M1_13TeV-madgraphMLM-pythia8	347700
QCD_HT500to700_TuneCUETP8M1_13TeV-madgraphMLM-pythia8	32100
QCD_HT700to1000_TuneCUETP8M1_13TeV-madgraphMLM-pythia8	6831
QCD_HT1000to1500_TuneCUETP8M1_13TeV-madgraphMLM-pythia8	1207
QCD_HT1500to2000_TuneCUETP8M1_13TeV-madgraphMLM-pythia8	119.9
QCD_HT2000toInf_TuneCUETP8M1_13TeV-madgraphMLM-pythia8	25.24

4.4 Signal MC simulation

This search is designed to be sensitive to a variety of long-lived models with displaced jet signatures. We therefore tested with a group of signal models with different final-state topologies containing displaced jets. All the signal samples are produced with PYTHIA 8.212, and NNPDF2.3QED [110] is used for PDF modeling. In the SUSY models, when a gluino or top squark is long lived, it will have enough time to form a hadronic state, an R-hadron [79, 111, 112], which is simulated with PYTHIA. For underlying event modeling the CUETP8M1 tune is utilized.

4.4.1 Jet-jet model

In the (simplified) jet-jet model, two long-lived neutral particles (X) are pair produced, mediated by an off-shell Z boson (through the derivative coupling $\mathrm{Z}^{\mu} X_1^* \partial_{\mu} X_2$). Then each particle can decay into a quark-antiquark pair with flavor to be u, d, s, c, and b, the decay rate to each flavor is the same. The samples are produced with different mass points (m_X = 50, 100, 300, 500, 700, 1000, 3000 GeV) and different decay lengths in the rest frame ($c\tau_0$ = 1, 3, 10, 30, 100, 300, 1000, 2000 mm).

4.4.2 General gauge mediation $\widetilde{\mathrm{g}} \to \mathrm{g}\widetilde{\mathrm{G}}$

We also considered a GMSB SUSY model in the general gauge mediation scenario, where gluinos are pair produced, and the gravitino is the LSP whilst the gluino is the NLSP and long lived. After the gluino is produced, it forms an R-hadron, and then decays to a gluon and a gravitino, producing a displaced single jet and missing transverse momentum. The samples are produced with gluino masses from 800 GeV to 2500 GeV, the proper decay length of the gluino varies from 1 mm to 10 m.

4.4.3 R-parity violating $\widetilde{\mathrm{g}} \to \mathrm{tbs}$

The second SUSY model is an RPV SUSY model [113] with minimum flavor violation, where the gluino is long lived and decays to a top quark and a top squark, the top squark is assumed to be virtual and decays to a strange antiquark and a bottom antiquark through the RPV interaction with strength given by the coupling λ''_{323} [114], effectively resulting in a three-body decay with a "multijet" final-state topology. This model is referred to as the $\widetilde{\mathrm{g}} \to \mathrm{tbs}$ model. The samples are produced with gluino masses from 1200 to 3000 GeV, and a proper decay length varying from 1 mm to 10 m.

4.4.4 R-parity violating $\widetilde{\mathrm{t}} \to \mathrm{b}\ell$

We also considered another RPV SUSY model [115], in which the long-lived top squark decays to a bottom quark and a charged lepton via RPV interactions with strengths given by couplings λ'_{133}, λ'_{233}, and λ'_{333} [114] defined in equation 2.61, assuming the decay rate to each of the three lepton flavors (e, μ, and τ) to be equal, referred to as the $\widetilde{\mathrm{t}} \to \mathrm{b}\ell$ model. The samples are produced with different top squark masses from 200 to 1600 GeV, and a proper decay length varying from 1 mm to 1 m.

4.4.5 Dynamical *R*-parity violating $\widetilde{\mathrm{t}} \to \overline{\mathrm{dd}}$

We also consider another SUSY model motivated by dynamical R-parity violation (dRPV) [80, 116], where the long-lived top squark decays to two down antiquarks via RPV interaction with strength given by a nonholomorphic RPV coupling η''_{311} [81], referred to as the $\widetilde{\mathrm{t}} \to \overline{\mathrm{dd}}$ model. The samples are produced with different top squark masses from 800 to 1800 GeV, and proper decay length varying from 1 mm to 10 m.

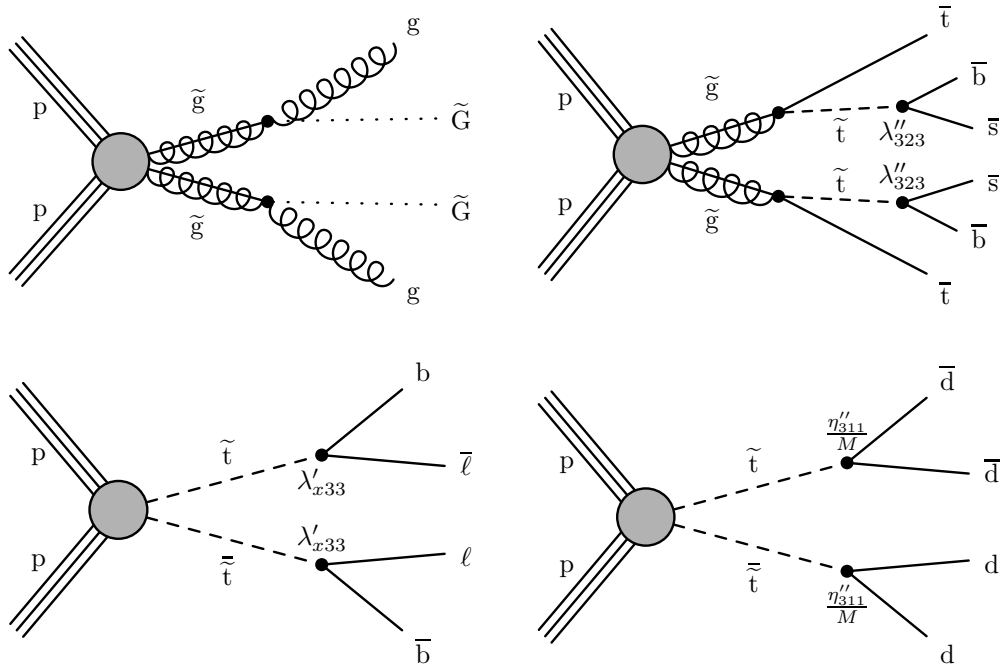

Figure 4.1: The Feynman diagrams for different long-lived SUSY models considered, including general gauge mediation with $\widetilde{\mathrm{g}} \to \mathrm{g}\widetilde{\mathrm{G}}$ decay (upper left), RPV SUSY with $\widetilde{\mathrm{g}} \to \mathrm{tbs}$ decay (upper right), RPV SUSY with $\widetilde{\mathrm{t}} \to \mathrm{b}\ell$ decay (lower left), dynamical RPV SUSY with $\widetilde{\mathrm{t}} \to \overline{\mathrm{dd}}$ decay (lower right).

4.5 Pileup reweighting

In the MC simulation samples, the pileup (i.e. the additional pp interactions within the same or nearby bunch crossings) distribution is not perfectly matched to the real

data. Therefore, a reweighting procedure is performed to match the pileup distributions. In the MC samples, the pileup for each event can be accessed through the true number of interactions information. While in the real data, the pileup distribution can be calculated based on the per bunch crossing instantaneous luminosity measurement and minimum bias cross section measurement. A per-event reweight factor is then assigned to the MC samples to match the pileup in the collected data.

Chapter 5

Displaced Jets Reconstruction and Event Selections

5.1 Analysis strategy

5.1.1 Jet kinematics

The reconstruction of the displaced dijet candidates starts from looking for a pair of calorimeter jets, which are reconstructed with the anti-k_t algorithm ($\Delta R = 0.4$). The calorimeter jets in both data and MC are corrected through L1FastJet, L2 and L3 jet corrections. For the jets in data, L2L3Residuals corrections are also applied to compensate the small differences for jet response in data and MC. The jets are required to satisfy $p_{\mathrm{T}} > 50\,\mathrm{GeV}$, $|\eta| < 2.0$. The kinematics of the calorimeter jets as well as the offline CALO H_{T} in events collected by the displaced dijet paths are shown in Figure 5.1.

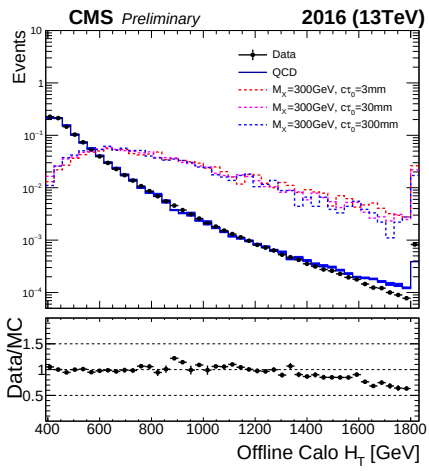

(a) Offline CALO H_{T}

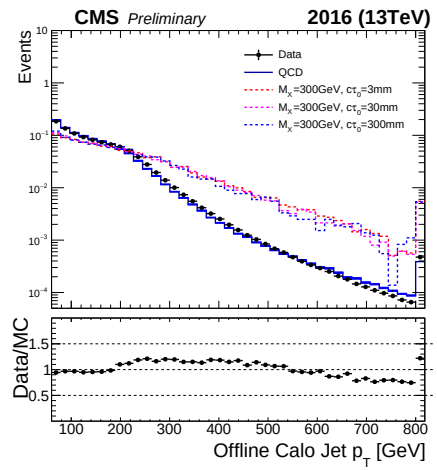

(b) Offline CALO jet p_{T}

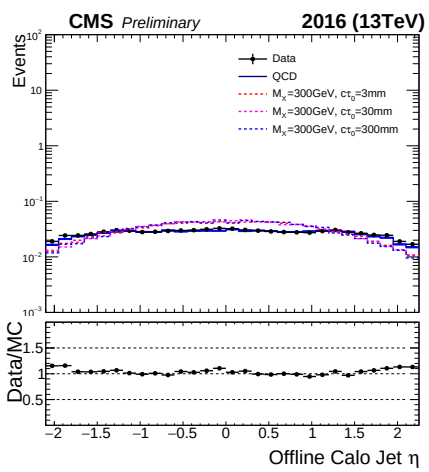

(c) Offline CALO jet η

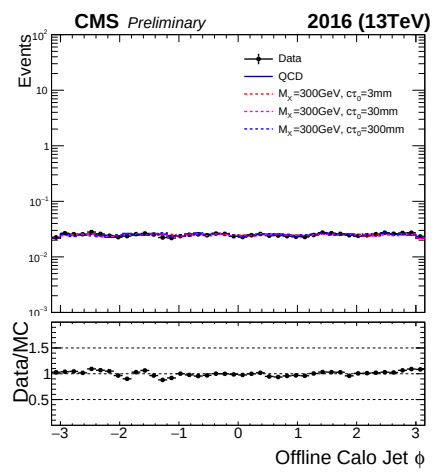

(d) Offline CALO jet ϕ

Figure 5.1: The distributions of offline CALO H_{T} and p_{T}, η, ϕ of CALO jets for data, simulated QCD multijet events, and simulated signal events. All the events are collected by the displaced jet trigger with offline CALO H_{T} cut. Both the data and simulated samples are unit normalized. The signal distributions are shown for the jet-jet model with m_X =300 GeV at different proper decay lengths $c\tau_0$ (3 mm, 30 mm, and 300 mm.

5.1.2 Jet-track association

If the long-lived particles decay within the tracker, multiple displaced tracks can be found, and their properties are crucial for this analysis. In order to suppress the background coming from nuclear interactions or accidentally crossed tracks, we require that the tracks are associated with the dijet system.

To find all the tracks associated with the dijet system, two different algorithms are considered. The first one is the jet-track association at the primary vertex (`JTA@VTX`), in which the η and ϕ of a track is computed using its momentum vector at the closest approach point with respect to the primary vertex. The angular distance of the jet and the track in the $\eta - \phi$ plane is then determined by:

$$\Delta R = \sqrt{(\eta_{\text{jet}} - \eta_{\text{track}})^2 + (\phi_{\text{jet}} - \phi_{\text{track}})^2} \tag{5.1}$$

A track is said to be associated with a jet when $\Delta R < \Delta R_0 = 0.5$. In the dijet system, when one track satisfies $\Delta R < 0.5$ for both jets, it is associated with the jet with smaller ΔR. Ideally, the (η, ϕ) of the tracks and the jets should be computed and compared at the secondary vertex. However, the jet-track association at the secondary vertex is not realistic since we need to pick up the tracks first to fit the vertex. In order to compensate the mismodeling in the jet-track association, the ΔR_0 is chosen to be slightly larger than the cone size in the jet reconstruction algorithm (0.4).

We also studied the jet-track association at the calorimeter face (`JTA@CALO`), in which tracks are extrapolated to the calorimeter face according to their curvature in the magnetic field (the extrapolation starts from the outermost hit of the track in the tracker). The (η, ϕ) of the track is determined by the impact point at the calorimeter face in the detector coordinate system. Then the track and the jet are also associated

based on ΔR in the η-ϕ plane just as in `JTA@VTX`. The impact of two different jet-track association algorithms will be studied in the following sections.

5.1.3 Secondary vertex reconstruction

To fit a secondary vertex from the tracks associated with the dijet system, we select the tracks that are displaced, specifically we require that the transverse impact parameters of the tracks are larger than $500\,\mu$m and the significances of the transverse impact parameters are larger than 5.0:

$$\mathrm{IP}_{\mathrm{2D}} > 500\,\mu\mathrm{m}, \quad \mathrm{Sig}[\mathrm{IP}_{\mathrm{2D}}] > 5.0, \tag{5.2}$$

where the transverse impact parameter is defined as the distance in the x-y plane between the closest approach point of the track with respect to the leading primary vertex (PV) and the PV itself. The leading primary vertex is chosen from the offline primary vertices collection with a new selection technique implemented in Run 2, in which the reconstructed vertex with the largest value of summed physics-object p_{T}^2 is taken to be the primary pp interaction vertex, referred to as the leading PV. The physics objects are those returned by a jet finding algorithm applied to all charged tracks associated with the vertex, plus the corresponding associated missing transverse momentum.

To ensure the quality of the tracks, we also require that:

- $p_{\mathrm{T}} > 1\,\mathrm{GeV}$;
- The track is *high-purity*.

From the selected displaced tracks, a secondary vertex is reconstructed using the Adaptive Vertex Fitter (AVF) [117]. The Adaptive Vertex Fitter utilizes an annealing

algorithm in which the outlier tracks are downweighted for each step, and thus exhibits good robustness against outlier tracks. In the AVF, the weight of a given track is defined as:

$$w_i(T) = \frac{\exp\left(-\chi_i^2/2T\right)}{\exp\left(-\chi_i^2/2T\right) + \exp\left(-\chi_c^2/2T\right)}, \tag{5.3}$$

where χ_c is a preset constant defining the threshold for track weight larger than 0.5 (in our case, χ_c is set to be 3.0); χ_i^2 measures the compatibility between the track and the vertex position:

$$\chi_i^2 = \frac{d^2(\text{track}_i, \mathbf{v})}{\sigma_i^2}, \tag{5.4}$$

where $d(\text{track}_i, \mathbf{v})$ is the three-dimensional distance between the track and the vertex position $\mathbf{v}$. The task of vertex reconstruction then becomes solving the following equation under a given "temperature" T:

$$\sum_i w_i(T, \mathbf{v})\chi_i(\mathbf{v})\nabla_{\mathbf{v}}\chi_i = 0. \tag{5.5}$$

This procedure is then repeated for several steps, with each step having a lower temperature till $T = 1$, which is called the *annealing schedule*. In this way, the outlier tracks are downweighted with each step, thus the vertex reconstruction can avoid dangerous local minima and become more robust.

A track is said to be assigned to the reconstructed vertex when the final weight of the track is larger than 0.5. The following vertex or track variables are examined to provide discriminating power between background and signal:

- Vertex invariant mass, where the kinematics of the vertex are determined by the four-momentum sum of the assigned tracks assuming pion mass for each track;
- Vertex p_{T};

- Track multiplicity of the vertex;
- L_{xy} significance, where L_{xy} is defined as the distance between secondary and primary vertices in the transverse plane;
- The transverse impact parameter significance of the track with the second highest $\mathrm{IP}_{\mathrm{2D}}$ significance among all the tracks assigned to the secondary vertex;
- The ratio between the sum of energy for all the tracks assigned to the vertex and the sum of the energy for all the tracks associated with the two jets:

$$\frac{\sum_{\mathrm{track}\in\mathrm{SV}} E_{\mathrm{track}}}{\sum_{\mathrm{track}\in\mathrm{dijet}} E_{\mathrm{track}}}. \tag{5.6}$$

The comparison between background and signal MC samples (with jet-jet model) for those variables are shown in Figures 5.2-5.7. For the events where more than one vertex is reconstructed, the one with the highest track multiplicity is selected. When the track multiplicities are also the same, the one with the smallest χ^2 per degree-of-freedom ($\chi^2/\mathrm{n_{dof}}$) is selected. For these plots, the signal MC samples are normalized such that the total number of events before trigger selection is 1×10^4, the QCD multijet MC sample is normalized such that the total number of events before trigger selection is 1×10^7.

In Figures 5.2-5.7, the results based on two different jet-track association algorithms are also plotted. The difference between the two algorithms is not significant with regard to the distributions of track and vertex variables. However, it was found that `JTA@CALO` was not well-defined for low p_{T} prompt tracks, therefore `JTA@VTX` is taken as the baseline algorithm of the analysis. All the following plots and results are based on `JTA@VTX` unless stated otherwise.

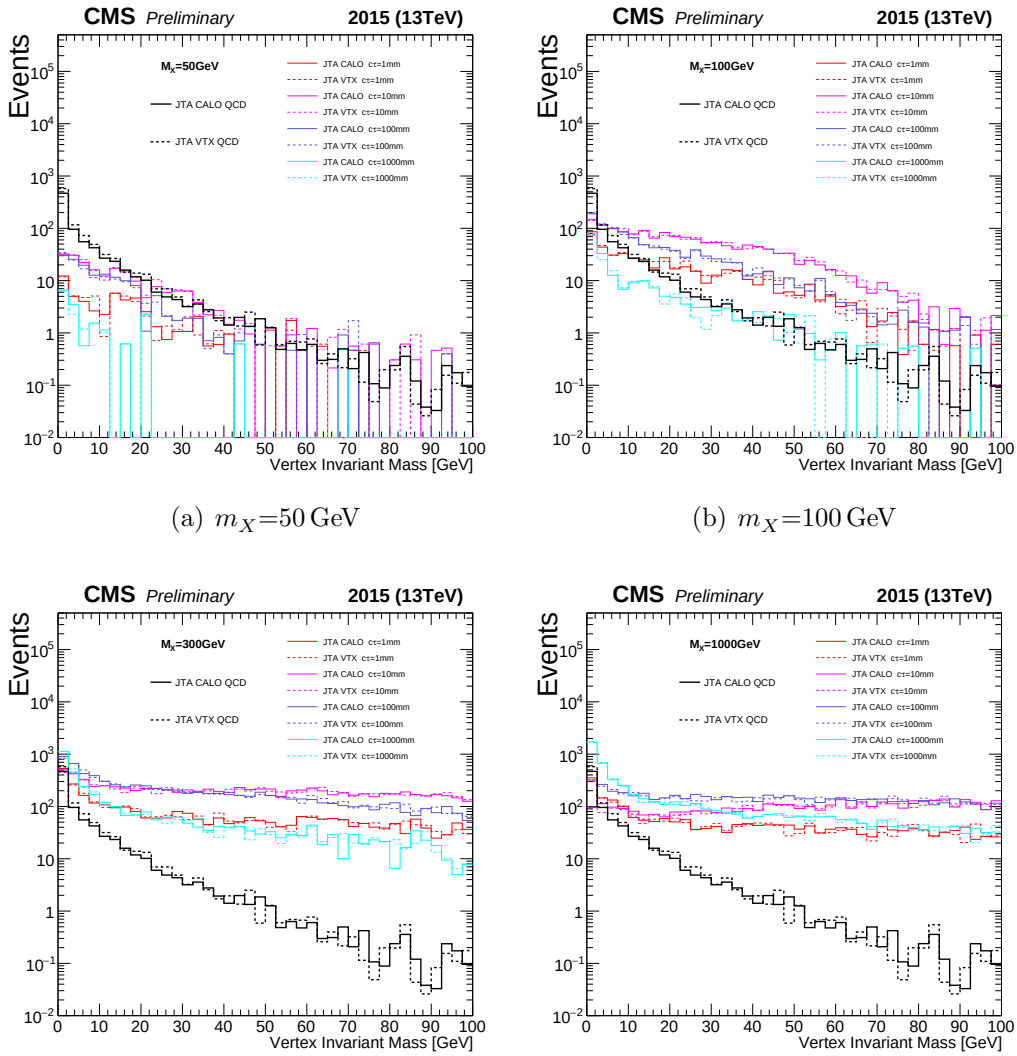

(a) m_X=50 GeV

(b) m_X=100 GeV

(c) m_X=300 GeV

(d) m_X=1000 GeV

Figure 5.2: The vertex invariant mass distributions for QCD multijet MC and jet-jet model signal MC samples. All samples are filtered by displaced dijet triggers matched by offline CALO H_{T} selection. Solid lines are results based on jet-track association at the calorimeter face, while the dashed lines are the results based on jet-track association at the vertex.

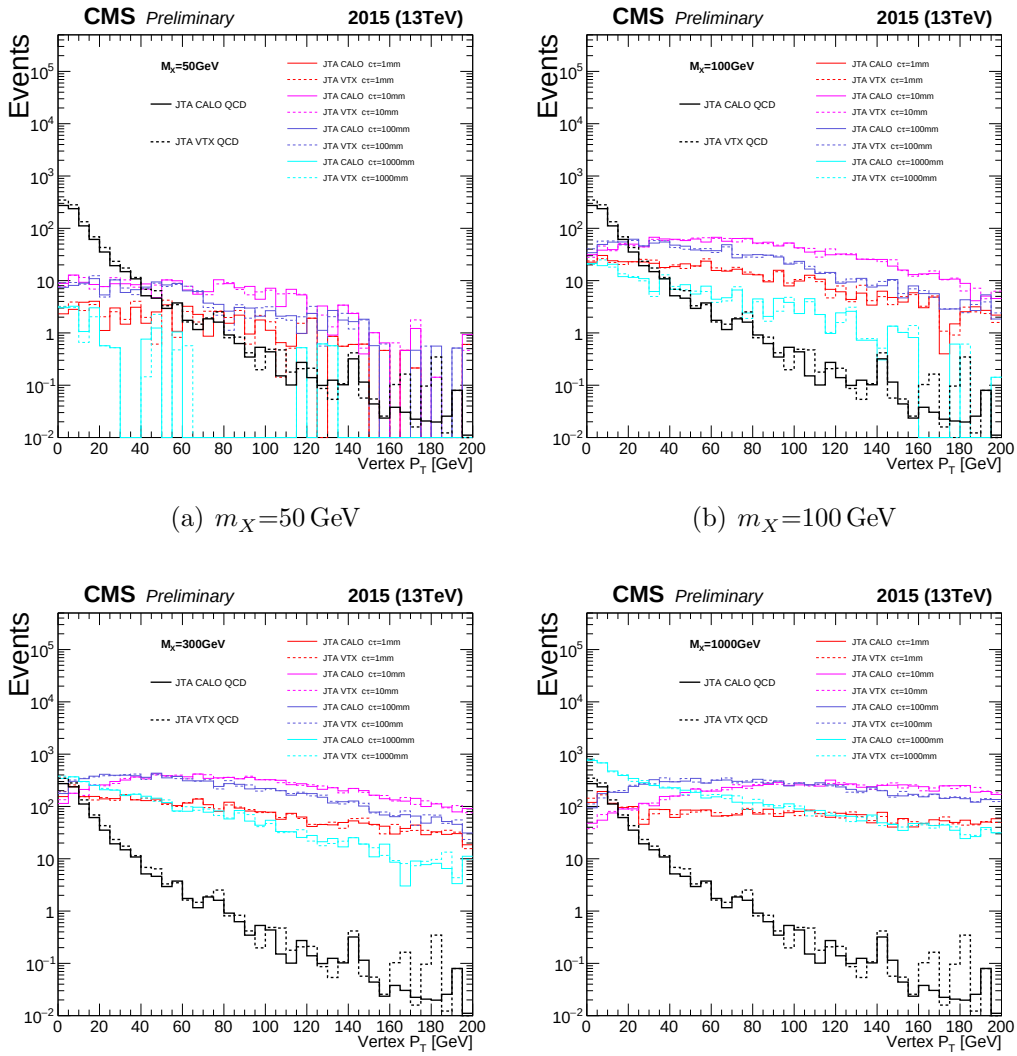

(a) m_X=50 GeV

(b) m_X=100 GeV

(c) m_X=300 GeV

(d) m_X=1000 GeV

Figure 5.3: The vertex transverse momentum distributions for QCD multijet MC and jet-jet model signal MC samples. All samples are filtered by displaced dijet triggers matched by offline CALO H_{T} selection. Solid lines are results based on jet-track association at the calorimeter face, while the dashed lines are the results based on jet-track association at the vertex.

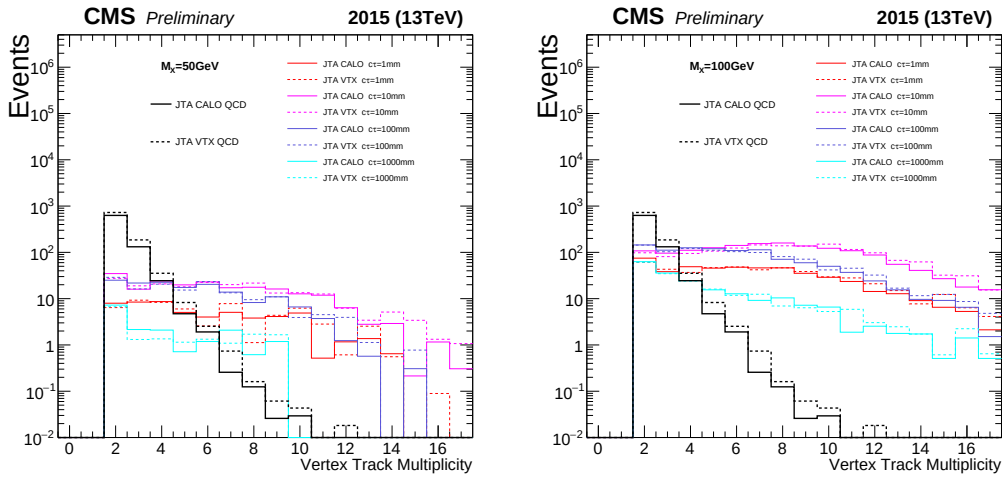

(a) m_X=50 GeV

(b) m_X=100 GeV

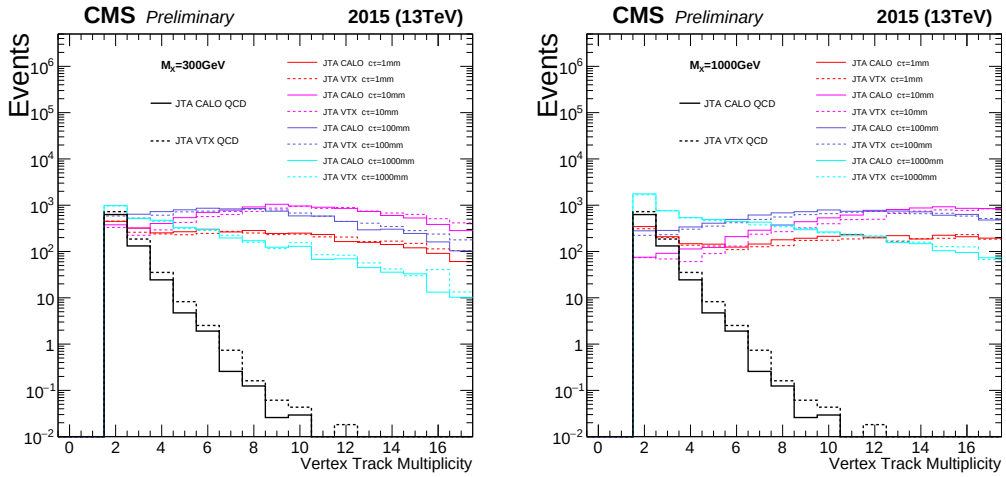

(c) m_X=300 GeV

(d) m_X=1000 GeV

Figure 5.4: The vertex track multiplicity distributions for QCD multijet MC and jet-jet model signal MC samples. All the samples are filtered by displaced dijet triggers matched by offline CALO H_{T} selection. Solid lines are results based on jet-track association at the calorimeter face, while the dashed lines are the results based on jet-track association at the vertex.

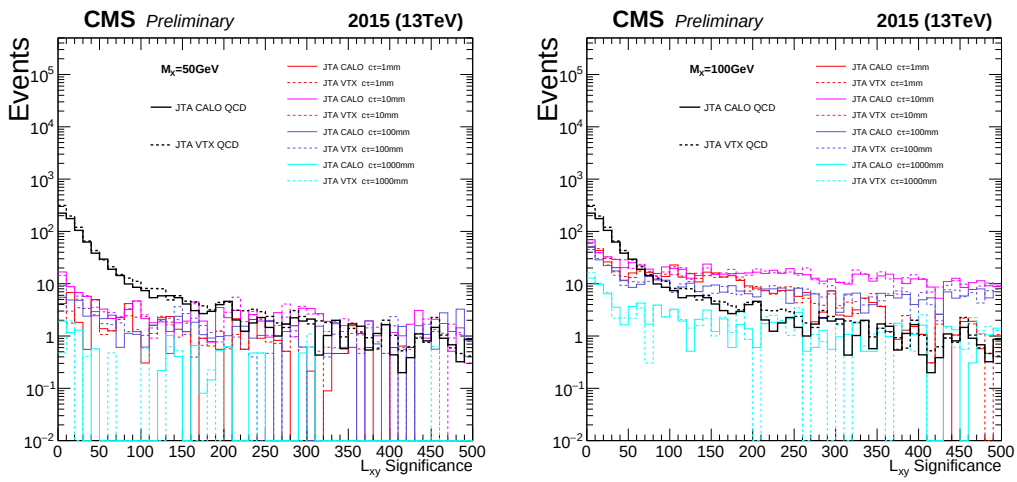

(a) m_X=50 GeV

(b) m_X=100 GeV

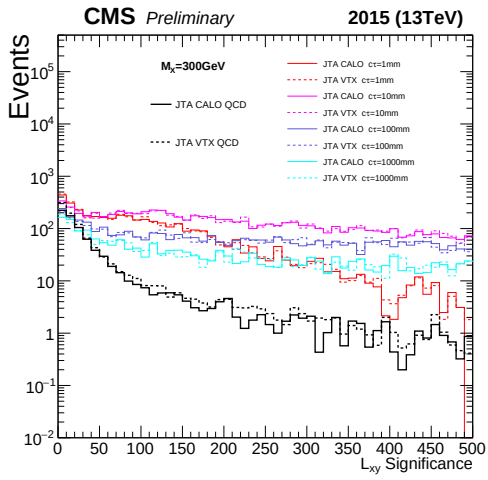

(c) m_X=300 GeV

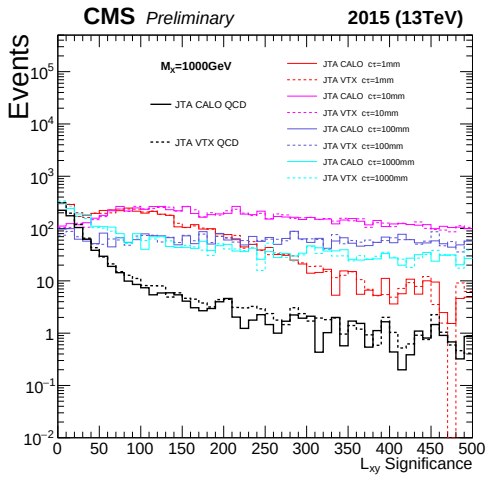

(d) m_X=1000 GeV

Figure 5.5: The L_{xy} significance distributions for QCD multijet MC and jet-jet model signal MC samples. All samples are filtered by displaced dijet triggers matched by offline CALO H_{T} selection. Solid lines are results based on jet-track association at calorimeter face, while the dashed lines are the results based on jet-track association at the vertex.

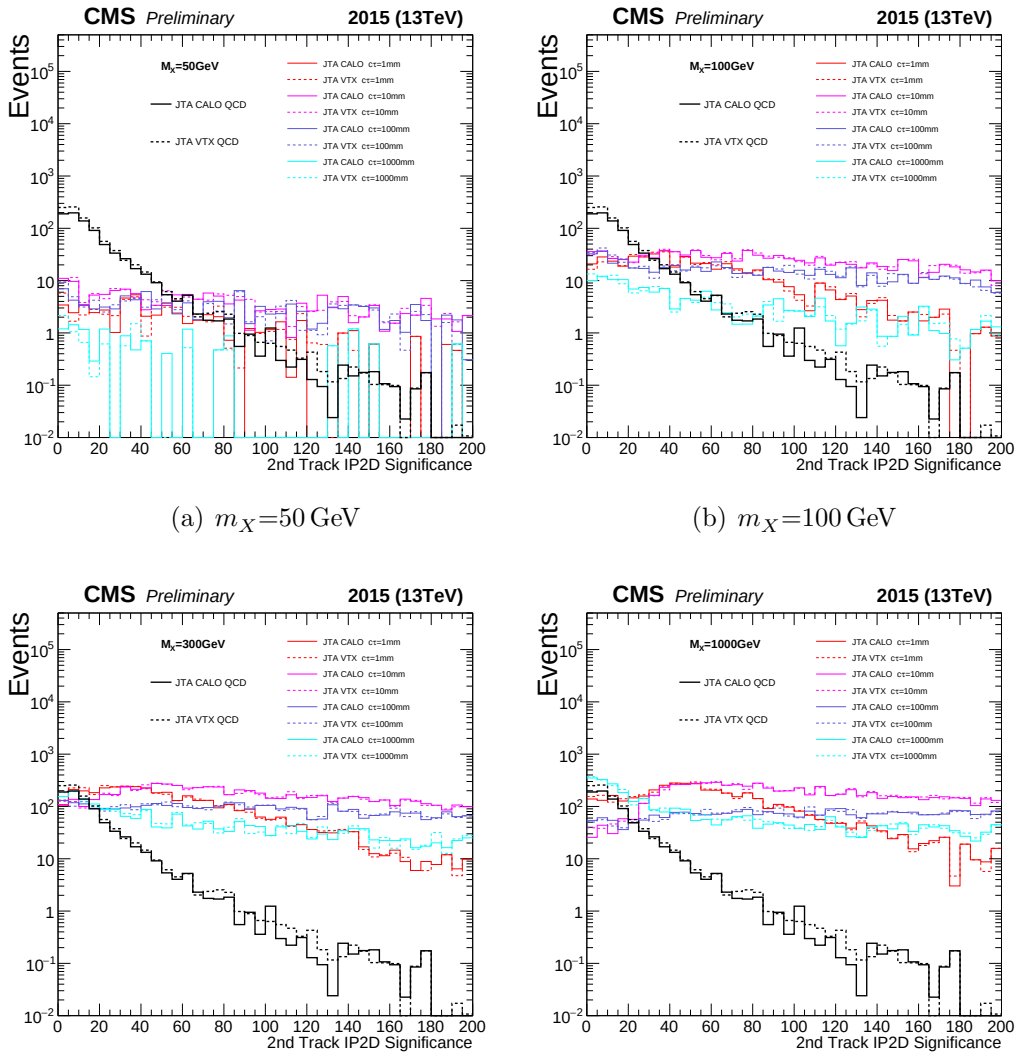

(a) m_X=50 GeV

(b) m_X=100 GeV

(c) m_X=300 GeV

(d) m_X=1000 GeV

Figure 5.6: The second highest track $\mathrm{IP}_{2\mathrm{D}}$ significance in the secondary vertex for QCD multijet MC and jet-jet model signal MC samples. All samples are filtered by displaced dijet triggers matched by offline CALO H_{T} selection. Solid lines are results based on jet-track association at calorimeter face, while the dashed lines are the results based on jet-track association at the vertex.

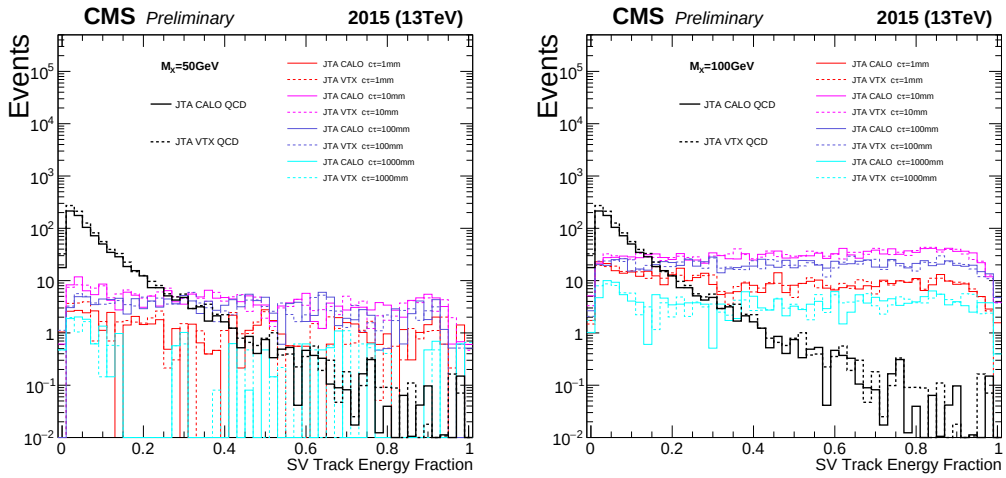

(a) m_X=50 GeV

(b) m_X=100 GeV

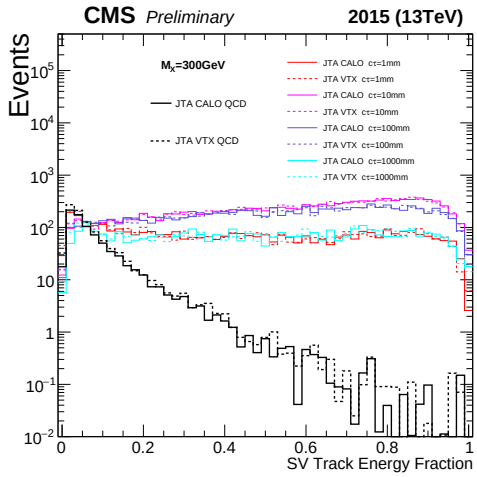

(c) m_X=300 GeV

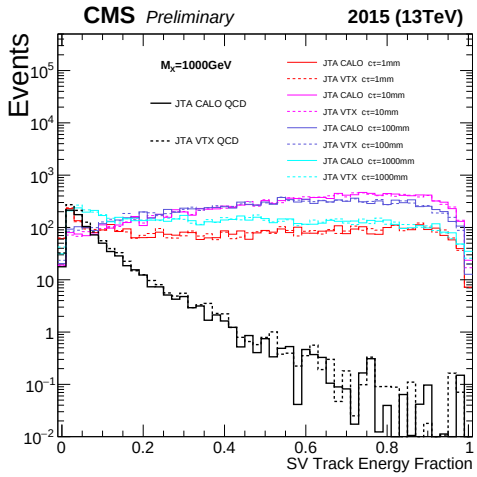

(d) m_X=1000 GeV

Figure 5.7: The secondary vertex track energy fraction with respect to the all tracks associated with the dijet for QCD multijet MC and jet-jet model signal MC samples. All samples are filtered by displaced dijet triggers matched by offline CALO H_{T} selection. Solid lines are results based on jet-track association at calorimeter face, while the dashed lines are the results based on jet-track association at the vertex.

As shown in Figures 5.2 and 5.3, since secondary vertices are mainly from the decay of long-lived particles for displaced jets, the secondary vertices in signals tend to have larger transverse momentum and invariant mass compared to QCD multijet background. However, when the mass of the long-lived particle goes down to 50 GeV, the discrimination between background and signal becomes less significant when it comes to the vertex invariant mass or transverse momentum.

Figure 5.4 shows the vertex track multiplicity for signal and background MC samples. In displaced jets, there tends to be higher track multiplicities in the reconstructed secondary vertices. Since the secondary vertices from QCD background usually come from nuclear interactions or accidentally crossed tracks, most vertices have only two assigned tracks.

Figures 5.5 and 5.6 show the L_{xy} significance and second-highest track $\mathrm{IP}_{\mathrm{2D}}$ significance for signal and background MC samples. For signal samples with displaced jet signatures, the secondary vertices tend to be more displaced in the transverse plane compared to the QCD background, therefore the secondary vertices in the signal samples tend to have higher L_{xy} significances and track $\mathrm{IP}_{\mathrm{2D}}$ significances.

Figure 5.7 shows the track energy fraction of the secondary vertex in the dijet system. For QCD multijet background, the total energy carried by the tracks assigned to the secondary vertex is small compared to the total track energy of the two jets, since the dijet doesn't really originate from the secondary vertex.

In the Run 1 displaced dijet analysis [118], it was required that there be at least

one track associated with each jet in the fitted secondary vertex. In Figure 5.8, we show the fraction of events that fail/pass this requirement in QCD background and signal samples. Overall, around 40% events in the QCD multijet background pass this requirement. Although most events in signals pass this requirement when m_X is large, only around 50% or less events pass the dijet requirement for the secondary vertex when $m_X = 50\,\mathrm{GeV}$. This is because when m_X is small, X tends to be highly boosted, and the two jets have a large probability to be merged and reconstructed as a single jet, thus it is hard to reconstruct a secondary vertex having tracks associated with two distinctive jets. In order to improve the sensitivity to the low mass region, we decided to remove this requirement from the analysis. In this way, we can also gain sensitivity to the case where the displaced vertex only contains one jet (as in the $\widetilde{\mathrm{g}} \to \mathrm{g}\widetilde{\mathrm{G}}$ model).

5.1.4 Preselection

We require the dijet (secondary vertex) candidates to fulfill certain preselection criteria to suppress the background. The first part of the preselection consists of the requirements for fit quality and kinematics of the secondary vertex:

- $\chi^2/\mathrm{n_{dof}}$ is smaller than 5.0;
- Vertex p_T is larger than $8\,\mathrm{GeV}$;
- Vertex invariant mass is larger than $4\,\mathrm{GeV}$;

The selections for vertex invariant mass and vertex p_T are imposed in order to suppress the background coming from long-lived mesons and baryons in the standard model. The data and QCD multijet MC distributions for these three variables before

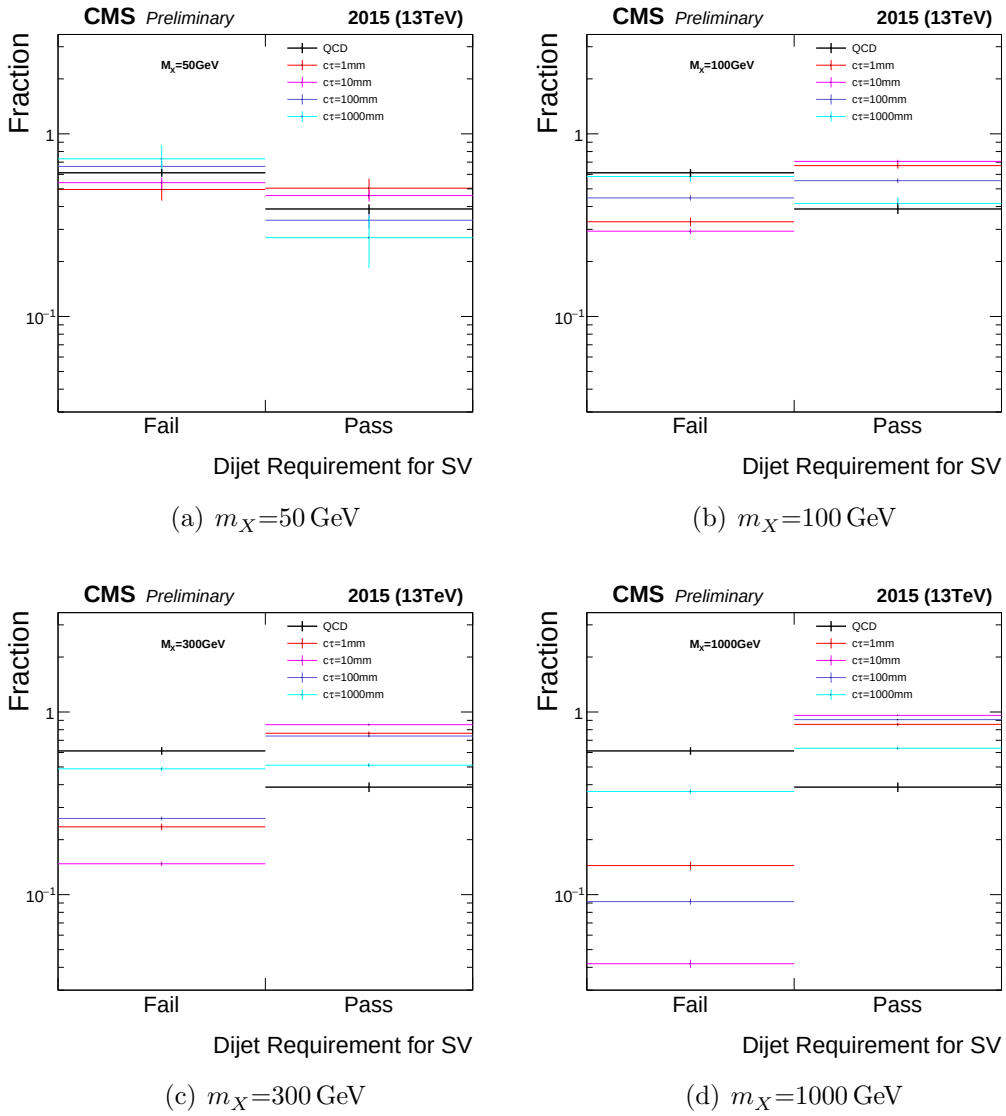

(a) m_X=50 GeV

(b) m_X=100 GeV

(c) m_X=300 GeV

(d) m_X=1000 GeV

Figure 5.8: The fraction of events that fail/pass the dijet requirement for QCD and signals, by which we require there is at least one track in each jet assigned to the secondary vertex. The tracks are associated with the jets on the calorimeter face.

preselection are shown in the top left, top right, and middle left plots of Figure 5.9; The distributions of signal MC samples at $m_X = 300\,\mathrm{GeV}$ are also plotted for comparison. In general, good agreement can be found between data and QCD multijet MC for the three variables.

The second part of the preselection is based on the transverse displacement and the energy carried by the tracks assigned to the secondary vertex. The secondary vertex track energy fraction and the second highest track $\mathrm{IP}_{2\mathrm{D}}$ significance before the preselection are shown in the middle right and bottom left plots of Figure 5.9, good agreements between data and QCD multijet MC samples can be found for both variables.

For the dijet (secondary vertex) candidates, we require that:

- Secondary vertex track energy fraction is larger than 15%;
- Second highest track $\mathrm{IP}_{2\mathrm{D}}$ significance is larger than 15.

Besides the vertex variables mentioned above, we also designed another variable to define the prompt activity contribution to the jets, which was also used in the preselection. For each track associated with the jets, the primary vertex (including the leading primary vertex and the pileup vertices) with the minimum 3D impact parameter ($\mathrm{IP}_{3\mathrm{D}}$) significance to the track is identified. If this minimum $\mathrm{IP}_{3\mathrm{D}}$ significance is smaller than 5, we assign the track to this primary vertex (in this way, we can find the tracks coming from the pileup vertices). Then for each jet, we can compute the track energy contribution from each primary vertex, and the primary vertex with the largest track energy contribution to the jet is chosen. We can now define a variable

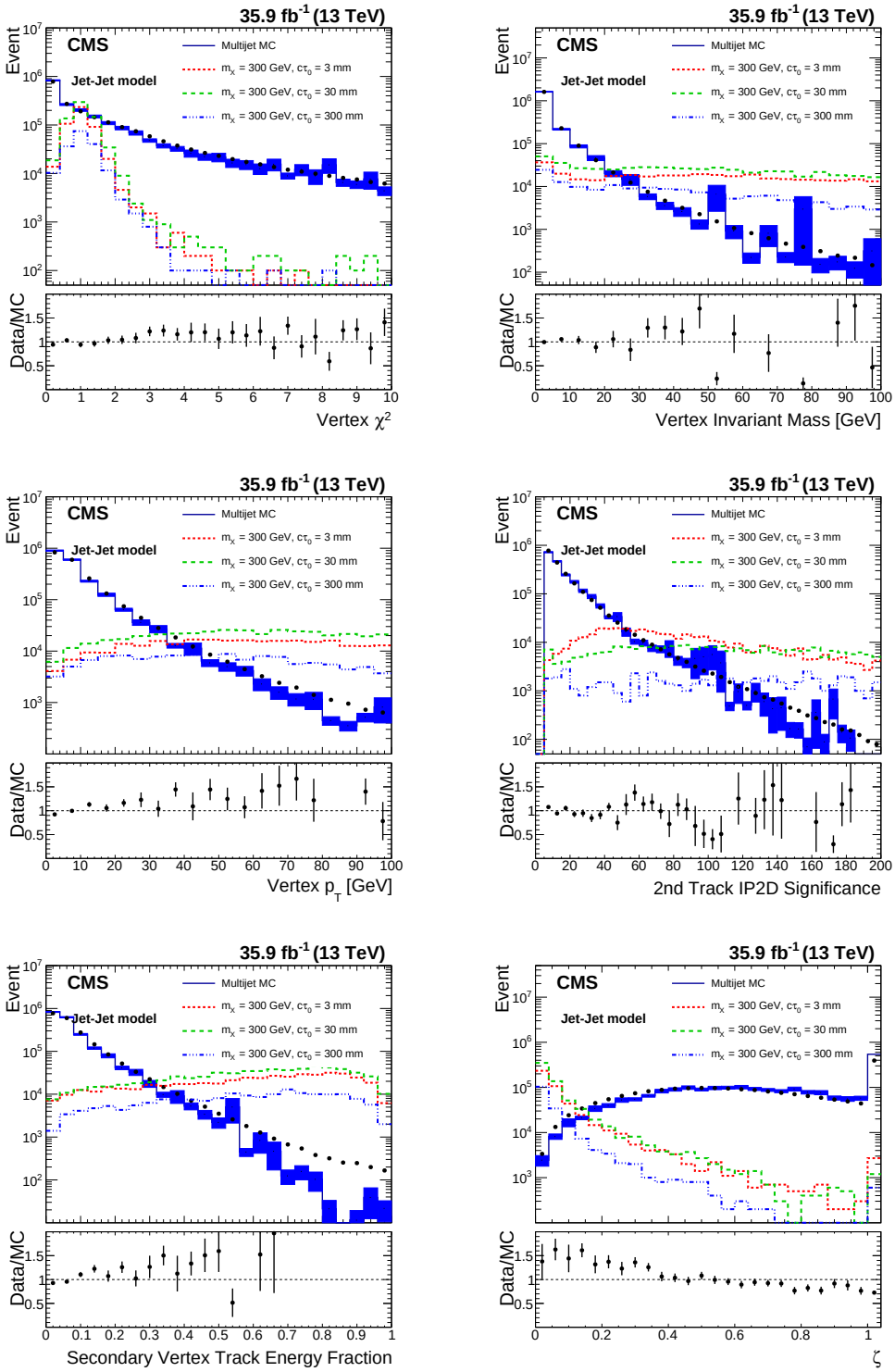

Figure 5.9: The distributions of preselection variables.

Table 5.1: Summary of the preselection criteria

Secondary-vertex/dijet variable	Requirement
Vertex $\chi^2/\mathrm{n_{dof}}$	<5.0
Vertex invariant mass	>4 GeV
Vertex transverse momentum	>8 GeV
Second largest two-dimensional IP significance	>15
Vertex track energy fraction in the dijet	>0.15
ζ (charged energy fraction associated with compatible primary vertices)	<0.20

ζ as:

$$\zeta = \frac{\sum_{\mathrm{track}\in\mathrm{PV}_1} E^{\mathrm{Jet}_1}_{\mathrm{track}} + \sum_{\mathrm{track}\in\mathrm{PV}_2} E^{\mathrm{Jet}_2}_{\mathrm{track}}}{E_{\mathrm{Jet}_1} + E_{\mathrm{Jet}_2}} \tag{5.7}$$

where PV_1 (PV_2) is the PV that has the largest track energy contribution to Jet_1 (Jet_2), and PV_1 doesn't need to be the same as PV_2. For the dijet (secondary vertex) candidates, we require that $\zeta < 0.2$.

The preselection criteria are summarized in Table 5.1. The selection efficiencies of the displaced dijet trigger (with offline CALO H_T match), vertex reconstruction and the two steps of preselection for background and signal MC samples are summarized in Table 5.2.

5.2 Event selection

In addition to the secondary vertex reconstruction based on the adaptive vertex fitter, an auxiliary algorithm is also explored in the analysis. For each displaced track associated with the dijet (i.e. the tracks satisfying $\mathrm{IP_{2D}} > 0.5\,\mathrm{mm}$, $\mathrm{Sig[IP_{2D}]} > 5.0$, $p_\mathrm{T} > 1\,\mathrm{GeV}$ and is *high-purity*), an expected decay point consistent with the displaced dijet hypothesis can be determined by the crossing point between the track helix and the dijet direction. When the track momentum is large, the track helix is

Table 5.2: Trigger efficiencies, vertex efficiencies, preselection efficiencies for QCD and jet-jet model signal MC samples. Event efficiencies in each row are relative to the events passing the criteria from rows above. Preselection 1 consists of the cuts on vertex $\chi^2/\mathrm{n_{dof}}$, p_T and invariant mass. Preselection 2 consists of the cuts on vertex track energy fraction, the second highest track $\mathrm{IP_{2D}}$ significance and ζ.

Efficiency (%)	QCD multijet	m_X=50 GeV			
		$c\tau_0 = 1\,\mathrm{mm}$	$c\tau_0 = 10\,\mathrm{mm}$	$c\tau_0 = 100\,\mathrm{mm}$	$c\tau_0 = 1\,\mathrm{m}$
Trigger	1.7×10^{-4}	0.47	1.62	0.56	0.06
Has vertex	81.1	97.2	97.3	97.6	94.4
Offline jet p_T	68.3	94.9	90.3	92.7	100
Preselection 1	12.5	67.7	81.0	71.7	47.1
Preselection 2	2.8	76.1	78.3	85.3	87.5

Efficiency (%)	m_X=100 GeV			
	$c\tau_0 = 1\,\mathrm{mm}$	$c\tau_0 = 10\,\mathrm{mm}$	$c\tau_0 = 100\,\mathrm{mm}$	$c\tau_0 = 1\,\mathrm{m}$
Trigger	3.11	10.3	4.91	0.5
Has vertex	99.0	99.3	98.7	98.0
Offline jet p_T	97.4	96.7	96.8	93.2
Preselection 1	83.0	89.4	80.6	74.6
Preselection 2	85.8	89.7	92.0	98.1

Efficiency (%)	m_X=300 GeV			
	$c\tau_0 = 1\,\mathrm{mm}$	$c\tau_0 = 10\,\mathrm{mm}$	$c\tau_0 = 100\,\mathrm{mm}$	$c\tau_0 = 1\,\mathrm{m}$
Trigger	18.9	69.0	42.4	6.27
Has vertex	99.6	99.8	99.5	96.6
Offline jet p_T	99.0	98.9	97.9	96.5
Preselection 1	87.8	95.5	92.8	86.0
Preselection 2	87.1	93.8	95.2	96.0

Efficiency (%)	m_X=1000 GeV			
	$c\tau_0 = 1\,\mathrm{mm}$	$c\tau_0 = 10\,\mathrm{mm}$	$c\tau_0 = 100\,\mathrm{mm}$	$c\tau_0 = 1\,\mathrm{m}$
Trigger	20.3	83.0	64.6	12.9
Has vertex	99.9	100	100	98.5
Offline jet p_T	99.8	99.9	99.7	99.0
Preselection 1	96.0	99.5	98.1	92.2
Preselection 2	92.6	97.7	97.2	97.0

approximately a straight line, the expected decay path length is:

$$L_{\mathrm{xy}}^{\mathrm{exp}} = \frac{\mathrm{IP}_{\mathrm{2D}}^{\mathrm{track}}}{\sin(\phi_{\mathrm{track}} - \phi_{\mathrm{dijet}})}, \tag{5.8}$$

where $\mathrm{IP}_{\mathrm{2D}}^{\mathrm{track}}$ is the signed transverse impact parameter for the track (the signature is determined by its angle with respect to the dijet direction), ϕ_{dijet} is the ϕ value of the dijet four-momentum (to compute the dijet four-momentum, the vertex of each CALO jet is updated from the primary vertex to the secondary vertex). Considering the curvature of the track helix in the magnetic field, the first order correction will be:

$$L_{\mathrm{xy}}^{\mathrm{exp}} = \frac{\mathrm{IP}_{\mathrm{2D}}^{\mathrm{track}}}{\sin(\phi_{\mathrm{track}} - \phi_{\mathrm{dijet}})} \left(1 - \frac{|\mathrm{IP}_{\mathrm{2D}}^{\mathrm{track}}|}{R}\right), \tag{5.9}$$

where R is the radius of curvature for the track helix in the transverse plane, and can be determined by the transverse momentum p_{T}, track charge q and the magnetic field B:

$$R = \frac{p_{\mathrm{T}}}{qB}. \tag{5.10}$$

After the expected decay path lengths are calculated, displaced tracks associated with the dijet are clustered based on $L_{\mathrm{xy}}^{\mathrm{exp}}$ using a *hierarchical clustering algorithm* [119]. In the *hierarchical clustering*, two clusters are merged together when the smallest $L_{\mathrm{xy}}^{\mathrm{exp}}$ difference between the two clusters is smaller than 15% of the vertex L_{xy}. When more than one clusters are formed after the final step of the hierarchical clustering, the one closest to the vertex L_{xy} is selected. Two variables of the cluster are examined to provide signal-background discrimination:

- Cluster track multiplicity;
- Cluster RMS:

$$\mathrm{RMS}_{\mathrm{cluster}} = \sqrt{1/N_{\mathrm{tracks}} \sum_{i=0}^{N_{\mathrm{tracks}}} \frac{(L_{\mathrm{xy}}^{\mathrm{exp}}(i) - L_{\mathrm{xy}})^2}{L_{\mathrm{xy}}^2}}. \tag{5.11}$$

The distributions of these two variables for data and MC samples are shown in Figure 5.10. Compared to the QCD background, the signals tend to have more tracks and smaller cluster RMS in the best cluster.

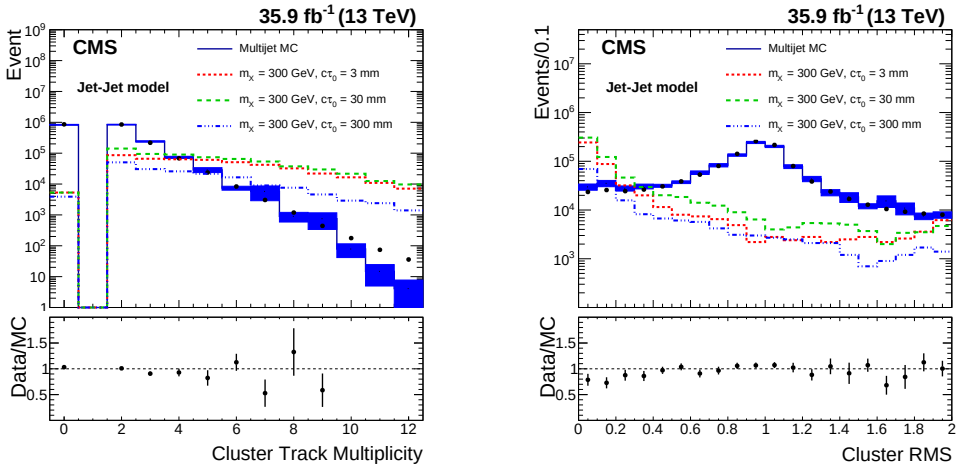

Figure 5.10: The distributions of cluster track multiplicity and cluster RMS for events collected by the displaced jet trigger. Offline CALO H_{T} selection and jet kinematics cuts were applied. The signal MC samples are normalized such that $\sigma \cdot 35.9\,\mathrm{fb}^{-1} = 1 \times 10^6$. The background samples are normalized to the corresponding luminosities in the data taking periods.

We then tried to build likelihood discriminant based on following variables:

- Vertex track multiplicity;
- Vertex L_{xy} significance;
- Cluster track multiplicity;
- Cluster RMS.

The distributions of vertex track multiplicity and vertex L_{xy} significance are shown in Figure 5.11. When the variables are uncorrelated, the likelihood discriminant is

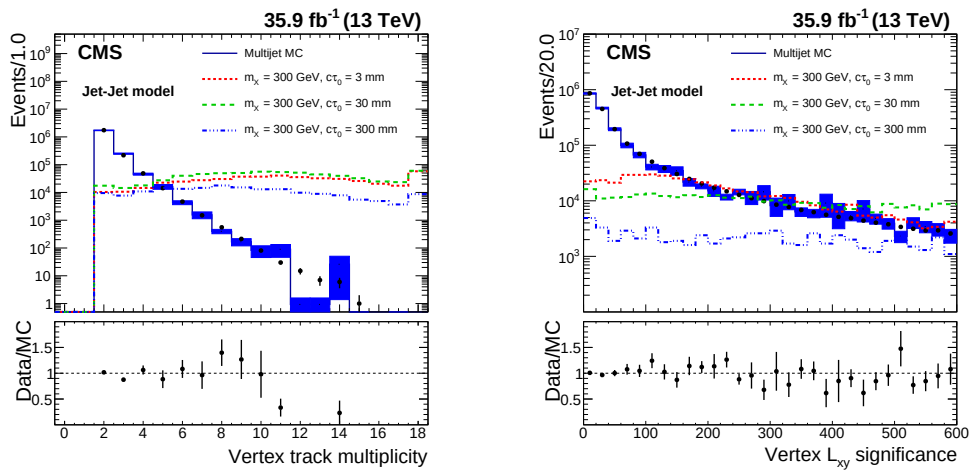

Figure 5.11: The distributions of vertex track multiplicity and L_{xy} significance for events collected by the displaced jet trigger. Offline CALO H_{T} selection and jet kinematics cuts were applied. The signal MC samples are normalized such that $\sigma \cdot 35.9\,\mathrm{fb}^{-1} = 1 \times 10^6$. The background samples are normalized to the corresponding luminosities in the data taking periods.

defined as:

$$p = \frac{p_S}{p_S + p_B} = \frac{1}{1 + p_B/p_S} = \frac{1}{1 + \prod_i p_{Bi}/p_{Si}} \tag{5.12}$$

where i is the label for different variables. When calculating p_B/p_S, we used the background and signal MC samples before preselection to increase the statistics, the jet-jet model events with $m_X = 300$ and $1000\,\mathrm{GeV}$, and with $c\tau_0 = 1$, 3, 10, 30, 100, 300, and $1000\,\mathrm{mm}$ are added together to derive p_S. However, cluster track multiplicity is correlated with vertex track multiplicity, with a correlation factor to be 0.497, where the correlation factor is defined as:

$$\mathrm{corr}(x, y) = \frac{\mathrm{cov}(x, y)}{\mathrm{RMS}(x)\mathrm{RMS}(y)}, \quad \mathrm{cov}(x, y) = \frac{\sum_i (x_i y_i)}{N} - \frac{\sum_i (x_i) \sum_j (y_j)}{N^2} \tag{5.13}$$

Therefore, we chose our likelihood discriminant to be built on vertex track multiplicity, cluster RMS and L_{xy} significance. The likelihood ratios for these three variables as well as the distributions of the likelihood discriminant in 2016 is shown in Figure 5.12.

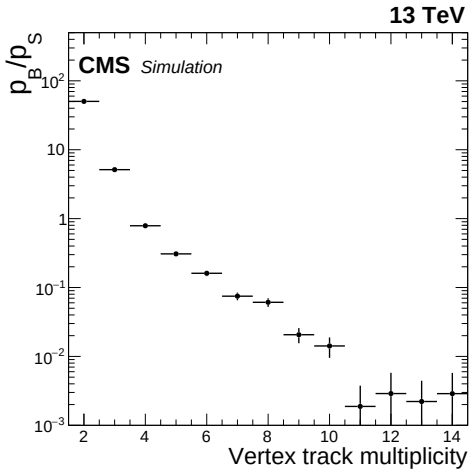

(a) p_B/p_S for vertex track multiplicity

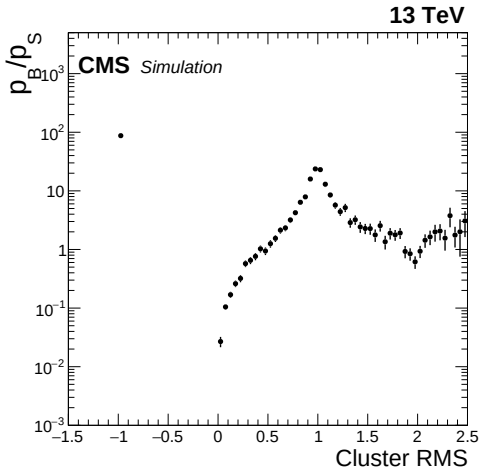

(b) p_B/p_S for cluster RMS

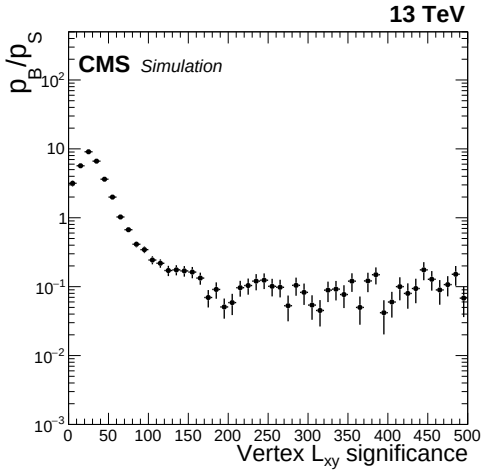

(c) p_B/p_S for L_{xy} significance

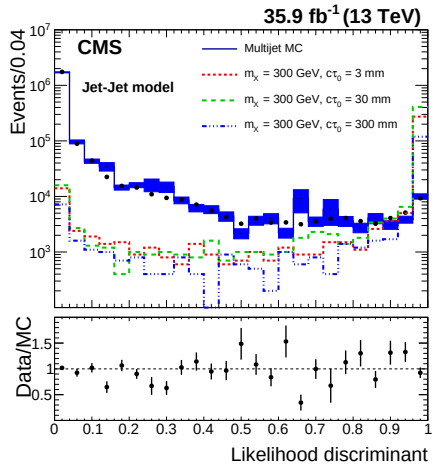

(d) Likelihood discriminant

Figure 5.12: (a)-(c): The likelihood ratio p_B/p_S for the discriminant variables; (d): The distributions of the likelihood discriminant for events collected by the displaced jet trigger. Offline CALO H_{T} selection and jet kinematics cuts were applied. The signal MC samples are normalized such that $\sigma \cdot 35.9\,\mathrm{fb}^{-1} = 1 \times 10^6$. The background samples are normalized to the corresponding luminosities in the data taking periods.

Apart from the likelihood discriminant, there are two other variables utilized in the final selection. One is the number of 3D prompt tracks in a single jet, where 3D prompt tracks are those tracks satisfying:

$$\mathrm{IP}_{3\mathrm{D}} < 300\mu m \tag{5.14}$$

The other is the jet energy fraction carried by 2D prompt tracks, where 2D prompt tracks are those tracks satisfying:

$$\mathrm{IP}_{2\mathrm{D}} < 500\mu m \tag{5.15}$$

The number of 3D prompt tracks and the charged prompt energy fraction for the first jet in the dijet are shown in Figures 5.13, where the displaced jets tend to have a smaller number of 3D prompt tracks and smaller charged prompt energy fraction.

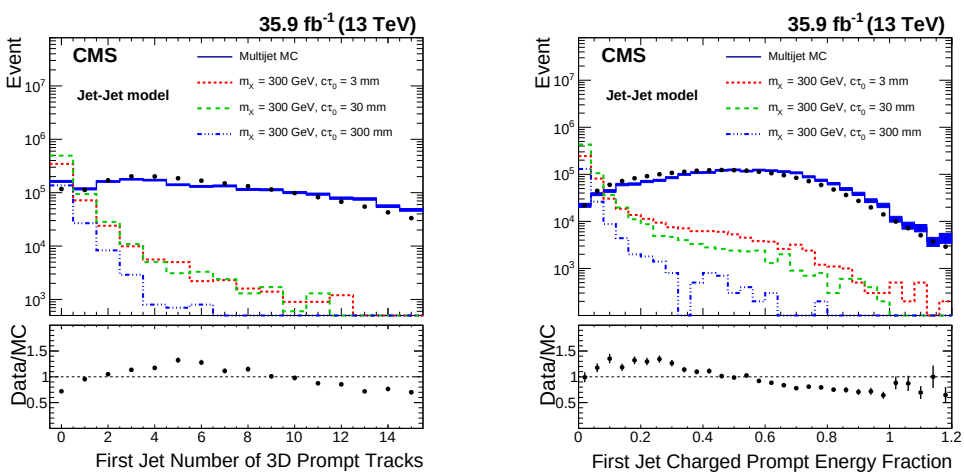

Figure 5.13: The distributions of the number of the 3D prompt tracks and the charged energy fraction for events collected by the displaced jet trigger. Offline CALO H_{T} selection and jet kinematics cuts were applied. The signal MC samples are normalized such that $\sigma \cdot 35.9\,\mathrm{fb}^{-1} = 1 \times 10^6$. The background samples are normalized to the corresponding luminosities in the data taking periods.

Chapter 6

Background Estimation

6.1 ABCD method

Due to the lack of statistics in the QCD MC sample, the prediction of background is derived from a data-driven method. In a simpler scenario, where we have two uncorrelated selection variables, one can estimate the background in the signal region with the so-called "ABCD method", where the region A, B, C, and D are defined as in Table 6.1. Region D is the signal region, in which both selections are passed, the number of events in region D can be estimated by:

$$D \approx \frac{BC}{A} \tag{6.1}$$

In our case, we have three separate selections, which are:

Table 6.1: The definition of the ABCD region

Region	Selection 1	Selection 2
A	Fail	Fail
B	Fail	Pass
C	Pass	Fail
D	Pass	Pass

- The selection on the number of 3D prompt tracks and the charged prompt energy fraction selection in the first jet;
- The selection on the number of 3D prompt tracks and the charged prompt energy fraction selection in the second jet;
- The selection on the likelihood discriminant.

Based on these three selections, we can build eight orthogonal regions, as shown in Table 6.2. In the eight regions, region H is the one where all the three selections are passed, and thus is the signal region. If the three selections are un-correlated, the number of events in region H can be estimated by:

1. FG/B
2. EG/C
3. EF/D
4. DG/A
5. BE/A
6. CF/A
7. BCD/A^2
8. $G(D + E + F)/(A + B + C)$
9. $G(D + E)/(A + C)$
10. $G(E + F)/(B + C)$
11. $G(D + F)/(A + B)$

Table 6.2: The definition of different regions used in background estimation

Region	Selection 1	Selection 2	Selection 3
A	Fail	Fail	Fail
B	Pass	Fail	Fail
C	Fail	Pass	Fail
D	Fail	Fail	Pass
E	Fail	Pass	Pass
F	Pass	Fail	Pass
G	Pass	Pass	Fail
H	Pass	Pass	Pass

Since there can be correlations between the two jet legs, to make our background prediction method more robust, we only used the last four variables. Specifically, $G(D+E+F)/(A+B+C)$ is treated as the central value of the predicted background, since it has the smallest statistical error, while the sub-combinations $G(D+E)/(A+C)$, $G(E+F)/(B+C)$, and $G(D+F)/(A+B)$ are used to estimate the systematic uncertainties of the background prediction. In order to validate the ABCD method in our analysis, we need to check the correlations among the three selections in the QCD background. We chose two working points for the jet variables cuts:

- Tight selection – number of prompt tracks is smaller than 2, charged prompt energy fraction is smaller than 15%;
- Loose selection – number of prompt tracks is smaller than 4, charged prompt energy fraction is smaller than 40%

We can calculate the correlation factors among the jet selections (at different working points) and likelihood discriminant as shown in Table 6.3. In general, the correlations among the three selections are small.

Table 6.3: The correlations between jet 1 selection, jet 2 selection and vertex-cluster likelihood discriminant after preselections

Correlation	Tight	Loose
Jet 1 selection v.s. Jet 2 selection	-0.0065	-0.0768
Jet 1 selection v.s. Likelihood discriminant	-0.0560	-0.0459
Jet 2 selection v.s. Likelihood discriminant	-0.0026	-0.0043

6.2 Background closure test with simulated QCD MC samples

To confirm the robustness of the background prediction method, we first tested it with simulated QCD multijet events within the two generator-level H_{T} bins $[300, 500]$ GeV and $[500, 700]$ GeV. The displaced jet trigger requirement was removed to improve the MC statistics. We then applied full offline selections on these events, and used the ABCD method to predict the background. The quantity $\mathrm{G(D+E+F)/(A+B+C)}$ is treated as the central value of the prediction (its statistical error is treated as the statistical error of the prediction), whereas the largest deviation from it to $\mathrm{G(D+E)/(A+C)}$, $\mathrm{G(E+F)/(B+C)}$ and $\mathrm{G(D+F)/(A+B)}$ is treated as the systematic error of the background prediction.

Figures 6.1 and 6.2 show the predicted and observed background yields for the two QCD multijet MC samples at tight/loose selection point, with different likelihood discriminant thresholds. We also calculated the *significance* for the deviation of the prediction, for which we assumed the number of observed background events obeys a Poisson distribution with a Gaussian prior:

$$P(n, \mu, \sigma) = \frac{1}{\sqrt{2\pi}\sigma} \int_0^\infty \exp\left[-\frac{(x-\mu)^2}{2\sigma^2}\right] \frac{x^n e^{-x}}{n!} dx \tag{6.2}$$

where n is the number of observed events, μ is the central value of the background prediction, σ is the systematic and statistical error added in quadrature. Note that the probability distribution $P(n, \mu, \sigma)$ is not unit normalized, since the integral over x is truncated at $x = 0$. Nevertheless, we can still define a properly normalized p-value as following:

$$p(n) = \sum_{k=0}^{n} P(k, \mu, \sigma) / \sum_{k=0}^{\infty} P(k, \mu, \sigma) \tag{6.3}$$

We then converted the p-value to a Z-value by using the error function:

$$Z = \sqrt{2}\,\mathrm{erf}^{-1}[2p - 1], \tag{6.4}$$

which represents the significance of the deviation in terms of the equivalent number of standard deviations. The numbers of predicted and observed background in the MC closure test, as well as the Z-values, are summarized in Table 6.4. In general, the observations are consistent with the predictions, and the significances of the deviations are small.

6.3 Background closure test in the control region

To test the background prediction with data, we defined a control region by inverting the secondary vertex track energy fraction cut, i.e. we required that the secondary vertex track energy fraction is less than 0.15. In this way the control region is populated with background events and is orthogonal to the signal region. The predicted and observed background for the control region with 2016 data at the loose selection point is shown in Figure 6.3 (for the tight selection, the statistics of 2016 data are insufficient in the control region, and the observed background is always zero). The values of predicted and observed background with different likelihood discriminant thresholds are summarized in Table 6.5, in which the observations are consistent with

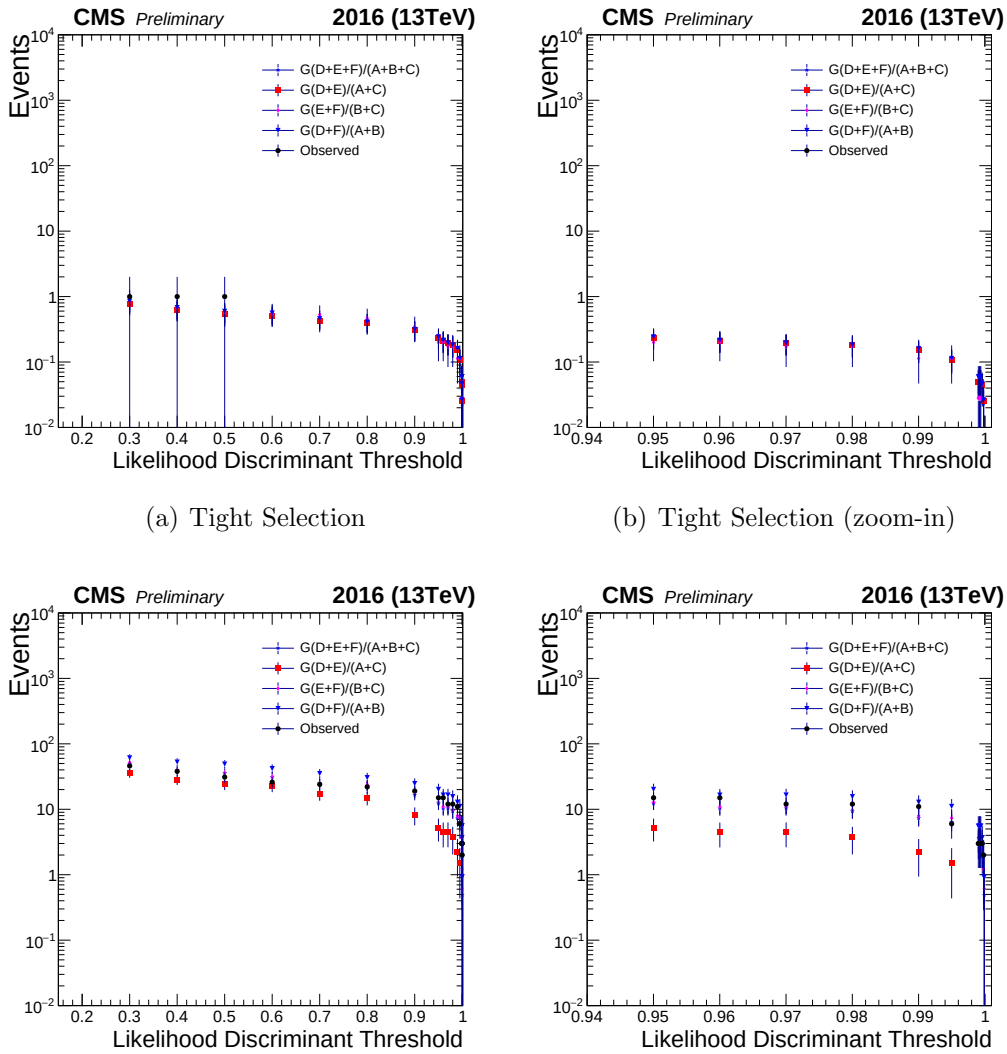

(a) Tight Selection

(b) Tight Selection (zoom-in)

(c) Loose Selection

(d) Loose Selection (zoom-in)

Figure 6.1: Closure test of the background prediction for QCD MC sample with generator $H_{\mathrm{T}} \in [300, 500]$ GeV. The top plots show the results with tight selection, the bottom plots show the results with loose selection. The right-hand plots are just the zoom-in of the left-hand plots in the range where the likelihood discriminant thresholds are larger than 0.94.

Table 6.4: The predicted and observed background in the QCD multijet MC closure test, the significances of the deviation are also shown in terms of the corresponding Z-values.

QCD $H_T \in [300, 500]$ GeV, tight selection			
Discriminant threshold	Predicted background	Observed background	Z-value
0.3	$0.82 \pm 0.10 \pm 0.27$	1	0.84
0.5	$0.56 \pm 0.03 \pm 0.19$	1	1.20
0.7	$0.45 \pm 0.08 \pm 0.15$	0	0.37
0.9	$0.31 \pm 0.03 \pm 0.10$	0	0.63
0.99	$0.15 \pm 0.04 \pm 0.05$	0	1.08
0.9992	$0.05 \pm 0.02 \pm 0.02$	0	1.62

QCD $H_T \in [300, 500]$ GeV, loose selection			
Discriminant threshold	Predicted background	Observed background	Z-value
0.3	$49.0 \pm 13.2 \pm 5.5$	46	-0.13
0.5	$35.7 \pm 13.4 \pm 4.6$	31	-0.26
0.7	$25.2 \pm 10.0 \pm 3.7$	24	-0.03
0.9	$16.7 \pm 8.5 \pm 3.0$	19	0.29
0.99	$7.35 \pm 5.5 \pm 1.93$	11	0.59
0.9992	$2.96 \pm 2.96 \pm 1.21$	3	0.05

QCD $H_T \in [500, 700]$ GeV, tight selection			
Discriminant threshold	Predicted background	Observed background	Z-value
0.3	$1.45 \pm 0.75 \pm 0.41$	3	1.27
0.5	$1.10 \pm 0.42 \pm 0.31$	3	1.73
0.7	$1.03 \pm 0.41 \pm 0.27$	1	0.57
0.9	$0.73 \pm 0.21 \pm 0.19$	0	-0.01
0.99	$0.33 \pm 0.15 \pm 0.09$	0	0.59
0.9992	$0.12 \pm 0.05 \pm 0.04$	0	1.19

QCD $H_T \in [500, 700]$ GeV, loose selection			
Discriminant threshold	Predicted background	Observed background	Z-value
0.3	$111.1 \pm 33.6 \pm 7.2$	91	-0.54
0.5	$86.5 \pm 28.9 \pm 6.11$	70	-0.51
0.7	$72.0 \pm 24.4 \pm 5.4$	55	-0.62
0.9	$46.6 \pm 18.8 \pm 4.2$	42	-0.19
0.99	$21.7 \pm 11.8 \pm 2.7$	18	-0.28
0.9992	$8.1 \pm 5.0 \pm 1.6$	7	-0.10

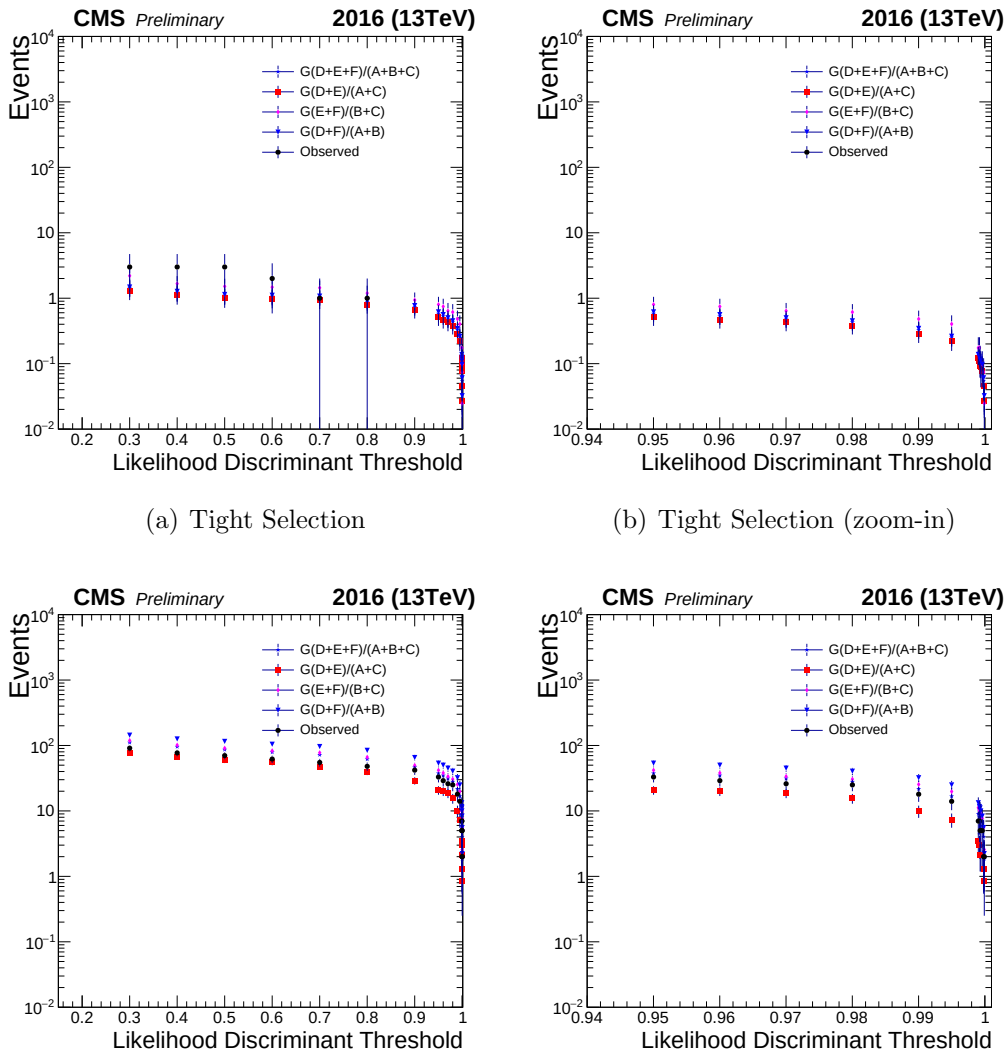

(a) Tight Selection

(b) Tight Selection (zoom-in)

(c) Loose Selection

(d) Loose Selection (zoom-in)

Figure 6.2: Closure test of the background prediction for QCD MC sample with generator $H_{\mathrm{T}} \in [500, 700]$ GeV. The top plots show the results with tight selection, the bottom plots show the results with loose selection. The right-hand plots are just the zoom-in of left-hand plots in the range where the likelihood discriminant thresholds are larger than 0.94.

the predictions.

The robustness of the background prediction method in the control region is also tested with QCD MC events. Figure 6.4, 6.5 show the predicted and observed back-

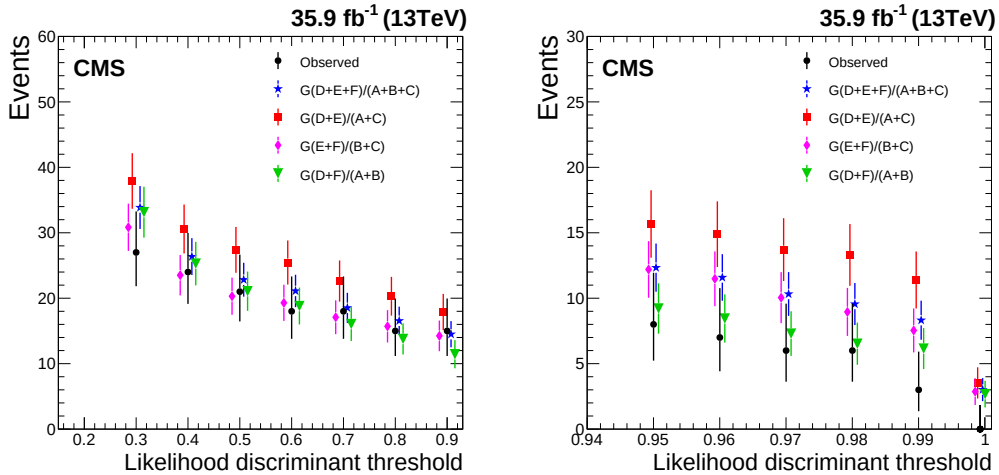

(a) Loose Selection

(b) Loose Selection (zoom-in)

Figure 6.3: Numbers of predicted and observed background events for the nominal background method and the three cross-checks in the control region. Shown are the comparisons for likelihood discriminant thresholds of 0.3, 0.4, 0.5, 0.6, 0.7, 0.8, and 0.9 (left); and for thresholds of 0.95, 0.96, 0.97, 0.98, 0.99, and 0.9993 (right). The error bars represent the statistical uncertainties of the predictions and the observations. The data points at different likelihood discriminant thresholds are correlated, since the events passing higher likelihood discriminant thresholds also pass lower likelihood discriminant thresholds.

ground levels for QCD MC samples at the loose selection point in the control region, good agreement can be found between the observations and the predictions.

6.4 Differential distribution estimation for the likelihood discriminants

In order to check the background prediction when the likelihood discriminant is small, we also established a method to predict the differential distribution of the likelihood discriminant, i.e. the background yield when the likelihood discriminant p satisfies $p \in (x_1, x_2]$ (i.e. $x_1 < p \leq x_2$). To achieve this, when constructing regions A

Table 6.5: The predicted and observed background in the control region for 2016 data. Good agreement can be found between the prediction and the observation

Discriminant threshold	Predicted background	Observed background	Z-value
0.3	$33.9 \pm 4.1 \pm 3.3$	27	-0.80
0.5	$22.8 \pm 4.6 \pm 2.6$	21	-0.14
0.7	$18.5 \pm 4.1 \pm 2.3$	18	0.05
0.9	$14.5 \pm 3.4 \pm 2.0$	15	0.24
0.99	$8.3 \pm 3.1 \pm 1.5$	3	-1.12
0.9992	$3.0 \pm 0.5 \pm 0.9$	0	-1.40

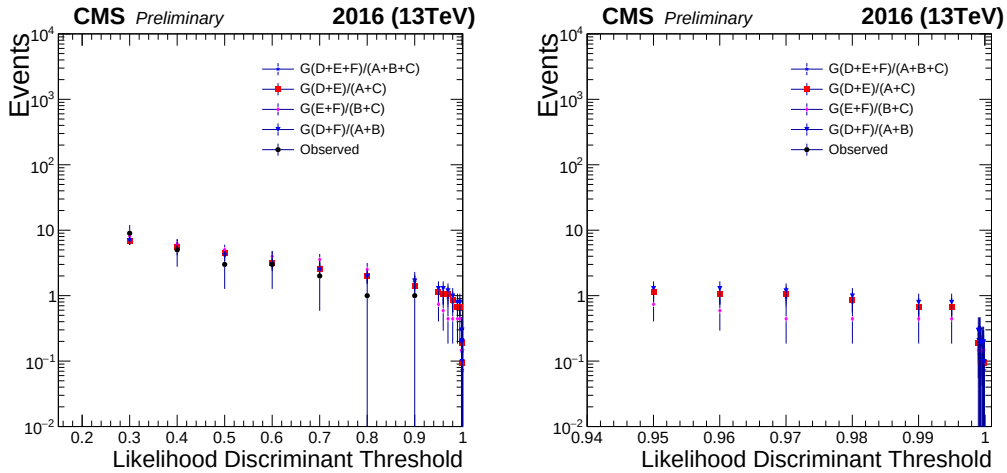

(a) loose selection

(b) loose selection (zoom-in)

Figure 6.4: Closure test of the background prediction in the control region for QCD MC sample with generator $H_{\mathrm{T}} \in [500, 700]$ GeV. Only the results at the loose selection point are shown, since the statistics are insufficient in the control region at the tight selection point.

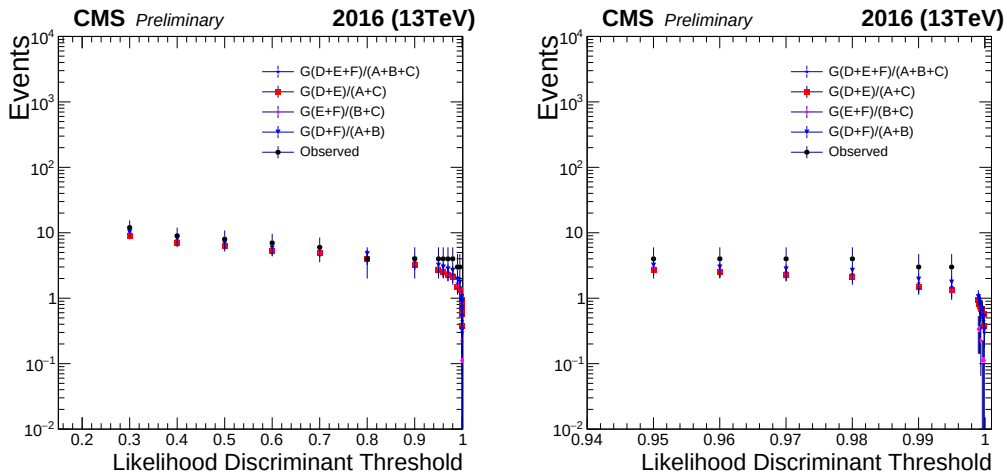

(a) loose selection

(b) loose selection (zoom-in)

Figure 6.5: Closure test of the background prediction in the control region for QCD MC sample with generator $H_{\mathrm{T}} \in [700, 1000]\,\mathrm{GeV}$. Only the results at the loose selection point are shown, since the statistics are insufficient in the control region at the tight selection point.

to H, we only select the events with $p \leq x_2$, the background in $p \in (x_1, x_2]$ can then be estimated by setting the last selection to be $p > x_1$ in the ABCD method described above. With this technique, we can check the consistency between the background prediction and the observation for small likelihood discriminant while still being blinded to the signal region (i.e. large likelihood discriminant). Figure 6.6 shows the differential distributions of the predicted background and observed events at small likelihood region for different selection values and different jet-track association algorithms. `JTA@VTX` generally leads to better agreement between predictions and observations than `JTA@CALO`. The main difference between `JTA@VTX` and `JTA@CALO` lies in low p_{T} tracks, which would be strongly bent in the magnetic field. Therefore the `JTA@CALO` is not well-defined for low p_{T} prompt tracks, and `JTA@VTX` is taken as the baseline jet-track association algorithm for this analysis instead.

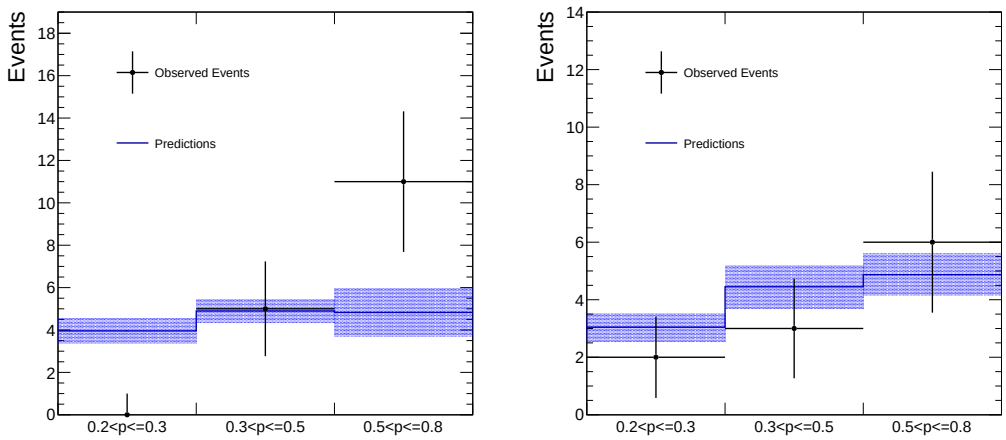

(a) α=0.21, β=0.13, JTA@CALO

(b) α=0.21, β=0.13, JTA@VTX

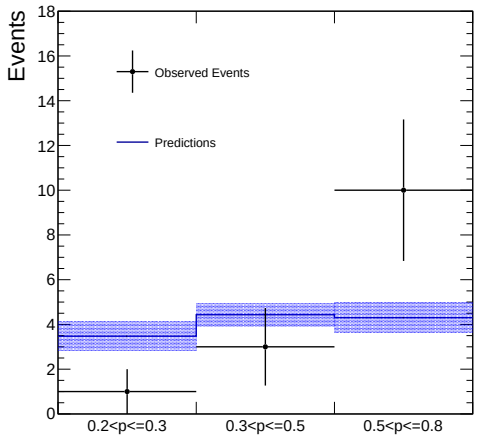

(c) α=0.15, β=0.14, JTA@CALO

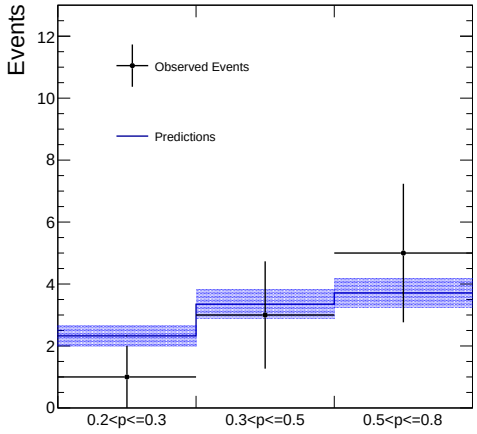

(d) α=0.15, β=0.14, JTA@VTX

Figure 6.6: The differential distributions of the predicted background and observed events at small likelihood region; Here α is the numerical value of the cut on the first jet charged prompt energy fraction, and β is the numerical value of the same cut on the second jet.

6.5 Selection optimization

In order to optimize the final selection, we parameterize the final cuts as following:

- Charged prompt energy fraction $< \alpha$ for the first jet;
- Charged prompt energy fraction $< \beta$ for the second jet;
- Vertex likelihood discriminant $> \gamma$.

Since the predicted background is expected to be very small in our analysis, the usual target function for optimization $S/\sqrt{B}$ (or $S/\sqrt{S+B}$ when one considers optimizing the discovery potential) doesn't hold here, and the minimization usually doesn't converge. We instead used Punzi formula with 5σ significance [120] by maximizing the target function:

$$F(\alpha, \beta, \gamma) = \sum_{S_i} \log \left[\frac{\epsilon_{S_i}(\alpha, \beta, \gamma)}{5/2 + \sqrt{B(\alpha, \beta, \gamma)}} \right] \tag{6.5}$$

where S_i represents different signal points, B is the predicted background level using ABCD method. For optimization we choose 12 signal points with m_X=100, 300, 1000 GeV and $c\tau_0$ = 1, 10, 100, 1000 mm. We then look for the maximization point of $F(\alpha, \beta, \gamma)$ in the three-dimensional space of (α, β, γ), and we get (α, β, γ)=(0.15, 0.13, 0.9993), which is chosen as our optimized final selection.

Chapter 7

Systematic Uncertainties

7.1 Trigger Systematics

In the analysis we used specialized trigger paths for capturing the displaced jet signatures. Our main signal path `HLT_HT350_DisplacedDijet40_DisplacedTrack_v` has the following HLT workflow composed of a series of HLT filters:

- `hltHT350`→`hltDoubleCentralCaloJetpt40`→ `hltL4PromptDisplacedDijetFullTracksHLTCaloJetTagFilterLowPt`→ `hltL4DisplacedDijetFullTracksHLTCaloJetTagFilterLowPt`

where the requirements for each HLT filter are:

- `hltHT350`: Online CALO H_{T} >350 GeV;
- `hltDoubleCentralCaloJetpt40`: At least two online CALO jets satisfying p_{T} larger than 40 GeV and $|\eta| < 2.0$;
- `hltL4PromptDisplacedDijetFullTracksHLTCaloJetTagFilterLowPt`: At least two online CALO jets (tagged by the above CALO Jet filter) having no more

than two online prompt tracks, where the prompt tracks are defined as $\mathrm{IP}_{2\mathrm{D}} < 1\,\mathrm{mm}$, and the track candidates are selected from the three iterations (`iter0`, `iter1`, `iter2`) of HLT online tracking;

- `hltL4DisplacedDijetFullTracksHLTCaloJetTagFilterLowPt`: At least two online CALO jets (tagged by the above CALO Jet filters) having at least one online displaced track, where the displaced tracks are defined as $\mathrm{IP}_{2\mathrm{D}} > 0.5\,\mathrm{mm}$ and $\mathrm{Sig}[\mathrm{IP}_{2\mathrm{D}}] > 5.0$, the track candidates are selected from the four iterations (`iter0`, `iter1`, `iter2`, `iter4`) of HLT online tracking.

In order to study the overall performance of the signal path, we ran the Physics Analysis Tool (PAT) sequence to get access to the bits and trigger objects (i.e. the tagged online CALO jets) of each HLT filter. We then studied the performance of each HLT filter separately, which will be explained in detail in the following sections.

7.1.1 Online CALO H_{T} filter

To study the performance of the CALO H_{T} filter `hltHT350`, we utilized the orthogonal primary data sets `/SingleMuon/*/AOD` and selected the events triggered by the isolated single muon path `HLT_IsoMu24_v`. We then computed the efficiency of `hltHT350` as a function of offline CALO H_{T} as shown in Figure 7.1, where the efficiency is defined as:

$$\epsilon = \frac{N_{\mathrm{events}}(\mathrm{HLT\_IsoMu24\_v\ AND\ hltHT350})}{N_{\mathrm{events}}(\mathrm{HLT\_IsoMu24\_v})} \tag{7.1}$$

In 2016, before Run2016H, `hltHT350` became fully efficient when offline CALO H_{T} is larger than 400 GeV. However, in Run2016H, due to the saturation of L1 jets, the L1 HTT seeds become inefficient when going to higher H_{T}, this further impacts the efficiency of the HLT CALO H_{T} filter. The loss of efficiency can be observed in the

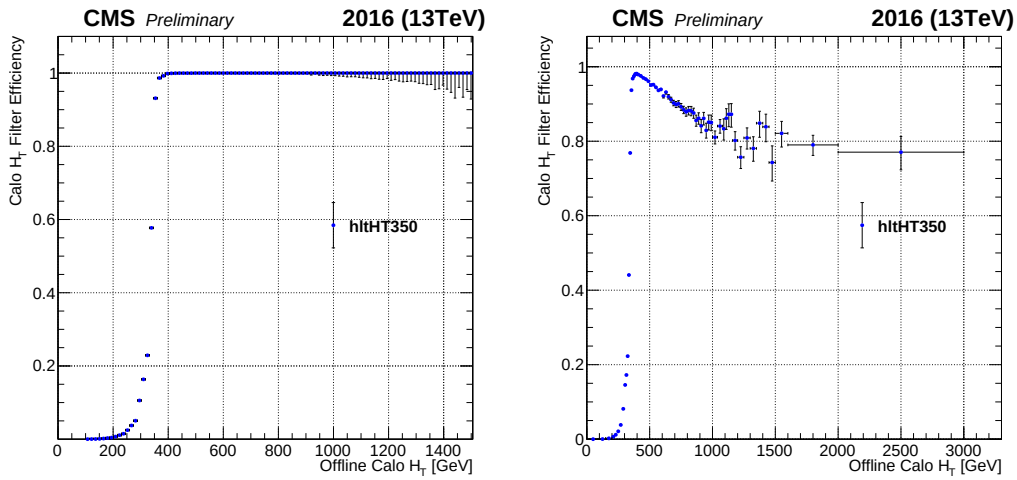

(a) Before Run2016H data-taking period (b) Within Run2106H data-taking period

Figure 7.1: The efficiency of the CALO H_{T} filter `hltHT350` as a function of offline CALO H_{T} in different data taking periods. Left: the efficiency measured before Run2016H; Right: the efficiency measured during Run2016H, where L1_HTT seed became inefficient due to saturated L1 jets.

right plot of Figure 7.1, and can be as large as $\sim 20\%$ when $H_{\mathrm{T}} > 1000\,\mathrm{GeV}$. To estimate the impact of the L1 HTT inefficiency on the signal acceptance, we fit the efficiency curve of `hltHT350` for CALO $H_{\mathrm{T}} > 400\,\mathrm{GeV}$ in Run2016H (with a linear function for $H_{\mathrm{T}} \in [400, 1200]\,\mathrm{GeV}$, and a constant term for $H_{\mathrm{T}} > 1200\,\mathrm{GeV}$), and apply it to the signal MC samples according to offline CALO H_{T}. We then apply the full offline selection again, and compare the signal efficiencies with the original values. The inefficiencies for different signal points are listed in Table 7.1. The loss of signal yields in the entire 2016 dataset can be obtained by multiplying the inefficiency by 0.241, which is the luminosity ratio of Run2016H to the entire 2016 dataset (the largest loss of signal yield would be $\sim 4.8\%$). The corrections are then applied to the signal yields, half of the corrections are taken as the systematic errors.

Table 7.1: The variations of signal efficiencies (for jet-jet model)due to the inefficiency of L1 HTT seed in Run2016H.

Variations	$c\tau_0 = 1\,\mathrm{mm}$	$c\tau_0 = 10\,\mathrm{mm}$	$c\tau_0 = 100\,\mathrm{mm}$	$c\tau_0 = 1000\,\mathrm{mm}$
$m_X = 1000\,\mathrm{GeV}$	20.0%	20.0%	20.0%	19.8%
$m_X = 700\,\mathrm{GeV}$	20.0%	19.7%	19.5%	19.2%
$m_X = 500\,\mathrm{GeV}$	18.5%	17.8%	17.6%	16.9%
$m_X = 300\,\mathrm{GeV}$	12.8%	12.1%	11.7%	10.9%
$m_X = 100\,\mathrm{GeV}$	6.6%	6.6%	6.6%	6.6%
$m_X = 50\,\mathrm{GeV}$	5.5%	5.3%	3.9%	6.1%

7.1.2 Online CALO jet p_{T} filter

To study the performance of the online CALO jet p_{T} (and η) filter:

`hltDoubleCentralCaloJetpt40`,

we selected the events collected with the prescaled control path `HLT_HT325_v` and required offline CALO $H_{\mathrm{T}} > 400\,\mathrm{GeV}$. After matching the offline CALO jets with online CALO jets by requiring $\Delta R < 0.4$, we measured the per-jet tag efficiency for the online CALO jet filter as a function of the offline p_{T}, which is shown in Figure 7.2. When offline $p_{\mathrm{T}} > 50\,\mathrm{GeV}$, both data and MC simulation reach full efficiency, and the difference between them is negligible. Therefore no further systematic uncertainties are added.

7.1.3 Online tracking requirements

To study the performance of the online prompt/displaced tracking requirements, we selected the events triggered by the prescaled control path `HLT_HT325_v`, and then required that `hltHT350` and `hltDoubleCentralCaloJetpt40` were fired. The online CALO jets satisfying $p_{\mathrm{T}} > 40\,\mathrm{GeV}$, $|\eta| < 2.0$ are required to match offline CALO jets with $\Delta R < 0.4$. For the offline CALO jets, we ran the jet-track association algorithm through which we matched the offline tracks to the jets at the primary vertex with

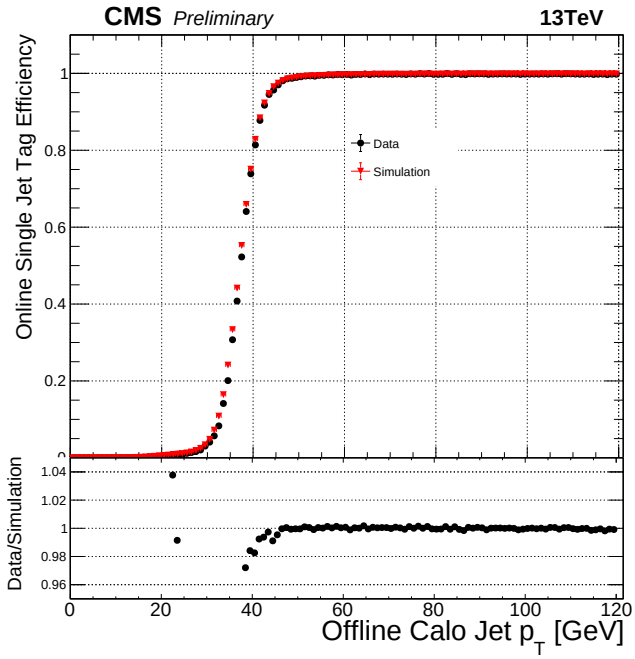

Figure 7.2: The online tag efficiency for offline CALO jets satisfying online p_{T} >40 GeV, online $|\eta| < 2.0$. Offline selection $|\eta| < 2.0$ is applied to the jets.

cone size equal to 0.4, and the number of offline prompt tracks and displaced tracks for offline jets are computed using the same definition as in the online computation. We further required the offline CALO jets satisfying $p_{\mathrm{T}} > 50\,\mathrm{GeV}$, $|\eta| < 2.0$ and offline CALO $H_{\mathrm{T}} > 400\,\mathrm{GeV}$ to make sure the measurement is done at the plateaus of the CALO H_{T} filter and the CALO jet p_{T} filter. The per-jet online tag efficiencies for prompt track requirement are then computed as functions of offline prompt track multiplicity. To compute the efficiency of the online displaced track requirement, in addition to the selections mentioned above, we required the events having at least two jets containing no more than two online prompt tracks, and only selected the jets tagged by the online prompt track requirement. The efficiencies of the online displaced track requirement are then computed as functions of the number of offline displaced tracks. The measurements of jet tag efficiencies for online prompt/displaced track

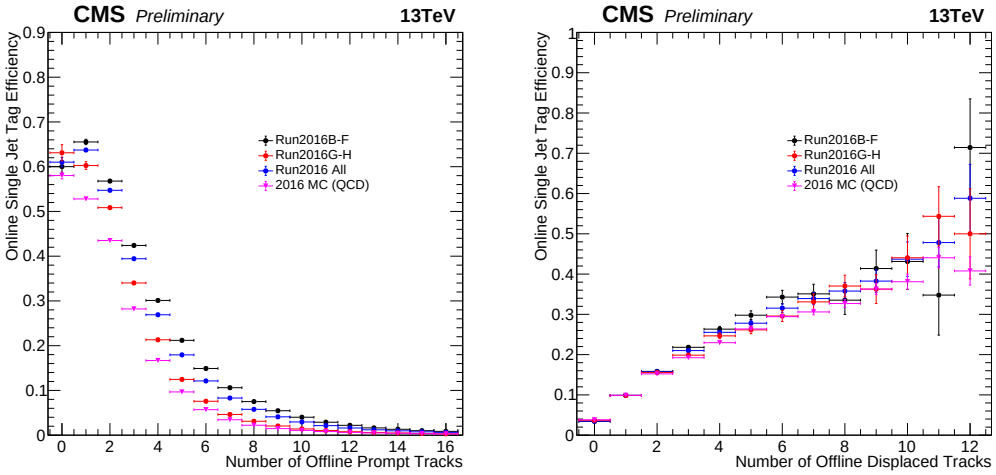

(a) Online prompt track Requirement (b) Online displaced track Requirement

Figure 7.3: The online per-jet tag efficiency for the CALO jets as functions of offline prompt tracks/displaced tracks in the 2016 data-taking periods. The offline CALO jets are required to have $p_{\mathrm{T}} > 50\,\mathrm{GeV}$ and $|\eta| < 2.0$. The efficiencies calculated with QCD MC samples are also plotted for comparison.

requirements are shown in Figure 7.3. For the online displaced track requirement, MC simulation is consistent with the data performance across the whole 2016 data taking period, and the differences are generally within the statistical uncertainties. Meanwhile for the online prompt track requirement, the tag efficiencies in real data are constantly higher than the efficiencies measured with MC simulation. Moreover, Run2016B-F has higher efficiencies than Run2016G-H due to the loss of tracks in online tracking when affected by the APV saturation issue (and given the fact we cut on the **maximum** number of prompt tracks). Since data always has higher efficiency compared to the QCD multijet MC simulation, in order to be conservative no further correction is applied to the signal acceptance. To estimate the systematic uncertainty of the online tracking, we interpret the difference between data and MC as the overestimation of mistag efficiency in the MC simulation. We then define a

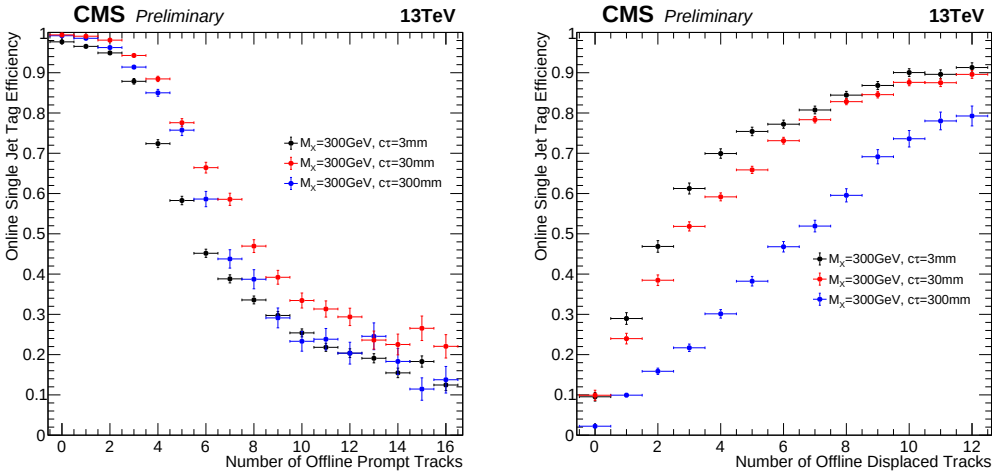

(a) Online prompt track requirement (b) Online displaced track requirement

Figure 7.4: The online per-jet tag efficiency for the CALO jets as functions of offline prompt tracks/displaced tracks for displaced jets MC samples at $m_X = 300\,\text{GeV}$. The offline CALO jets are required to have $p_\text{T} > 50\,\text{GeV}$ and $|\eta| < 2.0$.

scale factor as following:

$$SF(N_\text{p.track}) = \frac{1 - \epsilon_\text{data}(N_\text{p.track})}{1 - \epsilon_\text{MC}(N_\text{p.track})} \tag{7.2}$$

where $N_\text{p.track}$ is the number of offline prompt tracks, and ϵ is the single jet tag efficiency. We then reprocess the signal MC samples. In the signal MC all the CALO jets satisfying online p_T >40 GeV, online $|\eta|$ <2.0 can be divided into two categories based on whether they are tagged by the online prompt track requirement or not. When the jet is untagged, we generate a random number from a uniform distribution $r \in [0, 1]$. If $r > SF(N_\text{p.track})$ this untagged jet is updated to be tagged. We then recompute the efficiencies of having at least two tagged jets for signal MC samples. The variations compared to the original values are listed in Table 7.2. The maximum variation for all the signal points tested doesn't exceed 9%, we thus assign a 9% systematic uncertainty to the online tracking.

Table 7.2: The variations of signal efficiencies due to the mismodeling of online tracking.

Variations	**Jet-jet model**			
	$c\tau_0 = 1\,\mathrm{mm}$	$c\tau_0 = 10\,\mathrm{mm}$	$c\tau_0 = 100\,\mathrm{mm}$	$c\tau_0 = 1000\,\mathrm{mm}$
$m_X = 1000\,\mathrm{GeV}$	8.3%	0.5%	0.1%	0.4%
$m_X = 700\,\mathrm{GeV}$	8.2%	0.5%	0.1%	0.3%
$m_X = 500\,\mathrm{GeV}$	7.9%	0.4%	0.1%	0.4%
$m_X = 300\,\mathrm{GeV}$	7.9%	0.6%	0.2%	0.5%
$m_X = 100\,\mathrm{GeV}$	8.1%	0.8%	0.6%	0.1%

Variations	**GMSB $\widetilde{\mathrm{g}} \to \mathrm{g}\widetilde{\mathrm{G}}$**			
	$c\tau_0 = 1\,\mathrm{mm}$	$c\tau_0 = 10\,\mathrm{mm}$	$c\tau_0 = 100\,\mathrm{mm}$	$c\tau_0 = 1000\,\mathrm{mm}$
$m_{\widetilde{\mathrm{g}}}$ =2400 GeV	9.2%	0.9%	0.3%	0.3%
$m_{\widetilde{\mathrm{g}}}$ =1000 GeV	8.0%	0.1%	0.5%	0.9%

Variations	**RPV $\widetilde{\mathrm{g}} \to \mathrm{tbs}$**			
	$c\tau_0 = 1\,\mathrm{mm}$	$c\tau_0 = 10\,\mathrm{mm}$	$c\tau_0 = 100\,\mathrm{mm}$	$c\tau_0 = 1000\,\mathrm{mm}$
$m_{\widetilde{\mathrm{g}}}$ =2400 GeV	8.6%	0.6%	0.1%	0.1%
$m_{\widetilde{\mathrm{g}}}$ =1200 GeV	8.8%	0.6%	0.1%	0.1%

Variations	**RPV $\widetilde{\mathrm{t}} \to \mathrm{b}\ell$**			
	$c\tau_0 = 1\,\mathrm{mm}$	$c\tau_0 = 10\,\mathrm{mm}$	$c\tau_0 = 100\,\mathrm{mm}$	$c\tau_0 = 1000\,\mathrm{mm}$
$m_{\widetilde{\mathrm{t}}} = 1200\,\mathrm{GeV}$	9.1%	1.4%	0.7%	0.9%
$m_{\widetilde{\mathrm{t}}} = 600\,\mathrm{GeV}$	8.0%	0.1%	0.8%	1.2%

Variations	**dRPV $\widetilde{\mathrm{t}} \to \overline{\mathrm{dd}}$**			
	$c\tau_0 = 1\,\mathrm{mm}$	$c\tau_0 = 10\,\mathrm{mm}$	$c\tau_0 = 100\,\mathrm{mm}$	$c\tau_0 = 1000\,\mathrm{mm}$
$m_{\widetilde{\mathrm{t}}} = 1600\,\mathrm{GeV}$	9.4%	0.8%	0.8%	0.2%
$m_{\widetilde{\mathrm{t}}} = 800\,\mathrm{GeV}$	9.2%	0.8%	0.2%	0.4%

7.2 Offline vertexing systematics

Since the secondary vertex reconstruction relies on the offline tracking, the modeling of the offline tracking will have significant impact on the signal acceptance of this analysis. In early 2016, the CMS tracker was influenced by the so-called HIP effect, where a loss of hit efficiency was observed in the silicon strip tracker due to the saturation in analog pipeline (voltage mode) (APV) read-out chips of strip tracker. The APV saturation was fixed after fill 5198, but before that (i.e. in Run2016B-F) the offline tracking efficiencies became worse when going to higher instantaneous luminosity.

To disentangle the offline tracking performance from the online tracking performance, we studied the data taken by the pre-scaled control path `HLT_HT325_v`, which only consists of the online CALO H_{T} requirement and doesn't utilize online tracking. The number of tracks and transverse displacement (L_{xy}) for reconstructed secondary vertices are shown in Figure 7.5 and 7.6, for Run2016B-F and Run2016G-H separately as well as combining all the data across the whole 2016 data taking period. For the whole combined data in 2016, the observed data are in good agreement with QCD MC simulation, and the impact of the deviation is negligible on the entire 2016 dataset. However, in Run2016B-F, the secondary vertices tend to lose tracks due to the APV saturation issue, therefore there are fewer tracks in the observed data than the MC simulation. In order to quantify the impact of this inefficiency, we define a scale factor as follows:

$$SF(N_{\mathrm{SV.track}}) = \frac{\epsilon_{\mathrm{data}}(N_{\mathrm{SV.track}})}{\epsilon_{\mathrm{MC}}(N_{\mathrm{SV.track}})} \tag{7.3}$$

where $N_{\mathrm{SV.track}}$ is the number of tracks in the secondary vertex, $\epsilon(N_{\mathrm{SV.track}})$ is the yield of secondary vertices when the track multiplicity is $N_{\mathrm{SV.track}}$. $(1 - SF)$ represents the loss of vertex efficiency in data compared to MC simulation, and can be as large as

$\sim 50\%$ in Run2016B-F.

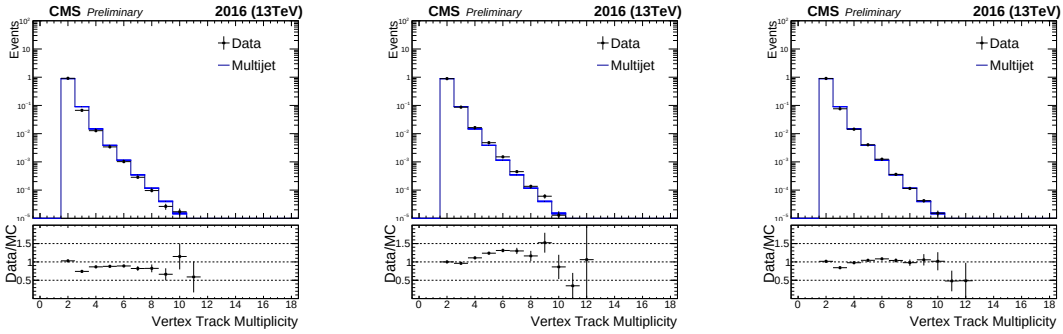

(a) Run2016B-F (b) Run2016G-H (c) Run2016 All

Figure 7.5: Vertex track multiplicity for events collected by control path `HLT_HT_325_v`, CALO jets are required to satisfy p_{T} >50 GeV and $|\eta| < 2.0$. (a) Events recorded in data taking periods Run2016B-F, which is affected by the APV saturation issue in the tracker; (b) Events recorded in data taking periods Run2016G-H, where the APV saturation issue is fixed; (c) Events collected during the entire 2016 data-taking period.

To estimate the impact on the signal efficiency, we compute $SF(N_{\mathrm{SV.track}})$ with Run2016B-F data, where the deviation from MC simulation is most severe. Then for each secondary vertex candidate in the signal MC, we generate a random number from uniform distribution $r \in [0, 1]$. If $r > SF(N_{\mathrm{SV.track}})$, the secondary vertex candidate is removed from the event. We then recompute the signal efficiencies for signal models, the relative variations of signal efficiencies are summarized in Table 7.3. In general, the loss of signal efficiency becomes larger for low mass or long lifetime, since there are fewer tracks in the reconstructed secondary vertices, thus the vertices are more easily lost. The uncertainties are found to be 2%–15% for different signal models considered.

Table 7.3: The variations of signal efficiencies due to the mismodeling of offline vertexing.

Variations	**Jet-jet model**			
	$c\tau_0 = 1\,\mathrm{mm}$	$c\tau_0 = 10\,\mathrm{mm}$	$c\tau_0 = 100\,\mathrm{mm}$	$c\tau_0 = 1000\,\mathrm{mm}$
$m_X = 1000\,\mathrm{GeV}$	1.0%	0.8%	1.6%	2.8%
$m_X = 700\,\mathrm{GeV}$	1.6%	1.3%	2.3%	3.8%
$m_X = 500\,\mathrm{GeV}$	2.0%	2.0%	3.2%	4.1%
$m_X = 300\,\mathrm{GeV}$	4.4%	3.2%	3.9%	4.3%
$m_X = 100\,\mathrm{GeV}$	8.7%	5.4%	9.7%	3.9%
$m_X = 50\,\mathrm{GeV}$	13.6%	10.9%	10.0%	–%

Variations	**GMSB $\tilde{\mathrm{g}} \to \mathrm{g}\tilde{\mathrm{G}}$**			
	$c\tau_0 = 1\,\mathrm{mm}$	$c\tau_0 = 10\,\mathrm{mm}$	$c\tau_0 = 100\,\mathrm{mm}$	$c\tau_0 = 1000\,\mathrm{mm}$
$m_{\tilde{\mathrm{g}}}$ =2400 GeV	0.1%	0.4%	0.5%	0.9%
$m_{\tilde{\mathrm{g}}}$ =1000 GeV	0.6%	0.4%	1.2%	1.6%

Variations	**RPV $\tilde{\mathrm{g}} \to \mathrm{tbs}$**			
	$c\tau_0 = 1\,\mathrm{mm}$	$c\tau_0 = 10\,\mathrm{mm}$	$c\tau_0 = 100\,\mathrm{mm}$	$c\tau_0 = 1000\,\mathrm{mm}$
$m_{\tilde{\mathrm{g}}}$ =2400 GeV	0.1%	0.2%	0.5%	0.1%
$m_{\tilde{\mathrm{g}}}$ =1200 GeV	0.1%	0.6%	0.1%	0.1%

Variations	**RPV $\tilde{\mathrm{t}} \to \mathrm{b}\ell$**			
	$c\tau_0 = 1\,\mathrm{mm}$	$c\tau_0 = 10\,\mathrm{mm}$	$c\tau_0 = 100\,\mathrm{mm}$	$c\tau_0 = 1000\,\mathrm{mm}$
$m_{\tilde{\mathrm{t}}}$ =1200 GeV	3.4%	2.6%	2.9%	3.4%
$m_{\tilde{\mathrm{t}}}$ =600 GeV	3.6%	4.4%	5.0%	5.0%

Variations	**dRPV $\tilde{\mathrm{t}} \to \overline{\mathrm{d}}\overline{\mathrm{d}}$**			
	$c\tau_0 = 1\,\mathrm{mm}$	$c\tau_0 = 10\,\mathrm{mm}$	$c\tau_0 = 100\,\mathrm{mm}$	$c\tau_0 = 1000\,\mathrm{mm}$
$m_{\tilde{\mathrm{t}}}$ =1600 GeV	0.6%	0.2%	0.2%	1.2%
$m_{\tilde{\mathrm{t}}}$ =800 GeV	0.7%	0.6%	1.2%	2.4%

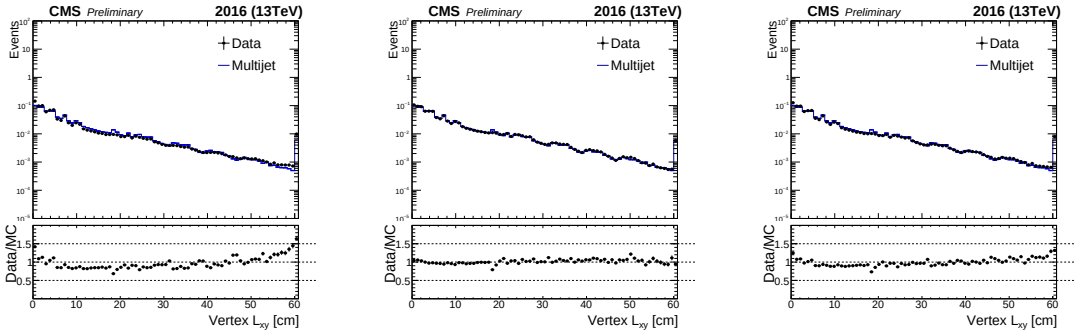

(a) Run2016B-F (b) Run2016G-H (c) Run2016 All

Figure 7.6: Transverse displacement (L_{xy}) of the secondary vertices for events collected by control path `HLT_HT_325_v`, CALO jets are required to satisfy p_{T} >50 GeV and $|\eta| < 2.0$. (a) Events recorded in data taking periods Run2016B-F, which is affected by the APV saturation issue in the tracker; (b) Events recorded in data taking periods Run2016G-H, where the APV saturation issue is fixed; (c) Events collected during the entire 2016 data-taking period.

7.3 Track impact parameter modeling uncertainty

To estimate the impact of the discrepancy between data and MC simulation observed in the number of 3D prompt tracks, we studied the distribution of 3D impact parameter with events collected with the pre-scaled control path `HLT_HT325_v`, selecting the tracks associated with the jets satisfying $p_{\mathrm{T}} > 50\,\mathrm{GeV}$, $|\eta| < 2.0$. We then varied the impact parameter measured in the QCD MC sample systematically by δ% till it (at least partly) covers the discrepancy observed in data and QCD MC simulation. As shown in Figure 7.8, $\delta = -45/+50$ would provide an envelope that covers the distribution observed in data. We then varied the track impact parameter in the signal MC samples track by track by the same magnitude, and examined the variations in the signal efficiencies, which are summarized in Table 7.4. The systematic uncertainty due to the IP modeling is then estimated to be 14%–20% for the signal models considered.

Table 7.4: The variations of signal efficiencies due to the mismodeling of offline track impact parameters.

Variations	**Jet-jet model**			
	$c\tau_0 = 1\,\mathrm{mm}$	$c\tau_0 = 10\,\mathrm{mm}$	$c\tau_0 = 100\,\mathrm{mm}$	$c\tau_0 = 1000\,\mathrm{mm}$
$m_X = 1000\,\mathrm{GeV}$	13.7%	6.0%	1.8%	1.4%
$m_X = 500\,\mathrm{GeV}$	12.9%	4.7%	1.9%	2.6%
$m_X = 300\,\mathrm{GeV}$	13.7%	3.2%	1.5%	3.2%
$m_X = 100\,\mathrm{GeV}$	9.0%	3.2%	1.4%	0%

Variations	**GMSB $\widetilde{\mathrm{g}} \to \mathrm{g}\widetilde{\mathrm{G}}$**			
	$c\tau_0 = 1\,\mathrm{mm}$	$c\tau_0 = 10\,\mathrm{mm}$	$c\tau_0 = 100\,\mathrm{mm}$	$c\tau_0 = 1000\,\mathrm{mm}$
$m_{\widetilde{\mathrm{g}}} = 2500\,\mathrm{GeV}$	16.2%	9.6%	2.9%	2.0%
$m_{\widetilde{\mathrm{g}}} = 2000\,\mathrm{GeV}$	13.8%	8.0%	3.2%	2.0%
$m_{\widetilde{\mathrm{g}}} = 1500\,\mathrm{GeV}$	12.7%	6.9%	3.0%	1.7%

Variations	**RPV $\widetilde{\mathrm{g}} \to \mathrm{tbs}$**			
	$c\tau_0 = 1\,\mathrm{mm}$	$c\tau_0 = 10\,\mathrm{mm}$	$c\tau_0 = 100\,\mathrm{mm}$	$c\tau_0 = 1000\,\mathrm{mm}$
$m_{\widetilde{\mathrm{g}}} = 2600\,\mathrm{GeV}$	19.2%	11.1%	3.5%	2.7%
$m_{\widetilde{\mathrm{g}}} = 1800\,\mathrm{GeV}$	20.0%	9.6%	6.1%	2.3%
$m_{\widetilde{\mathrm{g}}} = 1200\,\mathrm{GeV}$	19.5%	8.3%	3.1%	2.8%

Variations	**RPV $\widetilde{\mathrm{t}} \to \mathrm{b}\ell$**			
	$c\tau_0 = 1\,\mathrm{mm}$	$c\tau_0 = 10\,\mathrm{mm}$	$c\tau_0 = 100\,\mathrm{mm}$	$c\tau_0 = 1000\,\mathrm{mm}$
$m_{\widetilde{\mathrm{t}}} = 1200\,\mathrm{GeV}$	3.8%	6.7%	1.2%	0.6%
$m_{\widetilde{\mathrm{t}}} = 1000\,\mathrm{GeV}$	9.4%	3.0%	2.7%	0.2%
$m_{\widetilde{\mathrm{t}}} = 600\,\mathrm{GeV}$	2.3%	3.5%	1.5%	1.6%

Variations	**dRPV $\widetilde{\mathrm{t}} \to \overline{\mathrm{d}}\overline{\mathrm{d}}$**			
	$c\tau_0 = 1\,\mathrm{mm}$	$c\tau_0 = 10\,\mathrm{mm}$	$c\tau_0 = 100\,\mathrm{mm}$	$c\tau_0 = 1000\,\mathrm{mm}$
$m_{\widetilde{\mathrm{t}}} = 1600\,\mathrm{GeV}$	19.1%	9.3%	4.2%	2.5%
$m_{\widetilde{\mathrm{t}}} = 1200\,\mathrm{GeV}$	17.6%	8.1%	3.1%	2.0%
$m_{\widetilde{\mathrm{t}}} = 800\,\mathrm{GeV}$	15.3%	6.2%	3.2%	2.5%

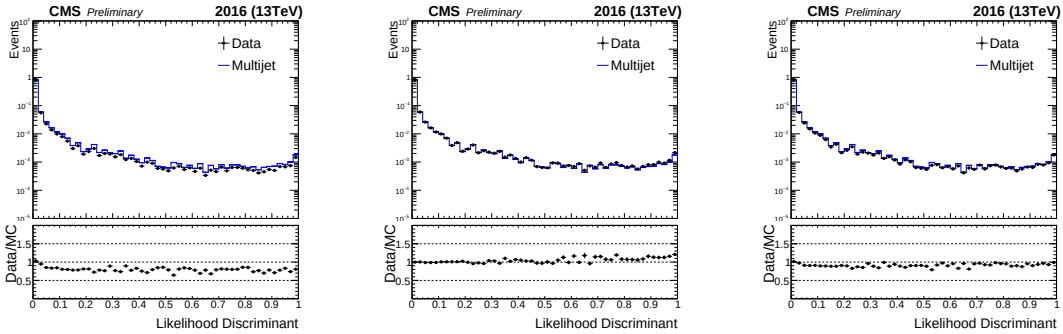

(a) Run2016B-F (b) Run2016G-H (c) Run2016 All

Figure 7.7: Likelihood Discriminant of the secondary vertices for events collected by control path `HLT_HT_325_v`, CALO jets are required to satisfy p_{T} >50 GeV and $|\eta| < 2.0$. (a) Events recorded in data taking periods Run2016B-F, which is affected by the APV saturation issue in the tracker; (b) Events recorded in data taking periods Run2016G-H, where the APV saturation issue is fixed; (c) Events collected during the entire 2016 data-taking period.

7.4 Jet energy correction uncertainty

The energy response of the reconstructed jets needs to be corrected to take account of various effects [104]. First, the L1Fast correction was applied to remove the pileup contribution and electronic noise. The L2L3 correction was then applied to correct the particle level jet response based on the MC simulation. For the real data sample, the L2L3Residual correction was further applied to compensate the difference within jet response between MC and data. The uncertainties of Jet Energy Correction (JEC) were provided by the JERC group and can be calculated jet by jet both for MC and data.

To estimate the impact of JEC uncertainty on the signal efficiency of the analysis, the p_{T} of each jet is varied up and down, and all the other variables that depend on the jet p_{T} or energy (i.e. H_{T}, ζ, and charged prompt energy fraction) are also varied simultaneously. We then reapplied the full selections to get the variations of

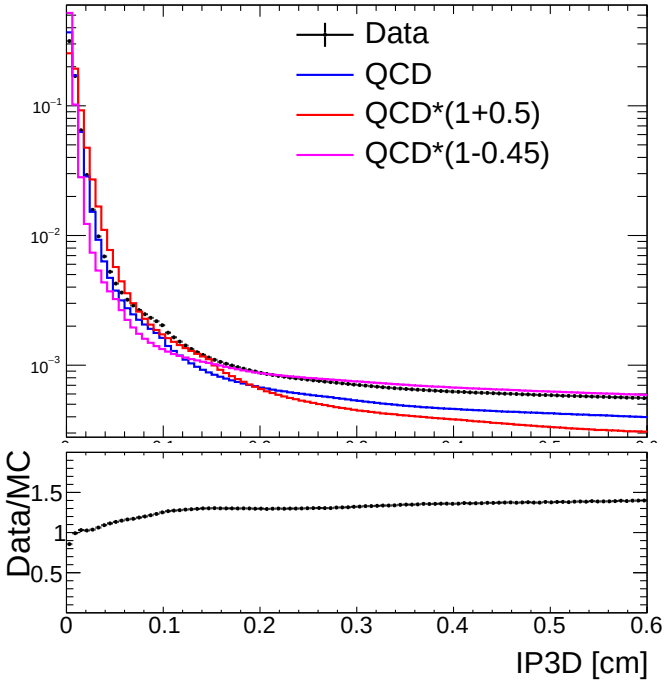

Figure 7.8: The distribution of 3D impact parameter for tracks (`high purity`, $p_{\mathrm{T}} > 1\,\mathrm{GeV}$) associated with jets satisfying $p_{\mathrm{T}} > 50\,\mathrm{GeV}$ and $|\eta| < 2.0$. The events are collected by `HLT_HT325_v` and the offline CALO H_{T} is required to be larger than 400 GeV. For QCD MC sample, the distribution after shifts by -45% and by +50% are also plotted, which provide an envelope that covers the distribution observed in data.

signal efficiencies, the largest variations from either side are treated as the signal systematics due to the JEC uncertainty. The results mainly depend on the mass of the long-lived particle, which are summarized in Table 7.5. The impact of the JER smearing on the signal efficiencies is very small and negligible (the changes in signal acceptance are at per-mille level for with or without JER smearing), thus no further systematic uncertainties are added.

Table 7.5: The variations of signal efficiencies for different models due to jet energy correction uncertainty

Jet-jet model				
m_X	50 GeV	100 GeV	300 GeV	1000 GeV
Variations	4.4%	3.5%	1.0%	0.2%

GMSB $\widetilde{\mathbf{g}} \rightarrow \mathbf{g}\widetilde{\mathbf{G}}$				
$m_{\widetilde{\mathrm{g}}}$	1000 GeV	1500 GeV	2000 GeV	2500 GeV
Variations	0.9%	1.3%	0.5%	0.5%

RPV $\widetilde{\mathbf{g}} \rightarrow \mathbf{tbs}$				
$m_{\widetilde{\mathrm{g}}}$	1200 GeV	1800 GeV	2000 GeV	2600 GeV
Variations	0.8%	1.4%	0.5%	0.5%

RPV $\widetilde{\mathbf{t}} \rightarrow \mathbf{b}\boldsymbol{\ell}$			
$m_{\widetilde{\mathrm{t}}}$	600 GeV	1000 GeV	1200 GeV
Variations	1.7%	0.6%	0.5%

dRPV $\widetilde{\mathbf{t}} \rightarrow \overline{\mathbf{dd}}$			
$m_{\widetilde{\mathrm{t}}}$	800 GeV	1000 GeV	1600 GeV
Variations	1.8%	0.7%	0.4%

7.5 PDF uncertainty

Following the recommendations from the PDF4LHC group [121], we utilized three PDF sets – **NNPDF**, **CT** and **MMHT** – to estimate the PDF uncertainty of the signal acceptance. We first reweighted the signal MC samples to the three PDF sets using the LHAPDF tool [122]. For **NNPDF** PDF set, we calculated the RMS of the PDF weights due to the choice of different eigenvectors:

$$\mathrm{RMS}(f_{\mathrm{NNPDF}}) = \sqrt{\frac{1}{N}\sum_{i=1}^{N}\left(\frac{f^{(i)}_{\mathrm{NNPDF}}}{f^{(0)}_{\mathrm{NNPDF}}} - 1\right)^2} \tag{7.4}$$

where $f^{(i)}_{\mathrm{NNPDF}}$ is the weight of the ith eigenvector in **NNPDF**, and $f^{(0)}_{\mathrm{NNPDF}}$ is the weight of the central eigenvector. We then varied the central **NNPDF** PDF weights up and down by the size of $\mathrm{RMS}(f_{\mathrm{NNPDF}})$, and calculate the variations of signal efficiencies correspondingly.

Second, we also reweighted the signal MC using the central weights of **CT** and **MMHT** PDF sets, and computed the largest variations of signal efficiencies compared to **NNPDF**.

The systematics due the choices of PDF is taken as the square root of the quadratic sum of the two variations, which are summarized in Table 7.6. In general, the largest deviation doesn't exceed 4%–6% for different signal models considered.

7.6 Primary vertex selection uncertainty

In the case of displaced jets scenarios, one may wonder how reliable the selection of the true primary vertex for signal events is, and what is its impact on this analysis.

Table 7.6: The variations of signal efficiencies due to the choices of PDF sets.

Variations	**Jet-jet model**			
	$c\tau_0 = 1\,\mathrm{mm}$	$c\tau_0 = 10\,\mathrm{mm}$	$c\tau_0 = 100\,\mathrm{mm}$	$c\tau_0 = 1000\,\mathrm{mm}$
$m_X = 1000\,\mathrm{GeV}$	1.3%	0.1%	0.4%	0.4%
$m_X = 300\,\mathrm{GeV}$	0.3%	1.0%	1.5%	1.2%
$m_X = 100\,\mathrm{GeV}$	1.2%	1.3%	0.8%	1.2%
$m_X = 50\,\mathrm{GeV}$	4.6%	3.8%	3.4%	3.4%

Variations	**GMSB $\widetilde{\mathrm{g}} \to \mathrm{g}\widetilde{\mathrm{G}}$**			
	$c\tau_0 = 1\,\mathrm{mm}$	$c\tau_0 = 10\,\mathrm{mm}$	$c\tau_0 = 100\,\mathrm{mm}$	$c\tau_0 = 1000\,\mathrm{mm}$
$m_{\widetilde{\mathrm{g}}} = 2500\,\mathrm{GeV}$	5.8%	4.8%	4.8%	5.4%
$m_{\widetilde{\mathrm{g}}} = 2000\,\mathrm{GeV}$	6.0%	1.4%	0.4%	2.2%
$m_{\widetilde{\mathrm{g}}} = 1600\,\mathrm{GeV}$	3.2%	1.0%	3.0%	2.5%
$m_{\widetilde{\mathrm{g}}} = 1000\,\mathrm{GeV}$	2.0%	0.6%	0.8%	0.8%

Variations	**RPV $\widetilde{\mathrm{g}} \to \mathrm{tbs}$**			
	$c\tau_0 = 1\,\mathrm{mm}$	$c\tau_0 = 10\,\mathrm{mm}$	$c\tau_0 = 100\,\mathrm{mm}$	$c\tau_0 = 1000\,\mathrm{mm}$
$m_{\widetilde{\mathrm{g}}} = 2400\,\mathrm{GeV}$	3.6%	1.6%	0.3%	1.4%
$m_{\widetilde{\mathrm{g}}} = 1800\,\mathrm{GeV}$	3.2%	0.2%	0.3%	0.7%
$m_{\widetilde{\mathrm{g}}} = 1200\,\mathrm{GeV}$	3.7%	0.8%	0.5%	0.6%

Variations	**RPV $\widetilde{\mathrm{t}} \to \mathrm{b}\ell$**			
	$c\tau_0 = 1\,\mathrm{mm}$	$c\tau_0 = 10\,\mathrm{mm}$	$c\tau_0 = 100\,\mathrm{mm}$	$c\tau_0 = 1000\,\mathrm{mm}$
$m_{\widetilde{\mathrm{t}}} = 1200\,\mathrm{GeV}$	4.8%	4.0%	0.6%	4.2%
$m_{\widetilde{\mathrm{t}}} = 1000\,\mathrm{GeV}$	3.2%	3.2%	1.5%	3.0%
$m_{\widetilde{\mathrm{t}}} = 800\,\mathrm{GeV}$	1.2%	1.3%	0.8%	1.2%
$m_{\widetilde{\mathrm{t}}} = 600\,\mathrm{GeV}$	3.1%	1.3%	1.1%	0.9%

Variations	**RPV $\widetilde{\mathrm{t}} \to \overline{\mathrm{dd}}$**			
	$c\tau_0 = 1\,\mathrm{mm}$	$c\tau_0 = 10\,\mathrm{mm}$	$c\tau_0 = 100\,\mathrm{mm}$	$c\tau_0 = 1000\,\mathrm{mm}$
$m_{\widetilde{\mathrm{t}}} = 1600\,\mathrm{GeV}$	3.5%	0.4%	0.4%	1.7%
$m_{\widetilde{\mathrm{t}}} = 1200\,\mathrm{GeV}$	2.6%	0.5%	0.8%	4.2%
$m_{\widetilde{\mathrm{t}}} = 800\,\mathrm{GeV}$	4.3%	0.3%	1.2%	2.0%

When designing the analysis strategy, we mainly used the 2D variables so that the analysis is not sensitive to the primary vertex selection. To quantify the possible impact, we select the sub-leading primary vertex instead of the leading one in the PV collection, and recompute the impact parameters and the vertex displacement. The variations of the signal efficiencies for different signal model are summarized in Table 7.7, in which the largest variation doesn't exceed 6%–15%.

We summarize the systematics of signal efficiencies in Table 7.8. For a given signal model, the largest variation due to each source across the tested mass-lifetime points is taken as the corresponding systematic uncertainties. The total systematic uncertainty is dominated by the uncertainties due to online and offline tracking, especially in the cases where the mass of the long-lived particle is small and the life-time is large.

Table 7.7: The variations of signal efficiencies when using the sub-leading primary vertex instead of the leading one.

Variations	**Jet-jet model**			
	$c\tau_0 = 1\,\mathrm{mm}$	$c\tau_0 = 10\,\mathrm{mm}$	$c\tau_0 = 100\,\mathrm{mm}$	$c\tau_0 = 1000\,\mathrm{mm}$
$m_X = 1000\,\mathrm{GeV}$	6.3%	4.2%	1.7%	2.4%
$m_X = 300\,\mathrm{GeV}$	1.9%	0.1%	1.0%	4.3%
$m_X = 100\,\mathrm{GeV}$	2.2%	0.2%	0.4%	5.8%

Variations	**GMSB $\widetilde{\mathrm{g}} \to \mathrm{g}\widetilde{\mathrm{G}}$**			
	$c\tau_0 = 1\,\mathrm{mm}$	$c\tau_0 = 10\,\mathrm{mm}$	$c\tau_0 = 100\,\mathrm{mm}$	$c\tau_0 = 1000\,\mathrm{mm}$
$m_{\widetilde{\mathrm{g}}} = 2500\,\mathrm{GeV}$	10.4%	8.1%	7.2%	0.7%
$m_{\widetilde{\mathrm{g}}} = 1000\,\mathrm{GeV}$	2.5%	4.5%	2.0%	0.7%

Variations	**RPV $\widetilde{\mathrm{g}} \to \mathrm{tbs}$**			
	$c\tau_0 = 1\,\mathrm{mm}$	$c\tau_0 = 10\,\mathrm{mm}$	$c\tau_0 = 100\,\mathrm{mm}$	$c\tau_0 = 1000\,\mathrm{mm}$
$m_{\widetilde{\mathrm{g}}} = 2600\,\mathrm{GeV}$	14.4%	5.9%	3.1%	3.8%
$m_{\widetilde{\mathrm{g}}} = 1800\,\mathrm{GeV}$	15.4%	5.3%	5.1%	3.5%
$m_{\widetilde{\mathrm{g}}} = 1200\,\mathrm{GeV}$	14.6%	5.6%	7.7%	7.6%

Variations	**RPV $\widetilde{\mathrm{t}} \to \mathrm{b}\ell$**			
	$c\tau_0 = 1\,\mathrm{mm}$	$c\tau_0 = 10\,\mathrm{mm}$	$c\tau_0 = 100\,\mathrm{mm}$	$c\tau_0 = 1000\,\mathrm{mm}$
$m_{\widetilde{\mathrm{t}}} = 1200\,\mathrm{GeV}$	7.8%	4.1%	4.8%	3.4%
$m_{\widetilde{\mathrm{t}}} = 600\,\mathrm{GeV}$	5.2%	3.3%	3.1%	5.1%

Variations	**RPV $\widetilde{\mathrm{t}} \to \overline{\mathrm{d}}\overline{\mathrm{d}}$**			
	$c\tau_0 = 1\,\mathrm{mm}$	$c\tau_0 = 10\,\mathrm{mm}$	$c\tau_0 = 100\,\mathrm{mm}$	$c\tau_0 = 1000\,\mathrm{mm}$
$m_{\widetilde{\mathrm{t}}} = 1600\,\mathrm{GeV}$	7.0%	5.3%	5.7%	3.1%
$m_{\widetilde{\mathrm{t}}} = 1200\,\mathrm{GeV}$	9.9%	3.6%	5.7%	0.9%
$m_{\widetilde{\mathrm{t}}} = 800\,\mathrm{GeV}$	12.1%	4.2%	4.6%	5.1%

Table 7.8: Systematic uncertainties of the signal yields

Source	Jet-jet model	$\widetilde{\mathrm{g}} \to \mathrm{g}\widetilde{\mathrm{G}}$	$\widetilde{\mathrm{g}} \to \mathrm{tbs}$	$\widetilde{\mathrm{t}} \to \mathrm{b}\ell$	$\widetilde{\mathrm{t}} \to \overline{\mathrm{dd}}$
Integrated luminosity	2.5%	2.5%	2.5%	2.5%	2.5%
Online H_{T} requirement	2.5%	2.5%	2.5%	2.5%	2.5%
Online tracking requirement	9%	9%	9%	9%	10%
Offline vertexing	15%	2%	6%	5%	2%
Track impact parameter modeling	14%	16%	20%	10%	20%
Jet energy scale	4%	2%	2%	2%	2%
PDF	5%	6%	4%	5%	4%
Primary vertex selection	6%	10%	15%	8%	12%
Total	24%	22%	28%	18%	26%

Chapter 8

Results

8.1 Predicted background in the signal region

The signal region of this analysis is defined by the optimized selections determined in section 6.5, which are:

- for the leading jet, charged prompt energy fraction $< 15\%$, number of 3D prompt tracks < 2;
- for the sub-leading jet, charged prompt energy fraction $< 13\%$, number of 3D prompt tracks < 2;
- vertex likelihood discriminant > 0.9993.

Using the ABCD(EFGH) method described in section 6.1, the predicted background with 2016 data is:

$$1.03 \pm 0.11(\text{sys.}) \pm 0.19(\text{sta.}). \tag{8.1}$$

If we bin the signal region by offline CALO H_{T} and number of dijet candidates passing pre-selection, the predicted background will be:

- number of dijet candidates > 1: $0.16 \pm 0.06 \pm 0.11$;
- number of dijet candidates $= 1$, $400 < H_{\mathrm{T}} < 450\,\mathrm{GeV}$: $0.42 \pm 0.01 \pm 0.14$;
- number of dijet candidates $= 1$, $450 < H_{\mathrm{T}} < 550\,\mathrm{GeV}$: $0.23 \pm 0.07 \pm 0.08$;
- number of dijet candidates $= 1$, $H_{\mathrm{T}} > 550\,\mathrm{GeV}$: $0.19 \pm 0.05 \pm 0.07$.

These four bins are used for limit setting. The impact of the binning on the limit setting is small, since the inclusive region is already nearly background-free.

8.2 Observed event in the signal region

With the full selection applied, we observed 1 event in the 2016 data, which is consistent with the predicted 1.03 events for background. This event falls in the bin where the number of dijet candidates equals 1 and $H_{\mathrm{T}} > 550\,\mathrm{GeV}$. The event display of this event is shown in Figure 8.1, which contains a secondary vertex candidate with a transverse decay length of 3.5 cm. This event could be a very striking $\mathrm{t\bar{t}}$ event (or QCD multijet event through gluon splitting $\mathrm{g} \to \mathrm{b\bar{b}}$). The event display of some striking $\mathrm{t\bar{t}}$ events which have similar topology can be found in Figure 8.2

8.3 Limit setting

We set the limit on a given interpretation by computing the 95% confidence level (C.L.) associated with each signal point according to the $\mathrm{CL_s}$ prescription [123, 124, 125, 126]. In the $\mathrm{CL_s}$ prescription, we start with a (binned) likelihood function for observed n_i events in the ith bin:

$$\mathcal{L}(\mu, \theta) = \prod_i \frac{(\mu S_i(\theta) + B_i(\theta))^{n_i}}{n_i!} \exp\left[-\left(\mu S_i(\theta) + B_i(\theta)\right)\right] \pi(\theta), \tag{8.2}$$

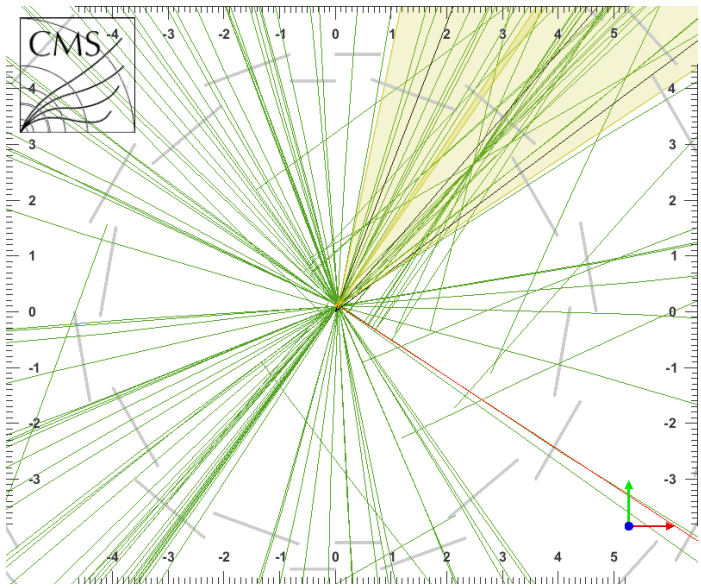

Figure 8.1: The event display of the event passing all the selections

where S_i is the signal yield in the ith bin, B_i is the background yield in the ith bin, θ includes all the nuisance parameters, $\pi(\theta)$ is the prior probability distribution function of θ, and μ is the signal strength. The Neyman-Pearson lemma [127] states that the likelihood ratio provides the most powerful test in hypothesis testing. ATLAS and CMS adopt a modified profile likelihood ratio as the test statistics for upper limits setting:

$$\tilde{q}_\mu = -2 \ln \frac{\mathcal{L}(\mu, \hat{\hat{\theta}})}{\mathcal{L}(\hat{\mu}, \hat{\theta})}, \quad \text{with } 0 \leq \hat{\mu} \leq \mu, \tag{8.3}$$

where $(\hat{\mu}, \hat{\theta})$ represents the maximization point of the likelihood function, while $\hat{\hat{\theta}}$ represents the conditional maximization point of the likelihood function with μ being fixed. Under a given hypothesis with $\mu = \mu'$, $\theta = \theta'$, we can find out the probability distribution function (pdf) of $\tilde{q}_\mu$: $f(\tilde{q}_\mu|\mu', \theta')$. In practice, θ' is usually replaced by its maximal likelihood estimator $\hat{\hat{\theta}}$ based on the observed data. The pdf $f(\tilde{q}_\mu|\mu', \hat{\hat{\theta}})$ can be estimated by generating MC pseudo-data. After constructing $f(\tilde{q}_\mu)$ under the background-only hypothesis ($f(\tilde{q}_\mu|0, \hat{\hat{\theta}}_0)$) and the signal+background hy-

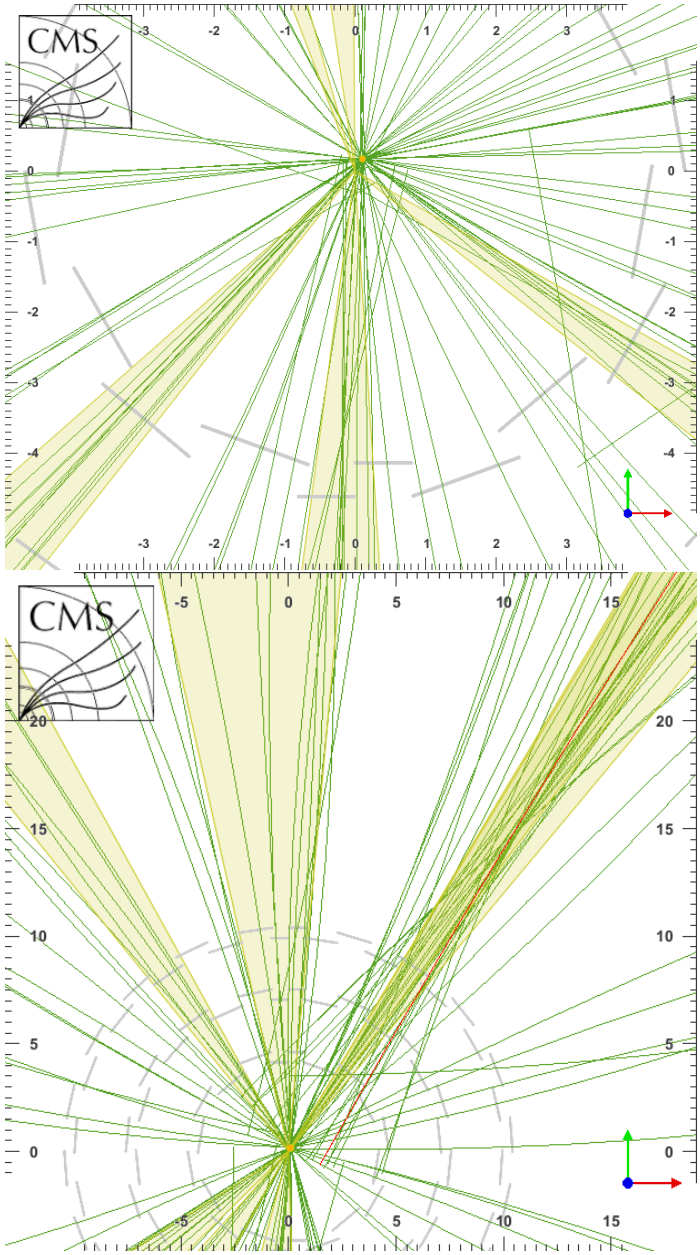

Figure 8.2: The event display of two striking $t\bar{t}$ events

pothesis ($f(\tilde{q}_\mu|\mu, \hat{\hat{\theta}}_\mu)$), we can build the p-values for background-only hypothesis and

signal+background hypothesis:

$$p_b = \int_{\tilde{q}_\mu^{\rm obs}}^{\infty} d\tilde{q}_\mu \; f(\tilde{q}_\mu|0, \hat{\hat{\theta}}_0), \tag{8.4}$$

$$p_{s+b} = \int_{\tilde{q}_\mu^{\rm obs}}^{\infty} d\tilde{q}_\mu \; f(\tilde{q}_\mu|\mu, \hat{\hat{\theta}}_\mu). \tag{8.5}$$

The $\mathrm{CL_s}$ value can then be calculated based on p_b and p_{s+b}:

$$\mathrm{CL_s}(\mu) = \frac{p_{s+b}}{1 - p_b}. \tag{8.6}$$

For $\mu = 1$, when $\mathrm{CL_s} \leq \alpha$ we can state that the signal is excluded at the $(1 - \alpha)$ confidence level.

We calculate the $\mathrm{CL_s}$ values using the asymptotic approximation [125], where the signal yields in the four bins of the signal region are utilized for the computation, and the systematic uncertainties are taken to be fully correlated across the four bins. The calculations based on the asymptotic approximation are cross-checked with the full-frequentist results for representative signal points, as shown in Figure 8.4.

8.4 Jet-jet interpretation

In the jet-jet model, two long-lived scalar neutral particles X are pair-produced through a 2→2 scattering process, mediated by a Z^* propagator. The signature often has two displaced vertices, each of them the origin of one displaced dijet pair. The expected and observed limits of the pair production cross sections for the jet-jet Model is shown in Figure 8.3, with different scalar mass m_X and proper decay length $c\tau_0$. The excluded pair production cross section can be as low as $\sim$ 0.2 fb at high mass (m_X =1000 GeV) for proper decay lengths between 3mm and 130mm.

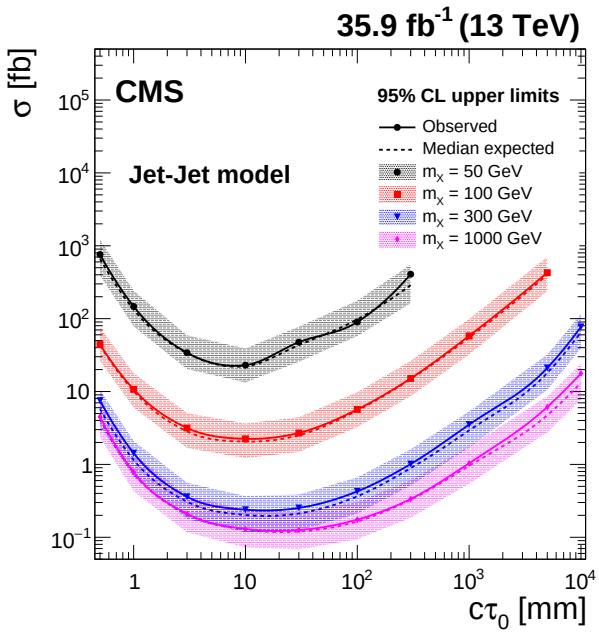

Figure 8.3: The expected and observed 95% C.L. upper limits on the pair production cross section of the long-lived particle X, assuming a 100% branching fraction for X to decay to a quark-antiquark pair, shown at different particle X masses and proper decay lengths for the jet-jet model. The solid (dashed) lines represent the observed (median expected) limits. The shaded bands represent the regions containing 68% of the distributions of the expected limits under the background-only hypothesis.

8.5 GMSB $\widetilde{g} \rightarrow g\widetilde{G}$ interpretation

In the GMSB long-lived gluino scenario, the gluino is pair produced and decays to a gluon and a gravitino. The gravitino is the LSP and manifests itself as missing energy. If the gluino is long-lived, the signature would be two displaced vertices, each of them containing a single displaced jet and missing energy. Though the analysis is commissioned with dijets, since we don't require the displaced vertex contains tracks from both jets, the two separate displaced single jets can be paired together. As long as the secondary vertex fitted from the two jets passes the selections, the analysis will be sensitive to displaced single jets. The expected limit of the pair production

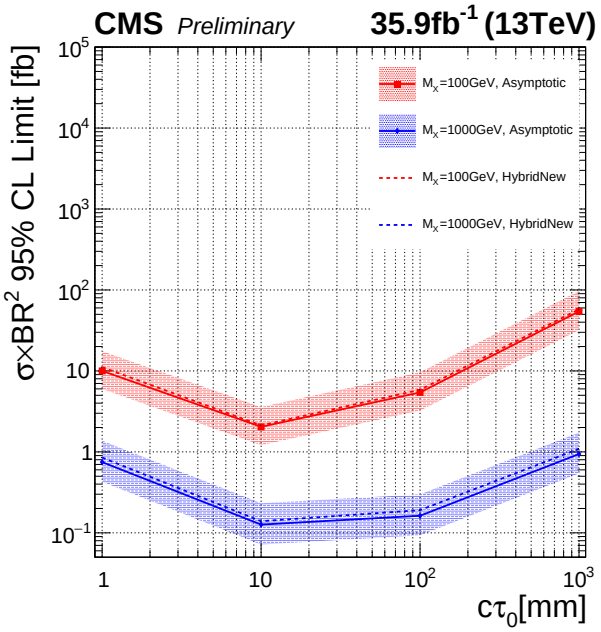

Figure 8.4: The comparison between asymptotic approximation and HybridNew method for expected limits on the Jet-Jet model.

cross section for GMSB long-lived gluino model is shown in Figure 8.5, with different gluino mass $m_{\tilde{g}}$ and proper decay length $c\tau_0$. When $m_{\tilde{g}} = 2400\,\text{GeV}$, the excluded gluino pair production cross section can be as low as ~ 0.25 fb for proper decay length between 10 mm and 210 mm. In general, for larger gluino mass the sensitivity is better. However, when proper decay length $c\tau_0 = 1\,\text{mm}$, the sensitivity of the analysis is independent of the gluino mass since the signal acceptance is mainly constrained by the online prompt track requirement in the displaced jet trigger.

The expected and observed exclusion region for a GMSB long-lived gluino in the lifetime-mass plane is shown in the right plot of Figure 8.5, based on a calculation at the next-to-leading logarithmic accuracy matched to next-to-leading order predictions (NLO+NLL) of the gluino pair production cross section at $\sqrt{s} = 13\,\text{TeV}$ [128, 129, 130, 131, 132]. For mean proper decay lengths between 20 mm and 110 mm, gluino

mass smaller than $\sim 2300\,\mathrm{GeV}$ can be excluded assuming 100% branch fraction for the $\widetilde{\mathrm{g}} \to \mathrm{g}\widetilde{\mathrm{G}}$ decay.

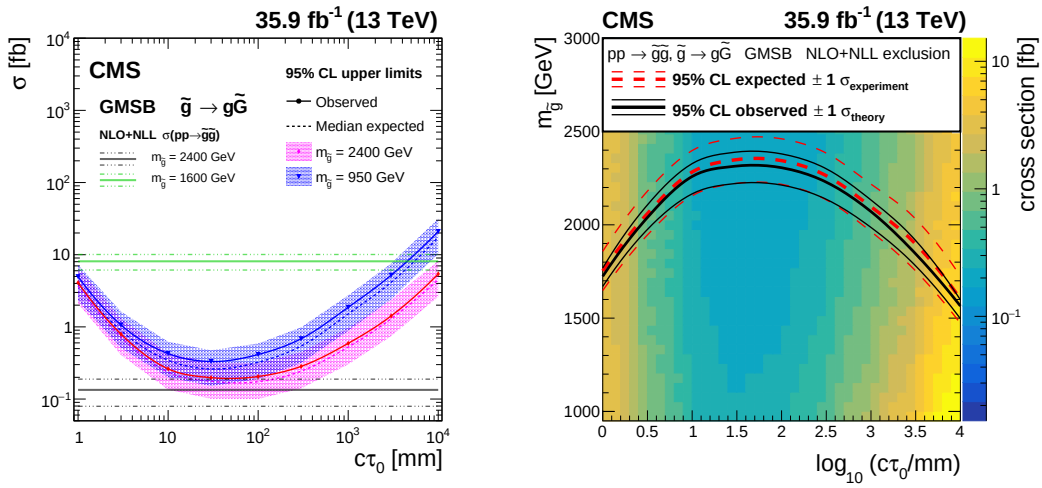

Figure 8.5: Left: the expected and observed 95% C.L. upper limits on the pair production cross section of the long-lived gluino, assuming a 100% branching fraction for $\widetilde{\mathrm{g}} \to \mathrm{g}\widetilde{\mathrm{G}}$ decays. The horizontal lines indicate the NLO+NLL gluino pair production cross sections for $m_{\widetilde{\mathrm{g}}} = 2400\,\mathrm{GeV}$ and $m_{\widetilde{\mathrm{g}}} = 1600\,\mathrm{GeV}$, as well as their variations due to the uncertainties in the choices of renormalization scales, factorization scales, and PDF sets. The solid (dashed) lines represent the observed (median expected) limits, the bands show the regions containing 68% of the distributions of the expected limits under the background-only hypothesis. Right: the expected and observed 95% C.L. limits for the long-lived gluino model in the mass-lifetime plane, assuming a 100% branching fraction for $\widetilde{\mathrm{g}} \to \mathrm{g}\widetilde{\mathrm{G}}$ decays, based on the NLO+NLL calculation of the gluino pair production cross section at $\sqrt{s} = 13\,\mathrm{TeV}$. The thick solid black (dashed red) line represents the observed (median expected) limits at 95% C.L.. The thin black lines represent the change in the observed limit due to the variation of the signal cross sections within their theoretical uncertainties. The thin red lines indicate the region containing 68% of the distribution of the expected limits under the background-only hypothesis.

8.6 RPV $\widetilde{\mathrm{g}} \to$ tbs interpretation

Figure 8.6 presents the expected and observed upper limits on the pair production cross section of the long-lived gluino in the RPV $\widetilde{\mathrm{g}} \to$ tbs model, assuming a 100%

branching fraction for the gluino to decay to top, bottom, and strange antiquarks. The upper limits on the pair production cross section are translated into upper limits on the gluino mass for different proper decay lengths, based on the NLO+NLL calculation of the gluino pair production cross section at $\sqrt{s} = 13\,\text{TeV}$ in the limit where all the other SUSY particles are much heavier and decoupled. Gluino masses up to 2400 GeV are excluded for proper decay lengths between 10 and 250 mm. The bounds are currently the most stringent on this model for proper decay lengths between 10 mm and 10 m.

8.7 RPV $\widetilde{\mathrm{t}} \to \mathrm{b}\ell$ interpretation

Figure 8.7 presents the expected and observed upper limits on the pair production cross section of the long-lived top squark in the RPV $\widetilde{\mathrm{t}} \to \mathrm{b}\ell$ model, assuming a 100% branching fraction for the top squark to decay to a bottom quark and a charged lepton. The upper limits on the pair production cross section are then translated into upper limits on the top squark mass for different proper decay lengths, based on an NLO+NLL calculation of the top squark pair production cross section at $\sqrt{s} = 13\,\text{TeV}$ in the limit where all the other SUSY particles are much heavier and decoupled. Top squark masses up to 1350 GeV are excluded for proper decay lengths between 7 and 110 mm. The bounds are currently the most stringent on this model for proper decay lengths between 3 mm and 1 m.

8.8 dRPV $\widetilde{\mathrm{t}} \to \overline{\mathrm{dd}}$ interpretation

Figure 8.8 presents the expected and observed upper limits on the pair production cross section of the long-lived top squark in the dRPV $\widetilde{\mathrm{t}} \to \overline{\mathrm{dd}}$ model, assuming a

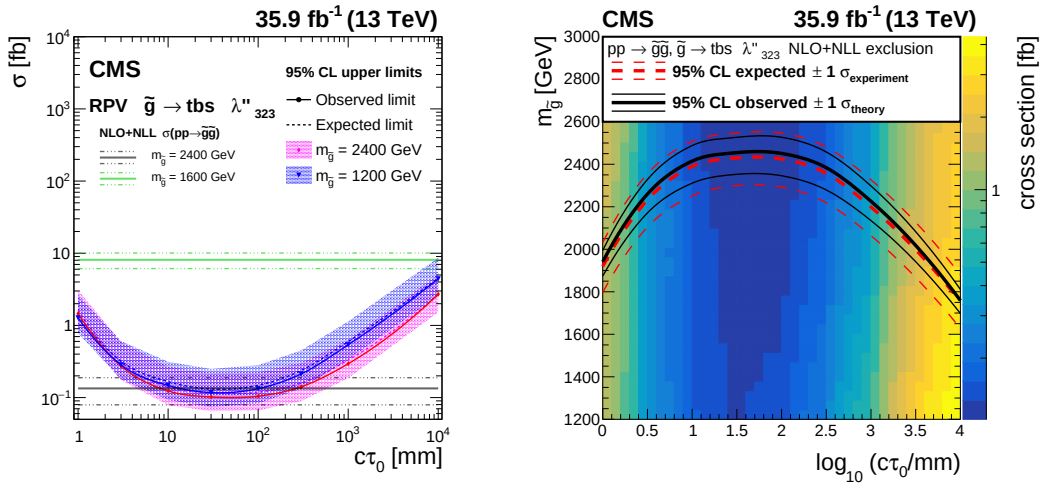

Figure 8.6: Left: the expected and observed 95% C.L. upper limits on the pair production cross section of the long-lived gluino, assuming a 100% branching fraction for $\widetilde{g} \to$ tbs decays. The horizontal lines indicate the NLO+NLL gluino pair production cross sections for $m_{\widetilde{g}} = 2400\,\text{GeV}$ and $m_{\widetilde{g}} = 1600\,\text{GeV}$, as well as their variations due to the uncertainties in the choices of renormalization scales, factorization scales, and PDF sets. The solid (dashed) lines represent the observed (median expected) limits, the bands show the regions containing 68% of the distributions of the expected limits under the background-only hypothesis. Right: the expected and observed 95% C.L. limits for the long-lived gluino model in the mass-lifetime plane, assuming a 100% branching fraction for $\widetilde{g} \to$ tbs decays, based on the NLO+NLL calculation of the gluino pair production cross section at $\sqrt{s} = 13\,\text{TeV}$. The thick solid black (dashed red) line represents the observed (median expected) limits at 95% C.L.. The thin black lines represent the change in the observed limit due to the variation of the signal cross sections within their theoretical uncertainties. The thin red lines indicate the region containing 68% of the distributions of the expected limits under the background-only hypothesis.

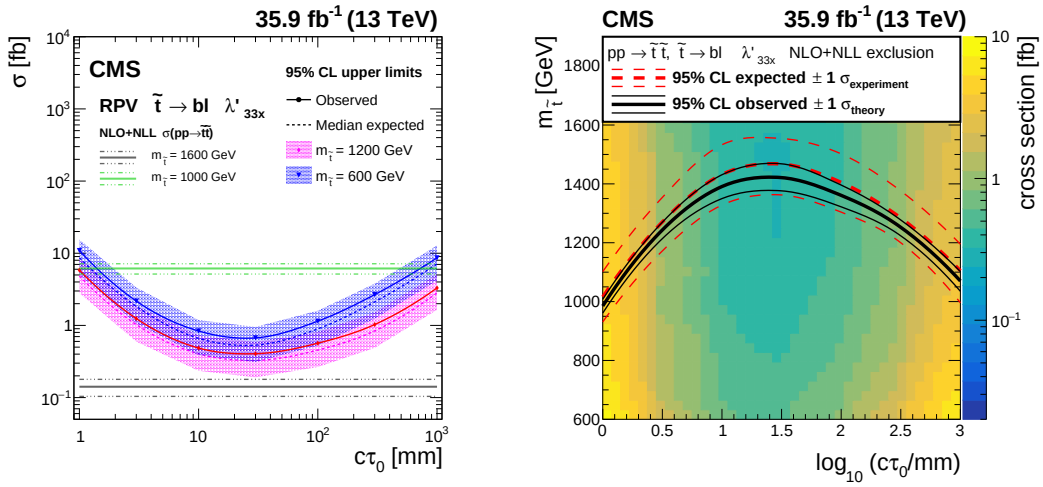

Figure 8.7: Left: the expected and observed 95% C.L. upper limits on the pair production cross section of the long-lived top squark, assuming a 100% branching fraction for $\widetilde{\mathrm{t}} \to \mathrm{b}\ell$ decays. The horizontal lines indicate the NLO+NLL top squark pair production cross sections for $m_{\widetilde{\mathrm{t}}} = 1600\,\mathrm{GeV}$ and $m_{\widetilde{\mathrm{t}}} = 1000\,\mathrm{GeV}$, as well as their variations due to the uncertainties in the choices of renormalization scales, factorization scales, and PDF sets. The solid (dashed) lines represent the observed (median expected) limits, the bands show the regions containing 68% of the distributions of the expected limits under the background-only hypothesis. Right: the expected and observed 95% C.L. limits for the long-lived top squark model in the mass-lifetime plane, assuming a 100% branching fraction for $\widetilde{\mathrm{t}} \to \mathrm{b}\ell$ decays, based on the NLO+NLL calculation of the top squark pair production cross section at $\sqrt{s} = 13\,\mathrm{TeV}$. The thick solid black (dashed red) line represents the observed (median expected) limits at 95% C.L.. The thin black lines represent the change in the observed limit due to the variation of the signal cross sections within their theoretical uncertainties. The thin red lines indicate the region containing 68% of the distributions of the expected limits under the background-only hypothesis.

100% branching fraction for the top squark to decay to two down antiquarks. The upper limits on the pair production cross section are translated into upper limits on the top squark mass for different proper decay lengths assuming a 100% branching fraction, based on the NLO+NLL calculation of the top squark pair production cross section at $\sqrt{s} = 13\,\text{TeV}$ in the limit where all the other SUSY particles are much heavier and decoupled. Top squark masses up to 1600 GeV are excluded for proper decay lengths between 10 and 100 mm. The bounds are currently the most stringent on this model for proper decay lengths between 10 mm and 10 m.

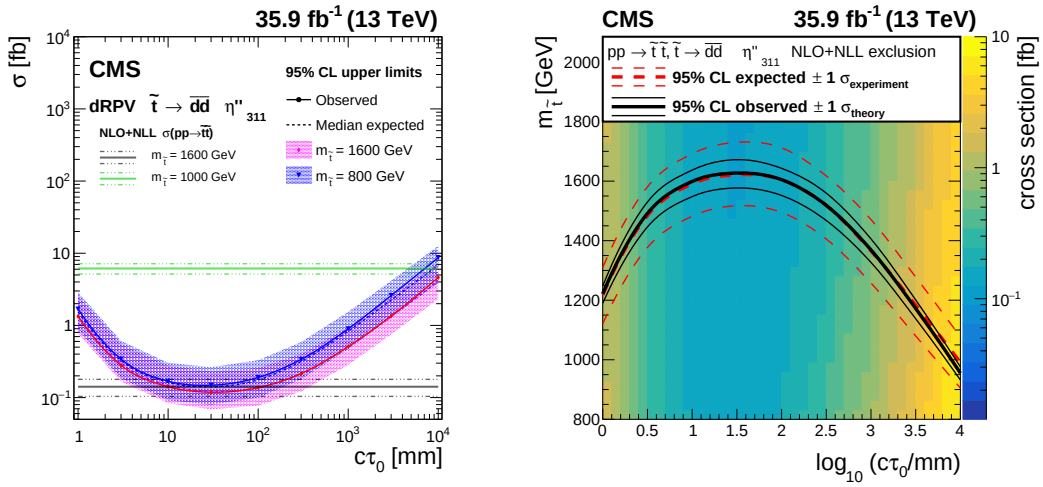

Figure 8.8: Left: the expected and observed 95% C.L. upper limits on the the pair production cross section of the long-lived top squark, assuming a 100% branching fraction for $\widetilde{\mathrm{t}} \to \overline{\mathrm{d}}\overline{\mathrm{d}}$ decays. The horizontal lines indicate the NLO+NLL top squark pair production cross sections for $m_{\widetilde{\mathrm{t}}} = 1600\,\mathrm{GeV}$ and $m_{\widetilde{\mathrm{t}}} = 1000\,\mathrm{GeV}$, as well as their variations due to the uncertainties in the choices of renormalization scales, factorization scales, and PDF sets. The solid (dashed) lines represent the observed (median expected) limits, the bands show the regions containing 68% of the distributions of the expected limits under the background-only hypothesis. Right: the expected and observed 95% C.L. limits for the long-lived top squark model in the mass-lifetime plane, assuming a 100% branching fraction for $\widetilde{\mathrm{t}} \to \overline{\mathrm{d}}\overline{\mathrm{d}}$ decays, based on an NLO+NLL calculation of the top squark pair production cross section at $\sqrt{s} = 13\,\mathrm{TeV}$. The thick solid black (dashed red) line represents the observed (median expected) limits at 95% C.L. The thin black lines represent the change in the observed limit due to the variation of the signal cross sections within their theoretical uncertainties. The thin red lines indicate the region containing 68% of the distribution of the expected limits under the background-only hypothesis.

Chapter 9

Conclusions

A search for long-lived particles decaying to jets is presented. The search is based on proton-proton collision data collected with the CMS experiment at a center-of-mass energy of 13 TeV in 2016, corresponding to an integrated luminosity of 35.9 fb^{-1}. The analysis utilizes a dedicated trigger to capture events with displaced-jet signatures, and exploits jet, track, and secondary vertex information to discriminate displaced-jet candidate events from those produced by the standard model and instrumental backgrounds. The observed yields in data are in agreement with the background predictions. For a variety of models, we set the best limits to date for long-lived particles with proper decay lengths approximately between 5 mm and 10 m. Upper limits are set at 95% confidence level on the pair production cross section of long-lived neutral particles decaying to two jets, for different masses and proper lifetimes, and are as low as 0.2 fb at high mass ($m_{\mathrm{X}} > 1000$ GeV) for proper decay lengths between 3 and 130 mm. A supersymmetric (SUSY) model with gauge-mediated supersymmetry breaking (GMSB) in which the long-lived gluino can decay to one jet and a lightest SUSY particle, is also tested. Upper limits are set on the pair production cross section of the gluino with different masses and proper decay lengths $c\tau_0$. Pair-produced long-

lived gluinos lighter than 2300 GeV are excluded for proper decay lengths between 20 and 110 mm. For an R-parity violating (RPV) SUSY model, where the long-lived gluino can decay to top, bottom, and strange antiquarks, pair-produced gluinos lighter than 2400 GeV are excluded for decay lengths between 10 and 250 mm. For a second RPV SUSY model, in which the long-lived top squark can decay to one bottom quark and a charged lepton, pair-produced long-lived top squarks lighter than 1350 GeV are excluded for decay lengths between 7 and 110 mm. For another RPV SUSY model where the long-lived top squark decays to two down antiquarks, pair-produced long-lived top squarks lighter than 1600 GeV are excluded for decay lengths between 10 and 110 mm. These are the most stringent limits to date on these models.

References

[1] C. N. Yang, *Selected Papers (1945–1980) of Chen Ning Yang*, vol. 36 of *World Scientific Series in 20th Century Physics*. Singapore, Singapore: World Scientific, 2005.

[2] C.-N. Yang and R. L. Mills, "Conservation of Isotopic Spin and Isotopic Gauge Invariance," *Phys. Rev.*, vol. 96, p. 191, 1954.

[3] G. 't Hooft and M. J. G. Veltman, "Regularization and Renormalization of Gauge Fields," *Nucl. Phys. B*, vol. 44, p. 189, 1972.

[4] J. Goldstone, A. Salam, and S. Weinberg, "Broken Symmetries," *Phys. Rev.*, vol. 127, p. 965, 1962.

[5] Y. Nambu and G. Jona-Lasinio, "Dynamical Model of Elementary Particles Based on an Analogy with Superconductivity. I," *Phys. Rev.*, vol. 122, p. 345, 1961.

[6] Y. Nambu and G. Jona-Lasinio, "Dynamical Model of Elementary Particles Based on an Analogy with Superconductivity. II," *Phys. Rev.*, vol. 124, p. 246, 1961.

[7] S. R. Coleman, J. Wess, and B. Zumino, "Structure of phenomenological Lagrangians. I," *Phys. Rev.*, vol. 177, p. 2239, 1969.

[8] R. F. Dashen, "Some features of chiral symmetry breaking," *Phys. Rev. D*, vol. 3, p. 1879, 1971.

[9] F. Englert and R. Brout, "Broken Symmetry and the Mass of Gauge Vector Mesons," *Phys. Rev. Lett.*, vol. 13, p. 321, 1964.

[10] P. W. Higgs, "Broken symmetries, massless particles and gauge fields," *Phys. Lett.*, vol. 12, p. 132, 1964.

[11] G. S. Guralnik, C. R. Hagen, and T. W. B. Kibble, "Global Conservation Laws and Massless Particles," *Phys. Rev. Lett.*, vol. 13, p. 585, 1964.

[12] S. Weinberg, "General Theory of Broken Local Symmetries," *Phys. Rev. D*, vol. 7, p. 1068, 1973.

[13] S. Weinberg, "A Model of Leptons," *Phys. Rev. Lett.*, vol. 19, p. 1264, 1967.

[14] F. J. Hasert *et al.*, "Observation of Neutrino Like Interactions Without Muon Or Electron in the Gargamelle Neutrino Experiment," *Phys. Lett. B*, vol. 46, p. 138, 1973.

[15] G. Arnison *et al.*, "Experimental Observation of Events with Large Missing Transverse Energy Accompanied by a Jet Or a Photon(s) in $\mathrm{p\overline{p}}$ Collisions at $\sqrt{s} = 540\,\mathrm{GeV}$," *Phys. Lett. B*, vol. 139, p. 115, 1984.

[16] G. Arnison *et al.*, "Experimental Observation of Lepton Pairs of Invariant Mass Around $95\,\mathrm{GeV}/c^2$ at the CERN SPS Collider," *Phys. Lett. B*, vol. 126, p. 398, 1983.

[17] G. Arnison *et al.*, "Further Evidence for Charged Intermediate Vector Bosons at the SPS Collider," *Phys. Lett. B*, vol. 129, p. 273, 1983.

[18] G. Arnison *et al.*, "Observation of Muonic Z^0 Decay at the $\overline{p}p$ Collider," *Phys. Lett. B*, vol. 147, p. 241, 1984.

[19] G. Aad *et al.*, "Observation of a new particle in the search for the Standard Model Higgs boson with the ATLAS detector at the LHC," *Phys. Lett. B*, vol. 716, p. 1, 2012.

[20] S. Chatrchyan *et al.*, "Observation of a new boson at a mass of 125 GeV with the CMS experiment at the LHC," *Phys. Lett. B*, vol. 716, p. 30, 2012.

[21] S. L. Glashow, "Partial Symmetries of Weak Interactions," *Nucl. Phys.*, vol. 22, p. 579, 1961.

[22] A. Salam, "Weak and Electromagnetic Interactions," *Conf. Proc.*, vol. C680519, p. 367, 1968.

[23] S. L. Glashow, J. Iliopoulos, and L. Maiani, "Weak Interactions with Lepton-Hadron Symmetry," *Phys. Rev. D*, vol. 2, p. 1285, 1970.

[24] J. J. Aubert *et al.*, "Experimental Observation of a Heavy Particle J," *Phys. Rev. Lett.*, vol. 33, p. 1404, 1974.

[25] J. E. Augustin *et al.*, "Discovery of a Narrow Resonance in e^+e^- Annihilation," *Phys. Rev. Lett.*, vol. 33, p. 1406, 1974.

[26] J. H. Christenson, J. W. Cronin, V. L. Fitch, and R. Turlay, "Evidence for the 2π Decay of the K_2^0 Meson," *Phys. Rev. Lett.*, vol. 13, p. 138, 1964.

[27] M. Kobayashi and T. Maskawa, "CP Violation in the Renormalizable Theory of Weak Interaction," *Prog. Theor. Phys.*, vol. 49, p. 652, 1973.

[28] S. W. Herb *et al.*, "Observation of a Dimuon Resonance at 9.5 GeV in 400-GeV Proton-Nucleus Collisions," *Phys. Rev. Lett.*, vol. 39, p. 252, 1977.

[29] F. Abe *et al.*, "Observation of top quark production in $\bar{p}p$ collisions," *Phys. Rev. Lett.*, vol. 74, p. 2626, 1995.

[30] S. Abachi *et al.*, "Observation of the top quark," *Phys. Rev. Lett.*, vol. 74, p. 2632, 1995.

[31] J. S. Bell and R. Jackiw, "A PCAC puzzle: $\pi^0 \to \gamma\gamma$ in the σ model," *Nuovo Cim. A*, vol. 60, p. 47, 1969.

[32] S. L. Adler, "Axial vector vertex in spinor electrodynamics," *Phys. Rev.*, vol. 177, p. 2426, 1969.

[33] K. Fujikawa, "Path Integral Measure for Gauge Invariant Fermion Theories," *Phys. Rev. Lett.*, vol. 42, p. 1195, 1979.

[34] D. J. Gross and F. Wilczek, "Ultraviolet Behavior of Nonabelian Gauge Theories," *Phys. Rev. Lett.*, vol. 30, p. 1343, 1973.

[35] H. Fritzsch, M. Gell-Mann, and H. Leutwyler, "Advantages of the Color Octet Gluon Picture," *Phys. Lett. B*, vol. 47, p. 365, 1973.

[36] M. Gell-Mann and F. E. Low, "Quantum electrodynamics at small distances," *Phys. Rev.*, vol. 95, p. 1300, 1954.

[37] C. G. Callan, Jr., "Broken scale invariance in scalar field theory," *Phys. Rev. D*, vol. 2, p. 1541, 1970.

[38] K. Symanzik, "Small distance behavior in field theory and power counting," *Commun. Math. Phys.*, vol. 18, p. 227, 1970.

[39] K. G. Wilson, "Renormalization group and critical phenomena. 1. Renormalization group and the Kadanoff scaling picture," *Phys. Rev. B*, vol. 4, p. 3174, 1971.

[40] K. G. Wilson, "Renormalization group and critical phenomena. 2. Phase space cell analysis of critical behavior," *Phys. Rev. B*, vol. 4, p. 3184, 1971.

[41] J. Polchinski, "Renormalization and Effective Lagrangians," *Nucl. Phys. B*, vol. 231, p. 269, 1984.

[42] G. 't Hooft, "Dimensional regularization and the renormalization group," *Nucl. Phys. B*, vol. 61, p. 455, 1973.

[43] D. J. Gross and F. Wilczek, "Asymptotically Free Gauge Theories - I," *Phys. Rev. D*, vol. 8, p. 3633, 1973.

[44] H. D. Politzer, "Reliable Perturbative Results for Strong Interactions?," *Phys. Rev. Lett.*, vol. 30, p. 1346, 1973.

[45] E. D. Bloom *et al.*, "High-Energy Inelastic *e-p* Scattering at 6-Degrees and 10-Degrees," *Phys. Rev. Lett.*, vol. 23, p. 930, 1969.

[46] M. Breidenbach, J. I. Friedman, H. W. Kendall, E. D. Bloom, D. H. Coward, H. C. DeStaebler, J. Drees, L. W. Mo, and R. E. Taylor, "Observed Behavior of Highly Inelastic Electron-Proton Scattering," *Phys. Rev. Lett.*, vol. 23, p. 935, 1969.

[47] S. Coleman and D. J. Gross, "Price of asymptotic freedom," *Phys. Rev. Lett.*, vol. 31, p. 851, 1973.

[48] A. A. Belavin, A. M. Polyakov, A. S. Schwartz, and Yu. S. Tyupkin, "Pseudoparticle Solutions of the Yang-Mills Equations," *Phys. Lett. B*, vol. 59, p. 85, 1975.

[49] S. Weinberg, "The U(1) Problem," *Phys. Rev. D*, vol. 11, p. 3583, 1975.

[50] G. 't Hooft, "Symmetry Breaking Through Bell-Jackiw Anomalies," *Phys. Rev. Lett.*, vol. 37, p. 8, 1976.

[51] G. 't Hooft, "Computation of the Quantum Effects Due to a Four-Dimensional Pseudoparticle," *Phys. Rev. D*, vol. 14, p. 3432, 1976.

[52] V. Baluni, "CP Violating Effects in QCD," *Phys. Rev. D*, vol. 19, p. 2227, 1979.

[53] R. J. Crewther, P. Di Vecchia, G. Veneziano, and E. Witten, "Chiral Estimate of the Electric Dipole Moment of the Neutron in Quantum Chromodynamics," *Phys. Lett. B*, vol. 88, p. 123, 1979. [Erratum: Phys. Lett. B 91, 487(1980)].

[54] J. M. Pendlebury *et al.*, "Revised experimental upper limit on the electric dipole moment of the neutron," *Phys. Rev. D*, vol. 92, no. 9, p. 092003, 2015.

[55] R. D. Peccei and H. R. Quinn, "CP Conservation in the Presence of Instantons," *Phys. Rev. Lett.*, vol. 38, p. 1440, 1977.

[56] R. D. Peccei and H. R. Quinn, "Constraints Imposed by CP Conservation in the Presence of Instantons," *Phys. Rev. D*, vol. 16, p. 1791, 1977.

[57] S. Weinberg, "A New Light Boson?," *Phys. Rev. Lett.*, vol. 40, p. 223, 1978.

[58] F. Wilczek, "Problem of Strong P and T Invariance in the Presence of Instantons," *Phys. Rev. Lett.*, vol. 40, p. 279, 1978.

[59] D. E. Kaplan, M. A. Luty, and K. M. Zurek, "Asymmetric Dark Matter," *Phys. Rev. D*, vol. 79, p. 115016, 2009.

[60] L. J. Hall, K. Jedamzik, J. March-Russell, and S. M. West, "Freeze-In Production of FIMP Dark Matter," *JHEP*, vol. 03, p. 080, 2010.

[61] I.-W. Kim and K. M. Zurek, "Flavor and Collider Signatures of Asymmetric Dark Matter," *Phys. Rev. D*, vol. 89, no. 3, p. 035008, 2014.

[62] Y. Cui and B. Shuve, "Probing Baryogenesis with Displaced Vertices at the LHC," *JHEP*, vol. 02, p. 049, 2015.

[63] R. T. Co, F. D'Eramo, L. J. Hall, and D. Pappadopulo, "Freeze-In Dark Matter with Displaced Signatures at Colliders," *JCAP*, vol. 1512, p. 024, 2015.

[64] L. Calibbi, L. Lopez-Honorez, S. Lowette, and A. Mariotti, "Singlet-Doublet Dark Matter Freeze-in: LHC displaced signatures versus cosmology," *JHEP*, vol. 09, p. 037, 2018.

[65] Z. Chacko, H.-S. Goh, and R. Harnik, "The Twin Higgs: Natural electroweak breaking from mirror symmetry," *Phys. Rev. Lett.*, vol. 96, p. 231802, 2006.

[66] H. Cai, H.-C. Cheng, and J. Terning, "A Quirky Little Higgs Model," *JHEP*, vol. 05, p. 045, 2009.

[67] N. Craig, S. Knapen, and P. Longhi, "Neutral Naturalness from Orbifold Higgs Models," *Phys. Rev. Lett.*, vol. 114, p. 061803, 2015.

[68] N. Craig, A. Katz, M. Strassler, and R. Sundrum, "Naturalness in the Dark at the LHC," *JHEP*, vol. 07, p. 105, 2015.

[69] D. Curtin and C. B. Verhaaren, "Discovering Uncolored Naturalness in Exotic Higgs Decays," *JHEP*, vol. 12, p. 072, 2015.

[70] A. Atre, T. Han, S. Pascoli, and B. Zhang, "The Search for Heavy Majorana Neutrinos," *JHEP*, vol. 05, p. 030, 2009.

[71] M. Drewes, "The Phenomenology of Right Handed Neutrinos," *Int. J. Mod. Phys. E*, vol. 22, p. 1330019, 2013.

[72] F. F. Deppisch, P. S. Bhupal Dev, and A. Pilaftsis, "Neutrinos and Collider Physics," *New J. Phys.*, vol. 17, p. 075019, 2015.

[73] Y. Cai, T. Han, T. Li, and R. Ruiz, "Lepton Number Violation: Seesaw Models and Their Collider Tests," *Front.in Phys.*, vol. 6, p. 40, 2018.

[74] R. Haag, J. T. Lopuszanski, and M. Sohnius, "All Possible Generators of Supersymmetries of the S-Matrix," *Nucl. Phys. B*, vol. 88, p. 257, 1975.

[75] A. Salam and J. A. Strathdee, "Supergauge Transformations," *Nucl. Phys. B*, vol. 76, p. 477, 1974.

[76] S. Ferrara, J. Wess, and B. Zumino, "Supergauge Multiplets and Superfields," *Phys. Lett. B*, vol. 51, p. 239, 1974.

[77] S. Weinberg, "Supersymmetry at Ordinary Energies. 1. Masses and Conservation Laws," *Phys. Rev. D*, vol. 26, p. 287, 1982.

[78] P. Fayet, "Supergauge Invariant Extension of the Higgs Mechanism and a Model for the electron and Its Neutrino," *Nucl. Phys. B*, vol. 90, p. 104, 1975.

[79] G. R. Farrar and P. Fayet, "Phenomenology of the Production, Decay, and Detection of New Hadronic States Associated with Supersymmetry," *Phys. Lett. B*, vol. 76, p. 575, 1978.

[80] C. Csaki, E. Kuflik, and T. Volansky, "Dynamical R-Parity Violation," *Phys. Rev. Lett.*, vol. 112, p. 131801, 2014.

[81] C. Csaki, E. Kuflik, S. Lombardo, O. Slone, and T. Volansky, "Phenomenology of a Long-Lived LSP with R-Parity Violation," *JHEP*, vol. 08, p. 016, 2015.

[82] L. O'Raifeartaigh, "Spontaneous Symmetry Breaking for Chiral Scalar Superfields," *Nucl. Phys. B*, vol. 96, p. 331, 1975.

[83] P. Fayet and J. Iliopoulos, "Spontaneously Broken Supergauge Symmetries and Goldstone Spinors," *Phys. Lett. B*, vol. 51, p. 461, 1974.

[84] S. Deser and B. Zumino, "Broken Supersymmetry and Supergravity," *Phys. Rev. Lett.*, vol. 38, p. 1433, 1977.

[85] P. Fayet, "Mixing Between Gravitational and Weak Interactions Through the Massive Gravitino," *Phys. Lett. B*, vol. 70, p. 461, 1977.

[86] G. F. Giudice and R. Rattazzi, "Theories with gauge mediated supersymmetry breaking," *Phys. Rept.*, vol. 322, p. 419, 1999.

[87] P. Meade, N. Seiberg, and D. Shih, "General Gauge Mediation," *Prog. Theor. Phys. Suppl.*, vol. 177, p. 143, 2009.

[88] K. G. Wilson, "The Renormalization Group and Strong Interactions," *Phys. Rev. D*, vol. 3, p. 1818, 1971.

[89] K. G. Wilson and M. E. Fisher, "Critical exponents in 3.99 dimensions," *Phys. Rev. Lett.*, vol. 28, p. 240, 1972.

[90] K. G. Wilson, "The Origins of lattice gauge theory," *Nucl. Phys. Proc. Suppl.*, vol. 140, p. 3, 2005.

[91] N. Arkani-Hamed and S. Dimopoulos, "Supersymmetric unification without low energy supersymmetry and signatures for fine-tuning at the LHC," *JHEP*, vol. 06, p. 073, 2005.

[92] G. F. Giudice and A. Romanino, "Split supersymmetry," *Nucl. Phys. B*, vol. 699, p. 65, 2004. [Erratum: Nucl. Phys. B 706, 487(2005)].

[93] N. Arkani-Hamed, S. Dimopoulos, G. F. Giudice, and A. Romanino, "Aspects of split supersymmetry," *Nucl. Phys. B*, vol. 709, p. 3, 2005.

[94] J. L. Hewett, B. Lillie, M. Masip, and T. G. Rizzo, "Signatures of long-lived gluinos in split supersymmetry," *JHEP*, vol. 09, p. 070, 2004.

[95] P. Gambino, G. F. Giudice, and P. Slavich, "Gluino decays in split supersymmetry," *Nucl. Phys. B*, vol. 726, p. 35, 2005.

[96] N. Arkani-Hamed, A. Gupta, D. E. Kaplan, N. Weiner, and T. Zorawski, "Simply Unnatural Supersymmetry," 2012.

[97] L. Evans and P. Bryant, "LHC Machine," *JINST*, vol. 3, p. S08001, 2008.

[98] S. Chatrchyan *et al.*, "The CMS Experiment at the CERN LHC," *JINST*, vol. 3, p. S08004, 2008.

[99] S. Abdullin *et al.*, "Design, performance, and calibration of CMS hadron-barrel calorimeter wedges," *Eur. Phys. J. C*, vol. 55, no. 1, p. 159, 2008.

[100] G. Baiatian *et al.*, "Design, performance, and calibration of CMS hadron endcap calorimeters," Tech. Rep. CMS-NOTE-2008-010, 2008.

[101] R. Fruhwirth, "Application of Kalman filtering to track and vertex fitting," *Nucl. Instrum. Meth.*, vol. A262, p. 444, 1987.

[102] M. Cacciari, G. P. Salam, and G. Soyez, "The anti-k_{T} jet clustering algorithm," *JHEP*, vol. 04, p. 063, 2008.

[103] M. Cacciari, G. P. Salam, and G. Soyez, "FastJet user manual," *Eur. Phys. J. C*, vol. 72, p. 1896, 2012.

[104] V. Khachatryan *et al.*, "Jet energy scale and resolution in the CMS experiment in pp collisions at 8 TeV," *JINST*, vol. 12, p. P02014, 2017.

[105] J. Alwall, R. Frederix, S. Frixione, V. Hirschi, F. Maltoni, O. Mattelaer, H. S. Shao, T. Stelzer, P. Torrielli, and M. Zaro, "The automated computation of tree-level and next-to-leading order differential cross sections, and their matching to parton shower simulations," *JHEP*, vol. 07, p. 079, 2014.

[106] T. Sjöstrand, S. Ask, J. R. Christiansen, R. Corke, N. Desai, P. Ilten, S. Mrenna, S. Prestel, C. O. Rasmussen, and P. Z. Skands, "An introduction to PYTHIA 8.2," *Comput. Phys. Commun.*, vol. 191, p. 159, 2015.

[107] J. Alwall *et al.*, "Comparative study of various algorithms for the merging of parton showers and matrix elements in hadronic collisions," *Eur. Phys. J. C*, vol. 53, p. 473, 2008.

[108] V. Khachatryan *et al.*, "Event generator tunes obtained from underlying event and multiparton scattering measurements," *Eur. Phys. J. C*, vol. 76, p. 155, 2016.

[109] R. D. Ball *et al.*, "Parton distributions for the LHC Run II," *JHEP*, vol. 04, p. 040, 2015.

[110] R. D. Ball, V. Bertone, S. Carrazza, L. Del Debbio, S. Forte, A. Guffanti, N. P. Hartland, and J. Rojo, "Parton distributions with QED corrections," *Nucl. Phys. B*, vol. 877, p. 290, 2013.

[111] G. R. Farrar and P. Fayet, "Bounds on R-hadron production from calorimetry experiments," *Phys. Lett. B*, vol. 79, p. 442, 1978.

[112] M. Fairbairn, A. C. Kraan, D. A. Milstead, T. Sjostrand, P. Z. Skands, and T. Sloan, "Stable massive particles at colliders," *Phys. Rept.*, vol. 438, p. 1, 2007.

[113] C. Csaki, Y. Grossman, and B. Heidenreich, "Minimal flavor violation supersymmetry: a natural theory for R-parity violation," *Phys. Rev. D*, vol. 85, p. 095009, 2012.

[114] R. Barbier, C. Bérat, M. Besançon, M. Chemtob, A. Deandrea, E. Dudas, P. Fayet, S. Lavignac, G. Moreau, E. Perez, and Y. Sirois, "R-parity violating supersymmetry," *Phys. Rept.*, vol. 420, p. 1, 2005.

[115] P. W. Graham, D. E. Kaplan, S. Rajendran, and P. Saraswat, "Displaced supersymmetry," *JHEP*, vol. 07, p. 149, 2012.

[116] C. Csaki, E. Kuflik, O. Slone, and T. Volansky, "Models of dynamical R-parity violation," *JHEP*, vol. 06, p. 045, 2015.

[117] R. Frühwirth, W. Waltenberger, and P. Vanlaer, "Adaptive vertex fitting," *J. Phys. G*, vol. 34, p. N343, 2007.

[118] "Search for long-lived neutral particles decaying to dijets," Tech. Rep. CMS-PAS-EXO-12-038, CERN, Geneva, 2013.

[119] S. C. Johnson, "Hierarchical clustering schemes," *Psychometrika*, vol. 32, p. 241, 1967.

[120] G. Punzi, "Sensitivity of searches for new signals and its optimization," *eConf*, vol. C030908, p. MODT002, 2003. [,79(2003)].

[121] J. Butterworth *et al.*, "PDF4LHC recommendations for LHC Run II," *J. Phys. G*, vol. 43, p. 023001, 2016.

[122] A. Buckley, J. Ferrando, S. Lloyd, K. Nordström, B. Page, M. Rüfenacht, M. Schönherr, and G. Watt, "LHAPDF6: parton density access in the LHC precision era," *Eur. Phys. J. C*, vol. 75, p. 132, 2015.

[123] T. Junk, "Confidence level computation for combining searches with small statistics," *Nucl. Instrum. Meth. A*, vol. 434, p. 435, 1999.

[124] A. L. Read, "Presentation of search results: The CL_s technique," *J. Phys. G*, vol. 28, p. 2693, 2002.

[125] G. Cowan, K. Cranmer, E. Gross, and O. Vitells, "Asymptotic formulae for likelihood-based tests of new physics," *Eur. Phys. J. C*, vol. 71, p. 1554, 2011. [Erratum: Eur. Phys. J. C, 73, 2501(2013)].

[126] The ATLAS Collaboration, The CMS Collaboration, The LHC Higgs Combination Group, "Procedure for the LHC Higgs boson search combination in Summer 2011," Tech. Rep. CMS-NOTE-2011-005, ATL-PHYS-PUB-2011-11, 2011.

[127] J. Neyman, E. S. Pearson, and K. Pearson, "Ix. on the problem of the most efficient tests of statistical hypotheses," *Philosophical Transactions of the Royal Society of London. Series A, Containing Papers of a Mathematical or Physical Character*, vol. 231, no. 694, p. 289, 1933.

[128] W. Beenakker, R. Hopker, M. Spira, and P. M. Zerwas, "Squark and gluino production at hadron colliders," *Nucl. Phys. B*, vol. 492, p. 51, 1997.

[129] A. Kulesza and L. Motyka, "Threshold resummation for squark-antisquark and gluino-pair production at the LHC," *Phys. Rev. Lett.*, vol. 102, p. 111802, 2009.

[130] A. Kulesza and L. Motyka, "Soft gluon resummation for the production of gluino-gluino and squark-antisquark pairs at the LHC," *Phys. Rev. D*, vol. 80, p. 095004, 2009.

[131] W. Beenakker, S. Brensing, M. n. Kramer, A. Kulesza, E. Laenen, L. Motyka, and I. Niessen, "Squark and gluino hadroproduction," *Int. J. Mod. Phys. A*, vol. 26, p. 2637, 2011.

[132] C. Borschensky, M. Krämer, A. Kulesza, M. Mangano, S. Padhi, T. Plehn, and X. Portell, "Squark and gluino production cross sections in pp collisions at $\sqrt{s}$ = 13, 14, 33 and 100 TeV," *Eur. Phys. J. C*, vol. 74, p. 3174, 2014.